

**DEVELOPMENT OF A DIRECT CONTACT HEAT EXCHANGER
FOR A PARTICLE HEATING CONCENTRATOR SOLAR POWER
APPLICATION**

A Dissertation
Presented to
The Academic Faculty

by

Ramy K. Imam

In Partial Fulfillment
of the Requirements for the Degree
Master of Science in the
School of Mechanical Engineering

Georgia Institute of Technology
May 2018

COPYRIGHT © 2018 BY RAMY IMAM

**DEVELOPMENT OF A DIRECT CONTACT HEAT EXCHANGER
FOR PARTICLE HEATING CONCENTRATOR SOLAR POWER
APPLICATION**

Approved by:

Dr. Sheldon M. Jeter, Advisor
School of Mechanical Engineering
Georgia Institute of Technology

Dr. Said I. Abdel-Khalik
School of Mechanical Engineering
Georgia Institute of Technology

Dr. Hany A. Al-Ansary
School of Mechanical Engineering
King Saud University

Date Approved: [April 09, 2018]

For my mother, father, and sister.

ACKNOWLEDGEMENTS

I would like to express my gratitude to my academic and research advisor, Professor Sheldon Jeter, for his continuous encouragement, support, and guidance during my master's studies. Under his instructions, I have learned not only how to conduct research but also the method for systematically solving the engineering problems and exploring new engineering solutions. I would also like to thank Professor Said Abdel-Khalik and Professor Hany Al-Ansary for taking the time to serve on my thesis defense committee. I would also like to express my appreciation to all my colleagues working in the lab, for their encouragement, care, and company, these include Mathew Golob, Clayton Naguey, and Kenzo Repole. In addition, I want to thank Qalaa Holding Scholarship Foundation for their continuous support and assistance. Finally, I especially want to thank my mother and father for their constant encouragement and affection and for supporting me and providing encouragement in this endeavor.

TABLE OF CONTENTS

ACKNOWLEDGEMENTS	iv
LIST OF TABLES	ix
LIST OF FIGURES	xii
List of Equations	xviii
LIST OF SYMBOLS AND ABBREVIATIONS	xx
SUMMARY	xxiii
CHAPTER 1. Introduction	1
1.1 Problem Statement	2
1.2 Objectives	3
CHAPTER 2. Background	4
2.1 Solar Thermal Energy	4
2.1.1 Solar Irradiance	4
2.1.2 Concentrated Solar Power Plants	5
2.1.3 Storage in Solar Power Towers	9
2.1.4 Particulates as a Heat Transfer Fluid	9
2.2 System Description	11
CHAPTER 3. Literature Review	14
3.1 Direct Contact Heat Exchangers	14
3.1.1 Fixed Bed Heat Exchangers	14
3.1.2 Moving Bed Heat Exchanger	16
3.1.3 Fluidized Bed Heat Exchangers	20
3.1.4 Baffles	24
3.2 Particulate Flow	27
3.2.1 Falling Particles	27
3.2.2 Particle Bed Fluidization	31
3.2.3 Classification of Powders	32
3.2.4 Particle Properties	36
3.3 Summary	38
CHAPTER 4. Minimal Fluidization Velocity	39
4.1 Introduction	39
4.2 Experimental Setup	40
4.2.1 Design	40
4.2.2 Measurements and Methods	40
4.3 Results and Discussion	43
CHAPTER 5. Overview of Internal Designs of Heat Exchangers	46

5.1	Introduction	46
5.2	Material Geometry	49
5.2.1	Conical Design	49
5.2.2	Disc & Donut Design	50
5.2.3	Zigzag Design	51
5.2.4	Chevrons Design	52
5.2.5	Tubular Designs	53
5.2.6	Corrugated Sheets Design	55
5.2.7	Helical Design	56
5.2.8	Cross Zig Zag Design	57
5.3	Type of Porous Structure	58
5.3.1	Perforated Plate	58
5.3.2	Wire Mesh	59
5.3.3	Foam	59
5.3.4	Directional Porous Structure	60
5.4	Heat Exchanger Material Requirements	60
5.5	Orientation of Heat Exchanger	61
5.6	Concluding Remarks	62
CHAPTER 6.	Investigation of Particle Inlet	64
6.1	Introduction	64
6.2	Design and Setup	65
6.2.1	Instrumentation	65
6.2.2	First Iteration	67
6.2.3	Second Iteration	70
6.2.4	Third Iteration	72
6.3	Methodology	84
6.4	Results	87
6.4.1	Small D - Perforated Plate with 40% Open Area	87
6.4.2	Large D - Perforated Plate with 40% Open Area	91
6.4.3	Small D - Perforated Plate with 51% Open Area	96
6.4.4	Large D - Perforated Plate with 51% Open Area	100
6.5	Uncertainty Analysis	105
6.6	Discussion	106
6.7	Conclusion	110
CHAPTER 7.	Investigation of Particle Flow	111
7.1	Introduction	112
7.2	Particle Fluidization	112
7.3	Particle Entrainment	114
7.3.1	Calculated Entrainment	114
7.3.2	Experiment Entrainment	118
7.4	Simple Particle Dynamic Simulation	136
7.4.1	Conical Design	137
7.4.2	Disc and Donut Design	138
7.4.3	Zigzag Design	140
7.4.4	Chevrons Design	141

7.4.5	Conclusions	142
7.5	Experimental Observations of Particle Distribution	143
7.6	Turbine Erosion	145
7.7	Summary	146
CHAPTER 8.	Particle Control	148
8.1	Introduction	148
8.2	Type of Valves	148
8.2.1	Rotary Paddle Wheel	148
8.2.2	Butterfly Valve	149
8.2.3	Gate Valve	150
8.2.4	T-valve	151
8.2.5	Pinch Valve	152
8.3	Modified Valves	152
8.3.1	Rotating Pocket Valve	152
8.3.2	Rotated Diaphragm Valve	153
8.3.3	Particle Bridging to Control Flow	154
8.4	Particle control in a Solar Tower System	155
8.5	T-Valve Airlock System	158
8.6	Conclusion	159
CHAPTER 9.	Conclusion	160
9.1	Conclusions	160
9.2	10 MW Solar Tower Plant	163
9.3	Summary	166
9.4	Future Work	169
References		171
Appendix A: Accucast ID50-K Foundry properties		176
Appendix B: Particle Materials		178
Appendix C: Types of Rotary Valve Air Leakage		181
Appendix D: T-Valve		182
Appendix E: T-Valve Airlock System		184
Appendix F: Airlock Cycling EES Calculations		185
Appendix G: Strainer		188
Appendix H: RTV Solar Tower System Components		190
Appendix I: Entrainment Calculations in EES		192
Appendix J: Uncertainty Analysis		194

Appendix K: Air Leakage Measurement	220
Appendix L: Entrainment Uncertainty Calculations	222
Appendix M: Uncertainty Analysis for Particle Size Measurements	229

LIST OF TABLES

TABLE 1: COMPARISON OF VARIOUS CONCENTRATING SOLAR POWER TECHNOLOGIES [5].	8
TABLE 2: BAFFLE DIAMETER AND TOLERANCES [26].	25
TABLE 3: SINGLE PARTICLE DRAG COEFFICIENT CORRELATIONS BASED ON ITS REYNOLDS NUMBER [29].	29
TABLE 4: TERMINAL VELOCITY OF A SINGLE PARTICLE BASED ON ITS REYNOLDS NUMBER [29].	31
TABLE 5: GELDART'S PARTICLE CLASSIFICATION [29].	33
TABLE 6: CARBO ACCUCAST ID50 PARTICLE PROPERTIES [32].	43
TABLE 7: RAW DATA FOR THE MINIMAL FLUIDIZATION VELOCITY EXPERIMENT.	44
TABLE 8: VOLUME FLOW RATE AND MASS FLOW RATE FOR THE SMALL HOLE DIAMETER WITH A 40% OPEN AREA AND A PRESSURE OF 0 BAR (NO SUPPLY AIR).	87
TABLE 9: VOLUME FLOW RATE AND MASS FLOW RATE FOR THE SMALL HOLE DIAMETER WITH A 40% OPEN AREA AND A SUPPLY AIR PRESSURE OF 0.5 BAR.	88
TABLE 10: VOLUME FLOW RATE AND MASS FLOW RATE FOR THE SMALL HOLE DIAMETER WITH A 40% OPEN AREA AND A SUPPLY AIR PRESSURE OF 1 BAR.	89
TABLE 11: VOLUME FLOW RATE AND MASS FLOW RATE FOR THE SMALL HOLE DIAMETER WITH A 40% OPEN AREA AND A SUPPLY AIR PRESSURE OF 1.5 BAR.	90
TABLE 12: VOLUME FLOW RATE AND MASS FLOW RATE FOR THE SMALL HOLE DIAMETER WITH A 40% OPEN AREA AND A SUPPLY AIR PRESSURE OF 2 BAR.	91
TABLE 13: VOLUME FLOW RATE AND MASS FLOW RATE FOR THE LARGE HOLE DIAMETER WITH A 40% OPEN AREA AND A SUPPLY AIR PRESSURE OF 0 BAR.	92
TABLE 14: VOLUME FLOW RATE AND MASS FLOW RATE FOR THE LARGE HOLE DIAMETER WITH A 40% OPEN AREA AND A SUPPLY AIR PRESSURE OF 0.5 BAR.	93
TABLE 15: VOLUME FLOW RATE AND MASS FLOW RATE FOR THE SMALL HOLE DIAMETER WITH A 40% OPEN AREA AND A SUPPLY AIR PRESSURE OF 1 BAR.	94
TABLE 16: VOLUME FLOW RATE AND MASS FLOW RATE FOR THE LARGE HOLE DIAMETER WITH A 40% OPEN AREA AND A SUPPLY AIR PRESSURE OF 1.5 BAR.	95

TABLE 17: VOLUME FLOW RATE AND MASS FLOW RATE FOR THE LARGE HOLE DIAMETER WITH A 40% OPEN AREA AND A SUPPLY AIR PRESSURE OF 2 BAR.	95
TABLE 18: VOLUME FLOW RATE AND MASS FLOW RATE FOR THE SMALL HOLE DIAMETER WITH A 51% OPEN AREA AND A SUPPLY AIR PRESSURE OF 0 BAR.	96
TABLE 19: VOLUME FLOW RATE AND MASS FLOW RATE FOR THE SMALL HOLE DIAMETER WITH A 51% OPEN AREA AND A SUPPLY AIR PRESSURE OF 0.5 BAR.	97
TABLE 20: VOLUME FLOW RATE AND MASS FLOW RATE FOR THE SMALL HOLE DIAMETER WITH A 51% OPEN AREA AND A SUPPLY AIR PRESSURE OF 1 BAR.	98
TABLE 21: VOLUME FLOW RATE AND MASS FLOW RATE FOR THE SMALL HOLE DIAMETER WITH A 51% OPEN AREA AND A SUPPLY AIR PRESSURE OF 1.5 BAR.	99
TABLE 22: VOLUME FLOW RATE AND MASS FLOW RATE FOR THE SMALL HOLE DIAMETER WITH A 51% OPEN AREA AND A SUPPLY AIR PRESSURE OF 2 BAR.	99
TABLE 23: VOLUME FLOW RATE AND MASS FLOW RATE FOR THE LARGE HOLE DIAMETER WITH A 51% OPEN AREA AND A SUPPLY AIR PRESSURE OF 0 BAR.	100
TABLE 24: VOLUME FLOW RATE AND MASS FLOW RATE FOR THE LARGE HOLE DIAMETER WITH A 51% OPEN AREA AND A SUPPLY AIR PRESSURE OF 0.5 BAR.	101
TABLE 25: VOLUME FLOW RATE AND MASS FLOW RATE FOR THE LARGE HOLE DIAMETER WITH A 51% OPEN AREA AND A SUPPLY AIR PRESSURE OF 1 BAR.	102
TABLE 26: VOLUME FLOW RATE AND MASS FLOW RATE FOR THE LARGE HOLE DIAMETER WITH A 51% OPEN AREA AND A SUPPLY AIR PRESSURE OF 1.5 BAR.	103
TABLE 27: VOLUME FLOW RATE AND MASS FLOW RATE FOR THE LARGE HOLE DIAMETER WITH A 51% OPEN AREA AND A SUPPLY AIR PRESSURE OF 2 BAR.	104
TABLE 28: UNCERTAINTY ANALYSIS FOR THE PARTICULATE MASS FLOW OF THE 40% OPEN AREA WITH A SMALL DIAMETER.	106
TABLE 29: UNCERTAINTY ANALYSIS FOR PARTICULATE MASS FLOW OF THE 40% OPEN AREA WITH A LARGE DIAMETER.	106

TABLE 30: UNCERTAINTY ANALYSIS FOR PARTICULATE MASS FLOW OF THE 51% OPEN AREA WITH A SMALL DIAMETER.....	106
TABLE 31: UNCERTAINTY ANALYSIS FOR PARTICULATE MASS FLOW OF THE 51% OPEN AREA WITH A LARGE DIAMETER.....	106
TABLE 32: FLUIDIZATION HEIGHT FOR A PERFORATED DISC WITH A 51% OPEN AREA.....	113
TABLE 33: FLUIDIZATION HEIGHT FOR A PERFORATED DISC WITH A 40% OPEN AREA.....	113
TABLE 34: AIR VELOCITIES IN FPM AT THE OUTLET NEAR THE WALL AND AT THE CENTER OF THE PIPE FOR A 2-PSI INLET PRESSURE.....	123
TABLE 35: AIR VELOCITIES IN FPM AT THE OUTLET NEAR THE WALL AND AT THE CENTER OF THE PIPE FOR A 5-PSI INLET PRESSURE.....	124
TABLE 36: AIR VELOCITIES IN FPM AT THE OUTLET NEAR THE WALL AND AT THE CENTER OF THE PIPE FOR A 10-PSI INLET PRESSURE.....	125
TABLE 37: AIR VELOCITIES IN FPM AT THE OUTLET NEAR THE WALL AND AT THE CENTER OF THE PIPE FOR A 20-PSI INLET PRESSURE.....	126
TABLE 38: AIR VELOCITIES IN FPM AT THE OUTLET NEAR THE WALL AND AT THE CENTER OF THE PIPE FOR A 30-PSI INLET PRESSURE.....	127
TABLE 39: AIR VELOCITIES IN FPM AT THE OUTLET NEAR THE WALL AND AT THE CENTER OF THE PIPE FOR A 40-PSI INLET PRESSURE.....	128
TABLE 40: AIR VELOCITIES IN FPM AT THE OUTLET NEAR THE WALL AND AT THE CENTER OF THE PIPE FOR A 50-PSI INLET PRESSURE.....	129
TABLE 41: AVERAGE VELOCITY MEASURED AT EACH INLET PRESSURE.....	132

LIST OF FIGURES

FIGURE 1: THE SOLAR IRRADIANCE ON AN ANNUAL AND DAILY SUM, SHOWING WHICH AREAS HAVE THE GREATEST POTENTIAL FOR SOLAR POWER [3].	4
FIGURE 2: TYPES OF CONCENTRATING SOLAR POWER TECHNOLOGIES. THE TOP ROW SYSTEMS ARE LINE CONCENTRATORS AND THE BOTTOM ROW SYSTEMS ARE POINT CONCENTRATORS [4].	5
FIGURE 3: DESIGN OF THE SOLAR TOWER SYSTEM CURRENTLY BUILT IN SAUDI ARABIA.	7
FIGURE 4: RESEARCH PAPERS FROM 1970 TILL 2017 RELATED TO CONCENTRATED SOLAR POWER IN SCOPUS.	10
FIGURE 5: TEMPERATURE RANGE OF DIFFERENT SUBSYSTEMS IN A SOLAR POWER PLANT (HTF: HEAT TRANSFER FLUID) [11].	11
FIGURE 6: SCHEMATIC OF THE PROMOTES SYSTEM [12].	12
FIGURE 7: SCHEMATIC OF THE SOLAR TOWER SYSTEM, SHOWING THE THREE MAIN SYSTEMS AND MANY OF THE COMPONENTS.	13
FIGURE 8: SCHEMATIC OF A FIXED BED HEAT EXCHANGER [15].	15
FIGURE 9: SCHEMATIC OF A MOVING BED HEAT EXCHANGER, HAVING A DIRECT CONTACT BETWEEN A GAS AND A SOLID [16].	17
FIGURE 10: AN EXAMPLE OF A CROSSFLOW HORIZONTAL MOVING BED HEAT EXCHANGER USED IN FOOD DRYERS [22].	19
FIGURE 11: AN EXAMPLE OF A VERTICAL CROSSFLOW MOVING BED HEAT EXCHANGER [23].	19
FIGURE 12: A SCHEMATIC OF A VERTICAL COUNTER FLOW MOVING BED HEAT EXCHANGER.	20
FIGURE 13: AN EXAMPLE OF A RADIAL FLOW MOVING BED CATALYST REACTOR USED IN THE CHEMICAL INDUSTRY [24].	20
FIGURE 14: A DIAGRAM TO ILLUSTRATE A FLUID BED REACTOR. ON THE LEFT SIDE, THE PARTICLES ARE AT REST. ON THE RIGHT SIDE, THE PARTICLES ARE NOW ACTING AS A FLUID, AS THE GASEOUS REACTANTS PASS THROUGH THE SOLID [15].	22
FIGURE 15: MULTISTAGE FLUIDIZED BED HEAT EXCHANGER THAT WAS STUDIED BY SERI [25].	23

FIGURE 16: TYPES OF BAFFLES USED IN HEAT EXCHANGERS. (A) SINGLE SEGMENTED BAFFLES, (B) DOUBLE SEGMENTED BAFFLES, AND (C) DISC AND DONUT BAFFLES [26].	24
FIGURE 17: TYPES OF BAFFLE CUTS THAT CAN BE INSERTED IN THE HEAT EXCHANGER [26].	25
FIGURE 18: BAFFLE ALIGNMENT AND SPACING IN A HEAT EXCHANGER [26].	26
FIGURE 19: SCHEMATIC SHOWING HOW MOST OF A FLUID WILL FLOW THROUGH A DISC AND DONUT BAFFLE DESIGN [28].	27
FIGURE 20: DRAG CURVE FOR MOTION OF A SPHERE IN A FLUID [29].	29
FIGURE 21: FREE BODY DIAGRAM OF THE PARTICLE WHILE FALLING DUE TO GRAVITY IN THE HEAT EXCHANGER.	30
FIGURE 22: GELDART’S PARTICLE CLASSIFICATION [31].	34
FIGURE 23: SCHEMATICS OF VARIOUS FLUIDIZATION REGIMES [31].	35
FIGURE 24: SCHEMATIC SHOWING THE HYDRODYNAMIC VOLUME OF A PARTICLE [29].	36
FIGURE 25: EXPERIMENTAL SETUP TO VISUALIZE THE PARTICULATE FLOW AND TEST THE MINIMAL FLUIDIZATION VELOCITY EQUATION.	41
FIGURE 26: PRESSURE GAUGE USED TO MEASURE THE AIR PRESSURE AT THE INLET.	42
FIGURE 27: PARTICLE COLUMN MARKED AT SPECIFIC INTERVALS TO MAKE IT EASIER TO READ THE HEIGHT OF THE BED.	42
FIGURE 28: EXPERIMENTAL AND THEORETICAL PRESSURE DROPS VALUES FOR MOVING BED OF PARTICULATES IN A VERTICAL COLUMN.	45
FIGURE 29: TRANSPARENT PVC PIPE THAT WAS USED IN THE EXPERIMENT.	48
FIGURE 30: INTERNAL PARTS FOR THE CONICAL DESIGN OF THE HEAT EXCHANGER.	48
FIGURE 31: CONICAL DESIGN MADE ON SOLIDWORKS.	49
FIGURE 32: DISC AND DONUT DESIGN MADE ON SOLIDWORKS.	50
FIGURE 33: ZIGZAG DESIGN MADE ON SOLIDWORKS.	51
FIGURE 34: CHEVRON DESIGN MADE ON SOLIDWORKS.	52
FIGURE 35: SIDE VIEW OF THE CHEVRON DESIGN FOR THE HEAT EXCHANGER.	53
FIGURE 36: SIDE VIEW OF THE SQUARE TUBES GRID DESIGN FOR THE HEAT EXCHANGER.	54

FIGURE 37: SIDE VIEW OF THE CIRCULAR TUBES GRID DESIGN FOR THE HEAT EXCHANGER.	54
FIGURE 38: SIDE VIEW OF THE TRIANGULAR TUBES GRID DESIGN FOR THE HEAT EXCHANGER.....	55
FIGURE 39: PERFORATED CORRUGATED SHEETS THAT CAN BE USED IN THE HEAT EXCHANGER.....	55
FIGURE 40: SCHEMATIC OF A HELICAL STATIC MIXER, WHICH IS MOSTLY USED IN THE CHEMICAL INDUSTRY [40].....	56
FIGURE 41: FIRST TYPE OF A CROSS ZIGZAG STATIC MIXER DESIGN THAT IS USED IN SMALLER HEAT EXCHANGERS [40].	57
FIGURE 42: SECOND TYPE OF A CROSS ZIGZAG STATIC MIXER DESIGN THAT IS USED IN LARGER HEAT EXCHANGERS [40].	57
FIGURE 43: PERFORATED PLATE THAT WAS USED IN ONE OF THE DIRECT CONTACT HEAT EXCHANGER DESIGN.	58
FIGURE 44: STEEL WIRE MESH THAT WAS USED IN ONE OF THE DIRECT CONTACT HEAT EXCHANGER DESIGN.	59
FIGURE 45: ALUMINUM FOAM OR POROUS STRUCTURE.	59
FIGURE 46: DIRECTIONAL POROUS STRUCTURE, THE MATERIAL USED HERE WAS CERAMICS.	60
FIGURE 47: RIGHT ANGLED HEAT EXCHANGER DESIGN (STANDARD ORIENTATION).	61
FIGURE 48: TILTED HEAT EXCHANGER DESIGN.	62
FIGURE 49: VANE ANEMOMETER THAT IS USED TO MEASURE THE AIR OUTLET IN THE EXPERIMENT.....	66
FIGURE 50: ROTAMETER THAT IS USED TO MEASURE THE SUPPLY AIR IN THE EXPERIMENT.....	66
FIGURE 51: PRESSURE GAUGE THAT IS USED TO MEASURE THE PRESSURE INLET IN THE EXPERIMENT.	67
FIGURE 52: THE FIRST ITERATION OF THE EXPERIMENT.....	68
FIGURE 53: SCHEMATIC OF THE FIRST ITERATION OF THE EXPERIMENT.....	69
FIGURE 54: THE 6 IN DIAMETER PVC Y-FITTING THAT WAS USED IN THE SECOND ITERATION OF THE APPARATUS FOR THE AIR OUTLET CONNECTION.	71
FIGURE 55: THE THIRD ITERATION OF THE APPARATUS.	73
FIGURE 56: SCHEMATIC OF THE THIRD ITERATION OF THE EXPERIMENT.....	74
FIGURE 57: THE MATERIAL COLUMN THAT IS USED TO BE ATTACHED TO THE TOP OF THE APPARATUS.	75

FIGURE 58: GATE VALVE THAT IS USED IN THE EXPERIMENT.....	76
FIGURE 59: PERFORATED DISC HOLDER IN ITS ASSEMBLED POSITION.	77
FIGURE 60: PERFORATED DISC HOLDER IN ITS DISASSEMBLED POSITION.	77
FIGURE 61: A 2 IN. Y-FITTING AIR CONNECTION FOR THE EXPERIMENT.	78
FIGURE 62: HEAT EXCHANGER MODULE USED IN THE EXPERIMENT.....	79
FIGURE 63: HEAT EXCHANGER MODULE DETACHED FROM THE SYSTEM.	80
FIGURE 64: PARTICLE DISTRIBUTOR USED ON TOP OF THE HEAT EXCHANGER MODULE.....	80
FIGURE 65: PRESSURE GAUGE ATTACHED TO THE INLET AND WITH A CAMERA RECORDER.	81
FIGURE 66: STORAGE BIN WITH A RELEASE VALVE TO REUSE THE PARTICULATES.	82
FIGURE 67: PARTICULATES STATICALLY CHARGED AFTER SEVERAL RUNS THROUGH THE APPARATUS.	83
FIGURE 68: COPPER WIRE USED TO DISCHARGE THE PARTICULATES AND MINIMIZE ANY STATIC CHARGES....	83
FIGURE 69: A PERFORATED 2 IN DISC THAT HAS A 51% OPEN AREA, WITH A HOLE DIAMETER OF 0.14 IN (SMALL DIAMETER).....	85
FIGURE 70: A PERFORATED 2 IN DISC THAT HAS A 51% OPEN AREA, WITH A HOLE DIAMETER OF 0.1875 IN (LARGE DIAMETER).....	85
FIGURE 71: A PERFORATED 2 IN DISC THAT HAS A 40% OPEN AREA, WITH A HOLE DIAMETER OF 0.125 IN (SMALL DIAMETER).....	86
FIGURE 72: A PERFORATED 2 IN DISC THAT HAS A 40% OPEN AREA, WITH A HOLE DIAMETER OF 0.25 IN (LARGE DIAMETER).....	86
FIGURE 73: GRAPH SHOWING THE 40% OPEN AREA MASS FLOW RATES BOTH FOR THE SMALL AND LARGE HOLE DIAMETERS.....	107
FIGURE 74: GRAPH SHOWING THE 51% OPEN AREA MASS FLOW RATES BOTH FOR THE SMALL AND LARGE HOLE DIAMETERS.....	109
FIGURE 75: GRAPH SHOWING THE 40% AND 51% OPEN AREA MASS FLOW RATES BOTH FOR THE SMALL AND LARGE HOLE DIAMETERS FOR EACH OPEN AREA.	110
FIGURE 76: ENTRAINMENT VELOCITIES FOR AN ABSOLUTE PRESSURE OF 0.5 BARS.....	115
FIGURE 77: ENTRAINMENT VELOCITIES FOR AN ABSOLUTE PRESSURE OF 1 BAR.	115

FIGURE 78: ENTRAINMENT VELOCITIES FOR AN ABSOLUTE PRESSURE OF 1.5 BARS.....	116
FIGURE 79: ENTRAINMENT VELOCITIES FOR AN ABSOLUTE PRESSURE OF 2 BARS.....	116
FIGURE 80: ENTRAINMENT VELOCITIES FOR AN ABSOLUTE PRESSURE OF 4 BARS.....	117
FIGURE 81: ENTRAINMENT VELOCITIES FOR AN ABSOLUTE PRESSURE OF 15.7 BARS.....	118
FIGURE 82: THERMO-ANEMOMETER (TSI VELOCICALC MODEL 8350) THAT WAS USED TO MEASURE THE AIR VELOCITIES IN THE PIPE.	119
FIGURE 83: LOCATION OF MEASUREMENT POINTS IN THE 2-IN. PIPE BOTH NEAR THE CENTER AND NEAR THE WALLS.	120
FIGURE 84: THERMO-ANEMOMETER THAT WAS USED TO MEASURE THE AIR VELOCITY AT TWO RADIAL LOCATIONS IN THE 2-IN. PIPE.	120
FIGURE 85: SCALE (OHAUS GT 210) THAT WAS USED TO MEASURE THE MASS OF THE PARTICLES ENTRAINED IN THE OUTLET FILTER.	121
FIGURE 86: AVERAGE AIR VELOCITY VS PERCENTAGE OF PARTICLES ENTRAINED AT VARIOUS INLET AIR SUPPLY PRESSURES.	130
FIGURE 87: MICROSCOPE THAT WAS USED TO MEASURE THE PARTICLE SIZES IN THE SAMPLE.	131
FIGURE 88: MICROSCOPIC VIEW OF THE SLIDE RULER THAT WAS USED UNDER THE MICROSCOPE TO MEASURE THE ENTRAINED PARTICLE SIZES.	132
FIGURE 89: PARTICLE SIZE DISTRIBUTION IN EACH SAMPLE DIVIDED INTO 100 MICROMETER SEGMENTS. ...	133
FIGURE 90: A SAMPLE MICROSCOPIC VIEW OF MEASURING THE PARTICLE SIZES USING THE MICROSCOPIC SLIDE RULER.	134
FIGURE 91: FLOW VISUALIZATION FOR CONICAL DESIGN, OBLIQUE TILTED VIEW.	137
FIGURE 92: FLOW VISUALIZATION FOR CONICAL DESIGN, OBLIQUE SIDE VIEW.	138
FIGURE 93: FLOW VISUALIZATION FOR DISC AND DONUT DESIGN, OBLIQUE TILTED VIEW.....	139
FIGURE 94: FLOW VISUALIZATION FOR DISC AND DONUT DESIGN, OBLIQUE SIDE VIEW.....	139
FIGURE 95: FLOW VISUALIZATION FOR ZIGZAG DESIGN, OBLIQUE TILTED VIEW.....	140
FIGURE 96: FLOW VISUALIZATION FOR ZIGZAG DESIGN, OBLIQUE SIDE VIEW.....	141
FIGURE 97: FLOW VISUALIZATION FOR CHEVRONS DESIGN, OBLIQUE TILTED VIEW.	141

FIGURE 98: FLOW VISUALIZATION FOR CHEVRONS DESIGN, OBLIQUE SIDE VIEW.	142
FIGURE 99: UNIFORM FLOW THROUGH THE WYE SECTION, SHOWING THE INDIVIDUAL PARTICLE STREAMS THAT WERE MADE BY THE PERFORATED PLATE.	143
FIGURE 100: PARTICLES ARE DISTRIBUTED, THUS DIFFICULT TO OBSERVE USING STILL PICTURES. THE SMALL RED CIRCLE SHOWS A GROUP OF PARTICLES (SHOWN AS A DARKER REGION OF THE HEAT EXCHANGER). THE LARGER RED CIRCLE SHOWS THE PARTICLES THAT ARE TRAPPED IN BETWEEN THE PERFORATED PLATE AND THE PVC TUBE.	144
FIGURE 101: PARTICLE FLOW THROUGH THE HEAT EXCHANGER, PARTICLES CAN BE SEEN DISPERSED AND SHOW A GOOD DISTRIBUTION WHILE FALLING.	144
FIGURE 102: ANOTHER FIGURE SHOWING THE GOOD DISTRIBUTION OF THE PARTICLE FLOW IN THE HEAT EXCHANGER.	145
FIGURE 103: ROTARY PADDLE VALVE [50].	149
FIGURE 104: BUTTERFLY VALVE [51].	150
FIGURE 105: GATE VALVE WITH THE SELF-CLEANING MECHANISM [53].	151
FIGURE 106: T-VALVE WITH A SELF-CLEANING MECHANISM [54].	151
FIGURE 107: SCHEMATIC OF PINCH VALVE IN OPERATION [56].	152
FIGURE 108: ROTATING POCKET VALVE CONCEPTUAL DESIGN, SIDE VIEW.	153
FIGURE 109: ROTATED DIAPHRAGM VALVE [58].	154
FIGURE 110: PARTICLE BRIDGING FOR PARTICLE FLOW CONTROL.	154
FIGURE 111: SCHEMATIC OF SOLAR TOWER SYSTEM, SHOWING ALL THE VALVE LOCATIONS.	156
FIGURE 112: SCHEMATIC OF VALVE AIRLOCK SYSTEM [59].	157
FIGURE 113: SCHEMATIC OF THE AIRLOCK CHAMBER FOR THE DUAL T-VALVE AIRLOCK SYSTEM [60].	158
FIGURE 114: GRAPH SHOWING THE HEIGHT OF AIRLOCK CHAMBER FOR BOTH ACCUCAST ID50 AND COBALT FOR THE VARIOUS NUMBER OF CYCLES PER MINUTE.	159
FIGURE 115: SOLAR TOWER SYSTEM IN SAUDI ARABIA.	164
FIGURE 116: SCHEMATIC OF THE SOLAR TOWER SYSTEM THAT IS CURRENTLY INSTALLED.	164

LIST OF EQUATIONS

Equation 1	26
Equation 2	27
Equation 3	27
Equation 4	28
Equation 5	28
Equation 6	28
Equation 7	28
Equation 8	30
Equation 9	30
Equation 10	30
Equation 11	30
Equation 12	31
Equation 13	32
Equation 14	32
Equation 15	34
Equation 16	34
Equation 17	35
Equation 18	36
Equation 19	36
Equation 20	36
Equation 21	36
Equation 22	37

Equation 23	37
Equation 24	37
Equation 25	39
Equation 26	64
Equation 27	105

LIST OF SYMBOLS AND ABBREVIATIONS

B_s BAFFLE SPACING

D_s SHELL DIAMETER

F_D DRAG FORCE

F_s SHEAR STRESS DRAG FORCE

F_g GRAVITY FORCE

x SPHERE DIAMETER

μ FLUID VISCOSITY

U TERMINAL VELOCITY FOR A SINGLE PARTICLE

Re_p REYNOLDS NUMBER FOR A SINGLE PARTICLE

C_D DRAG COEFFICIENT

ρ_f DENSITY OF FLUID

R' FORCE PER PROJECTED AREA ON A SPHERICAL PARTICLE

ρ_p DENSITY OF THE PARTICLE

g ACCELERATION DUE TO GRAVITY

P PRESSURE

A_{CS} CROSS-SECTIONAL AREA

H HEIGHT OF BED

ε VOID FRACTION

Ar ARCHIMEDES NUMBER

r SPHERE RADIUS

μ_s SUSPENSION VISCOSITY

ρ_b BED DENSITY

x_p AVERAGE SPHERE DIAMETER

x_i DIAMETER OF A SINGLE SPHERE I

M_i MASS OF EACH PARTICLE

\dot{m}_p MASS FLOW RATE FOR THE PARTICLES

d_{out} OUTLET DIAMETER

ρ_A ABSOLUTE DENSITY OF A SINGLE PARTICLE

M_p MASS OF A SINGLE PARTICLE

V_{SM} VOLUME OF SOLID MATERIAL IN A SINGLE PARTICLE

CSP CONCENTRATED SOLAR POWER

EES ENGINEERING EQUATION SOLVER

HTF HEAT TRANSFER FLUID

PROMOTES HIGH PERFORMANCE REDUCTION/OXIDATION METAL OXIDES FOR
THERMOCHEMICAL ENERGY STORAGE

PHR PARTICLE HEATING RECEIVER

RTV RIYADH TECHNO VALLEY

CFD COMPUTATIONAL FLUID DYNAMICS

A AERATABLE PARTICLE CLASSIFICATION

B BUBBLES READILY PARTICLE CLASSIFICATION

C COHESIVE PARTICLE CLASSIFICATION

D INERTIAL PARTICLE CLASSIFICATION

PIV PARTICLE IMAGE VELOCIMETRY

U_A STATISTICAL UNCERTAINTY

U_B BIAS UNCERTAINTY

U_C COMBINED UNCERTAINTY

SUMMARY

This thesis will report on the conceptual and preliminary designs and performance analysis and preliminary cost estimation of a particle to fluid direct contact heat exchanger. Which will be used in a particle heating receiver-based concentrator for a solar tower power application with an air breathing gas turbine power block. The conceptual design will review existing designs, such as the disc and donut design, and innovative designs, such as a discrete structure porous fill. Particular emphasis will be on the consideration of particle introduction and removal technology as well as inlet particle distribution, including a scale model observations and evaluation. Another emphasis will be on particle retention to prevent damage to downstream system components, especially the gas turbine. One or more suitable designs will be identified, and an engineering performance and a cost model will be developed and compared. The most feasible design will be proposed for further research.

CHAPTER 1. INTRODUCTION

Energy demand has been rising for the past few decades in tremendous numbers. As our technologies advance and automate all our equipment in our homes, offices, and industries, we will be needing more energy. Due to climate change and the limited natural resources we have, we must attempt to move to more sustainable energy sources. The sun is one of the most stable natural energy sources, which if harnessed correctly can meet all of our demand needs. Another important aspect that we need to consider is climate change, due to the dependence on fossil fuels we have been producing a lot of carbon dioxide and other heat-trapping gases in the atmosphere. This lead to an increase in global temperatures, which will lead us to use even more electricity to cool our indoor environments. Therefore, the International Energy Agency has shown, with its recent efforts, that we need to increase the development of renewable energy sector [1].

One of the promising technologies of this sector is solar thermal power generation using concentrated solar power (CSP). CSP uses a set of mirrors or lenses to concentrate direct solar irradiance from a large area to a smaller area so that all the radiation is focused on a small area and thus concentrating energy. This energy is then used to heat a heat transfer fluid or medium that transfers that heat to another fluid that will be used to generate electricity. However, due to the fact that CSP technology uses direct solar irradiance, it would be very efficient only on specific locations where there will not be a lot of clouds, such as deserts. CSP systems are mostly used with a storage system or used in a hybrid system, to maintain nighttime operation [2]. Hybrid systems are systems that combine two technologies together. For example, a natural gas power plant can be combined with a solar

tower to form a hybrid system. The system will use solar energy in the day time and in the evening use natural gas.

1.1 Problem Statement

There is an increasing need for renewable energy systems today as the demand for energy is incredibly high and our carbon footprint is growing. A solution to help mitigate these problems is the use of solar tower power plants. Solar tower power plants use solar thermal energy from the sun to generate electricity. Solar tower power plants require a heat transfer fluid (HTF), which is a medium that the system is using to capture the heat from the sun. This HTF then passes through a heat exchanger with a fluid, to transfer the sun's heat to the fluid. The fluid then goes through a turbine to generate electricity. So, the higher the fluid temperature, the more electricity can be generated from the system. Therefore, in order to reach these high temperatures, there is a need for an effective heat exchanger that will transfer heat from the HTF to the fluid. Currently, most of these plants use an indirect contact heat exchanger which can be a high cost on the system. This is due to the fact that indirect contact heat exchangers, such as shell-and-tube or shell-and-plate require the use of expensive metal alloys. Furthermore, these types of heat exchangers also have a limited surface area compared to direct contact heat exchanger. Thus, my research focuses on developing a design for a direct contact heat exchanger that would effectively transfer heat from the HTF to the fluid, in this case the HTF is particulates and the fluid is air. This design will also help reduce the overall operational cost of the solar tower power plant and increase its efficiency. \

1.2 Objectives

The objective of this research is to develop a direct contact heat exchanger that will effectively transfer the heat from the particulates to the gas, to better understand particle flow dynamics, and to predict particle movements. This research will also help make solar tower power plants more efficient in generating electricity even after sunset.

Furthermore, this thesis will report on the conceptual and preliminary designs of a particle to fluid direct contact heat exchanger for use in solar tower application. A performance analysis and a preliminary cost estimation for the heat exchanger system in that application will be studied. The conceptual design will review existing designs such as the disc and donut design and innovative designs such as a discrete structure porous fill. Particular emphasis will be placed on particle introduction and removal technologies as well as inlet particle distribution including scale model observations and evaluation. Another emphasis will be on particle retention in the heat exchanger to prevent damage to down-stream components, especially the gas turbine. One or more suitable designs will be identified for an engineering performance and a cost model analysis. The most feasible design will be proposed for further research.

CHAPTER 2. BACKGROUND

2.1 Solar Thermal Energy

2.1.1 Solar Irradiance

The energy that the earth gets from the sun every day can generate enough electricity to power up all machinery on earth. Solar Irradiance is a measure of how much of solar radiation hits on the earth's surface per unit area. Most countries have an annual solar irradiation average of 1.6 MW-h/m² or higher, except for countries that are above the 45°N latitude or below the 45°S latitude. As shown in Figure 1, the solar irradiance and especially the beam component is, of course, most abundant in arid desert areas.

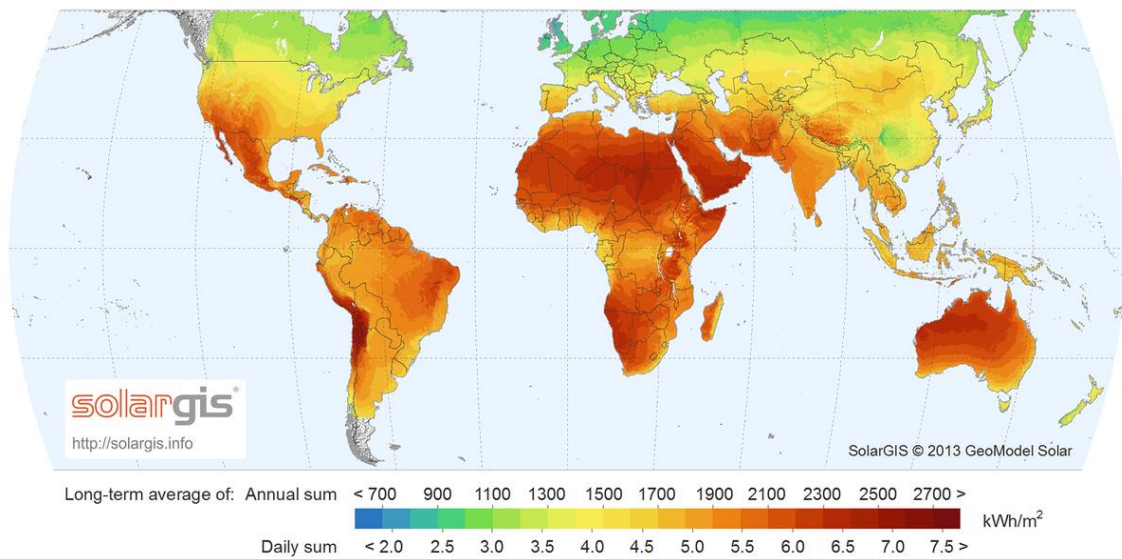


Figure 1: The solar irradiance on an annual and daily sum, showing which areas have the greatest potential for solar power [3].

2.1.2 Concentrated Solar Power Plants

Concentrated Solar Power (CSP) are systems that use mirrors or lenses to concentrate solar radiation onto a small area to generate solar thermal energy. CSPs are coupled with a heat engine or a turbine to generate electricity. There are four main types of CSP technology currently available; parabolic trough, faceted or Fresnel reflectors, dish collector, and solar tower, as can be seen in Figure 2. In some cases, CSP is used with a fossil fuel system to generate electricity in the morning while at night natural gas is used. In other cases, a storage system can be implemented to store the hot heat transfer fluid or medium and use that in the evening.

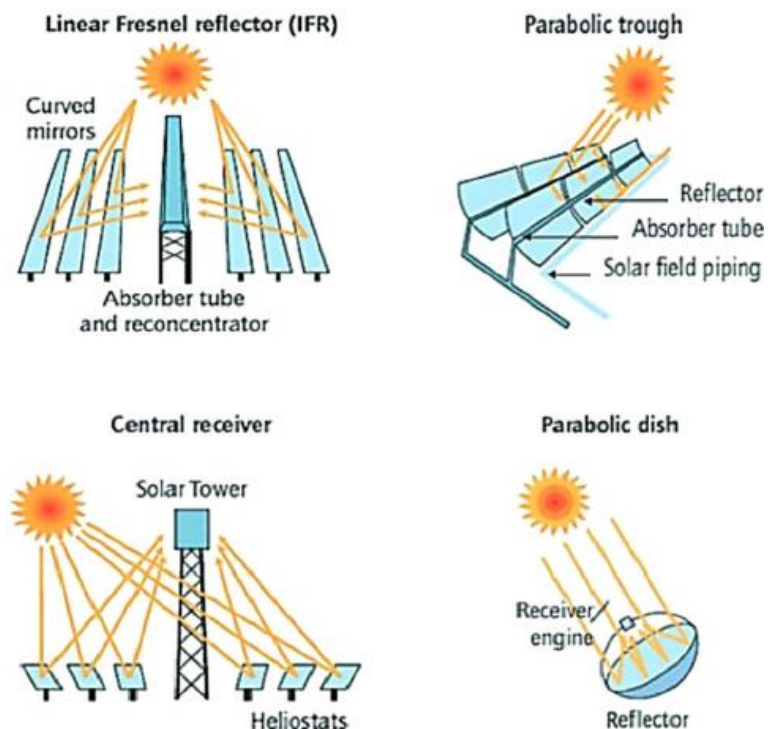


Figure 2: Types of concentrating solar power technologies. The top row systems are line concentrators and the bottom row systems are point concentrators [4].

The parabolic trough uses parabolic mirrors to concentrate the light onto a line, where the heat transfer fluid, commonly molten salt, is heated. The system must be able to track the sun on one axis. Another system is an array of Fresnel reflectors, where flat mirrors are placed at different angles so that throughout the day the sun is concentrated onto a pipe, where the heat transfer fluid passes through. In the dish collector, the light is concentrated on a small area rather than on a line, the benefit of this is having to reach higher concentration ratios, which helps us in getting more solar energy per area. The dish collector uses a parabolic surface to concentrate light onto a Sterling engine to generate electricity. Similar to the dish collector, the solar tower also concentrates light on a small area. In the solar tower system, the system uses a number of flat or slightly mirrors, called heliostats, to concentrate the light into a small area on top of the tower. Each of the heliostats has a control or drive system to track the sun throughout the day. Another concentrator, in the tower, may be used to collect all the light coming from the heliostats onto the receiver. The solar tower can also use molten salt, water, air, or particulate as a medium. The solar tower has many advantages over other CSPs, these include lower operating cost, higher efficiency, and scale-up potential. Consequently, a lot of research is being done to improve solar tower performance and decrease the cost, as can be seen in Figure 4. An example of a solar tower system is shown in Figure 3, this is the current system that our team is working on.

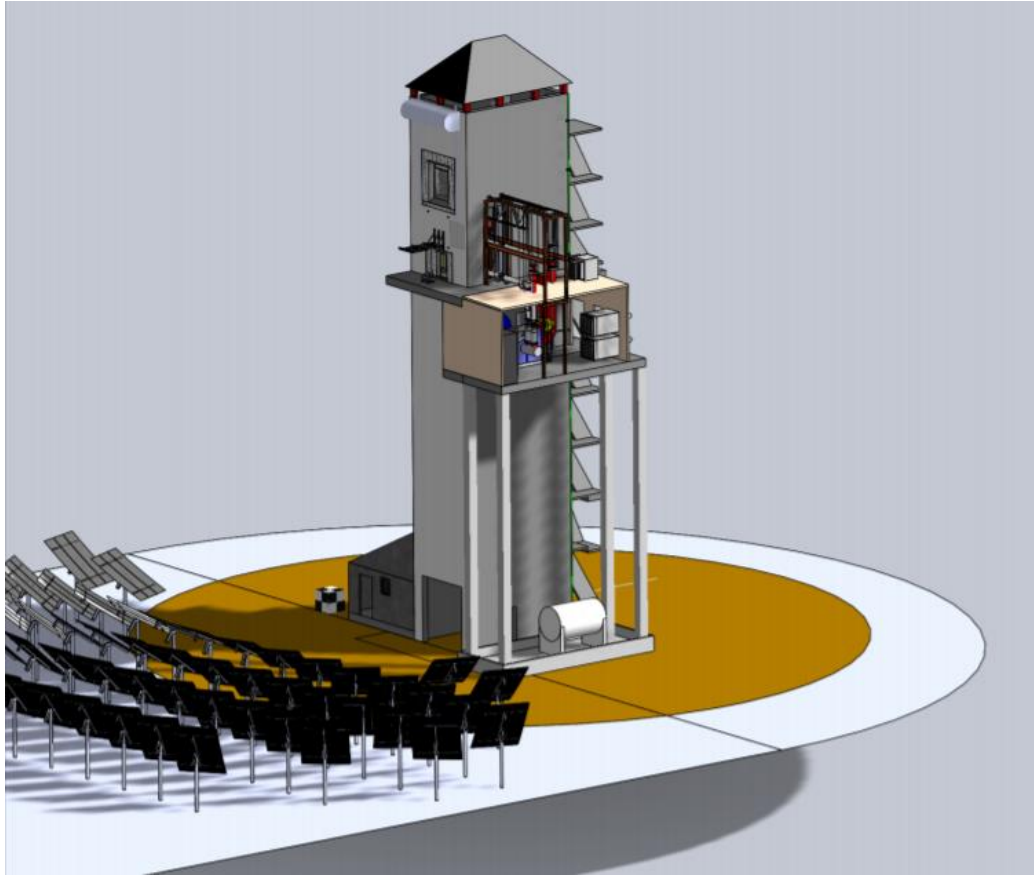






Figure 3: Design of the Solar Tower system currently built in Saudi Arabia.

Table 1: Comparison of various concentrating solar power technologies [5].

	Public Trough	Solar Tower	Linear Fresnel	Dish Stirling
	 [6]	 [7]	 [8]	 [9]
Typical Capacity (MW)	10-300	10-200	10-200	0.01-0.025
Maturity of Technology	Commercially proven	Pilot Commercial projects	Pilot projects	Demonstration projects
Technology Development Risk	Low	Medium	Medium	Medium
Operating temperature (°C)	350-550	250-565	390	550-750
Plant Peak Efficiency (%)	14-20	23-35	18	30
Collector Concentration	70-80 suns	>1000 suns	>60 suns	>1300 suns
Receiver	Receiver attached to collector	Cavity or external receiver fixed at top of tower	Fixed receiver	Receiver attached to collector

2.1.3 Storage in Solar Power Towers

By using thermal-energy storage in solar power towers, they have the advantage of continuously generating power regardless of demand. Storage can vary greatly depending on the type of heat transfer fluid used in the solar tower. For example, air is sometimes used as a heat transfer fluid by having the receiver, which is heated up by the sun's radiation, and then passing air through it. The air is then used to run a turbine, and excess air is used as storage [10]. Molten salts are also other heat transfer mediums that have been used extensively for storage. However, a more efficient heat transfer fluid is the use of packed beds made out of ceramic material, these systems are simple and can stand up to 800°C but are more expensive. Another similar heat transfer fluid or medium with a high heat capacity is sand; it is also cheaper as it is found in abundance [10].

2.1.4 Particulates as a Heat Transfer Fluid

There are many disadvantages when using molten salts as a heat transfer fluid in CSPs, thus there is a lot of current research in having alternatives for the heat transfer fluid. Particulates or powders have been mentioned as a heat transfer medium in the 1980s, but recently there has been a lot of research in using them because of their acceptable thermal and transport properties. They are also being currently investigated because particulates such as sand, are very cheap and easier to attain [11]. Figure 4, shows how starting from the year 2010, the number of published research about particulates in solar thermal systems has increased. The graph was developed by using Scopus database to search for specific keywords and check the number of peer-reviewed publications per year range. The

keywords used were: ‘Solar Plant Design’, ‘Solar Energy Application’, ‘PCM Energy Storage’, ‘Powders HTFs’, ‘Hybrid Solar Power Plants’, and ‘Thermo-chemical Energy Storage’ [11].

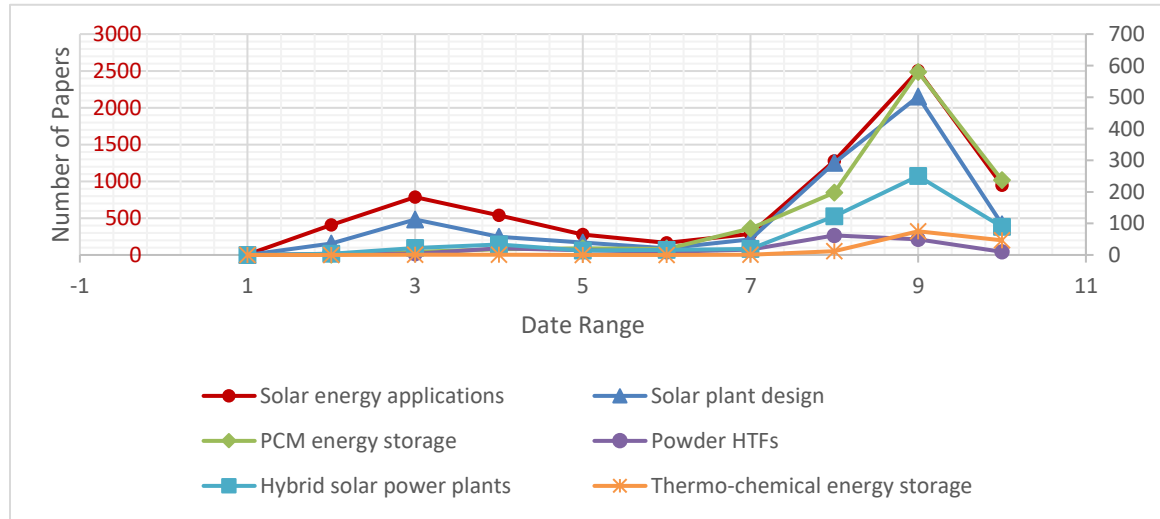


Figure 4: Research papers from 1970 till 2017 related to concentrated solar power in Scopus.

Another major advantage to the use of powders or granules as heat transfer “fluid” or medium is that they have a higher temperature limit. This results in higher overall efficiencies that could potentially be obtained from the thermodynamic cycle. Figure 4 shows that the use of powders, as a medium and in storage, has a wide range of operating temperatures. As can be seen, the use of gas or air as a heat transfer fluid could result in higher operating temperatures and thus higher thermodynamic efficiencies. However, the storage for gas or air is very challenging and consequently it is not yet being used today. Another important aspect is the technology risk as shown in Figure 5; since these technologies have not matured enough to be used in industry, operating at higher temperatures increases the technology risk [11]. Particulates have also been used in various

industries and applications, these include, chemical, food, energy, oil and gas, and agricultural industries. Therefore, this research will focus on particulates as a heat transfer medium in solar tower systems.

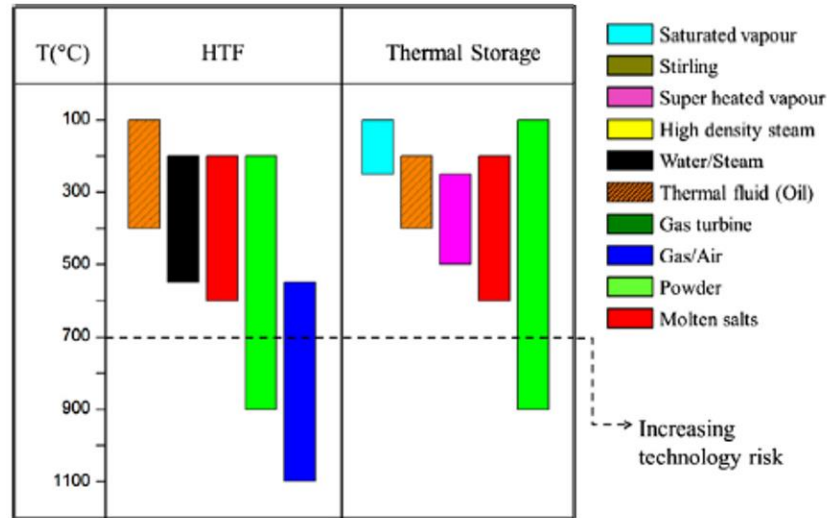


Figure 5: Temperature range of different subsystems in a solar power plant (HTF: heat transfer fluid) [11].

2.2 System Description

As shown in Figure 6, in this solar tower pilot project the particulates will start from the cold storage bin and will be transported to the top of the tower by a particle lift. The particles will be preheated using a direct contact heat exchanger and it would also oxidize the particles before falling onto the receiver. The receiver, which receives the solar irradiance from all the heliostats, will heat and reduce the particles through an endothermic reaction. Then the particles move to the hot storage bin, where particles would be stored for evening operations. After that the particles go through the main direct contact heat exchanger, where the particles would re-oxidize and the heat would be transferred from the particles to the air, going on to the turbine. Then after the heat transfer process, the particles

then fall into the cold storage bin where they go through the whole process again. In this particulate example, they are using a thermos chemical storage system which is different from our thermal storage system which does not include any oxidization in the process [12].

Some of the main points that summarize the system: the CSP system under consideration is a solar tower using a heliostat field. Furthermore, the heat transfer fluid or medium that will be used will be a particulate of the material (ACCUCAST ID50). Moreover, the cold and hot storage bin storage, as well as the heat exchanger, are enclosed in the tower structure and the particle lift will be outside the structure. Finally, the heat exchanger will be a direct contact heat exchanger between air and the particulate.

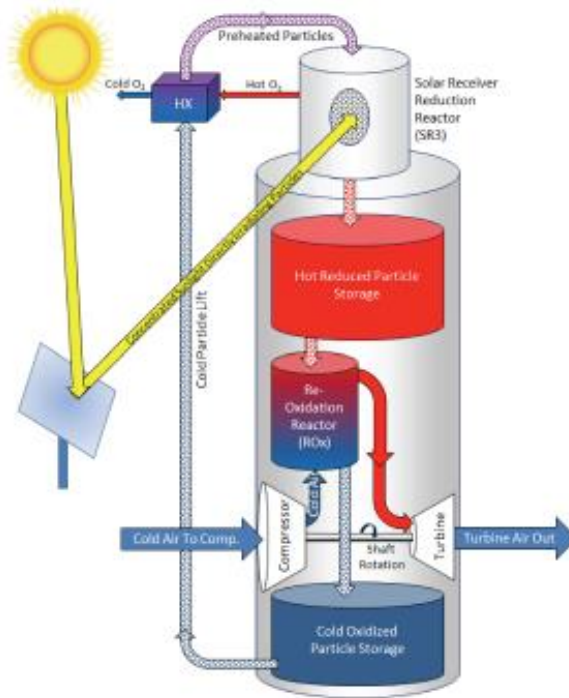


Figure 6: Schematic of the PROMOTES system [12].

Another schematic showing a more detailed view of the system as well as the three main systems in the prototype RTV solar tower is shown in Figure 7. The first system is the particle loop, shown in yellow, this shows how the particles flow from the top of the RTV tower till they are recycled at the bottom of the system and move back to the top. The second system is the air cycle, shown in blue and red, the cold air enters the direct contact heat exchanger and exits as hot air. Finally, a fuel cycle is added to the system, shown in green, to supplement the system.

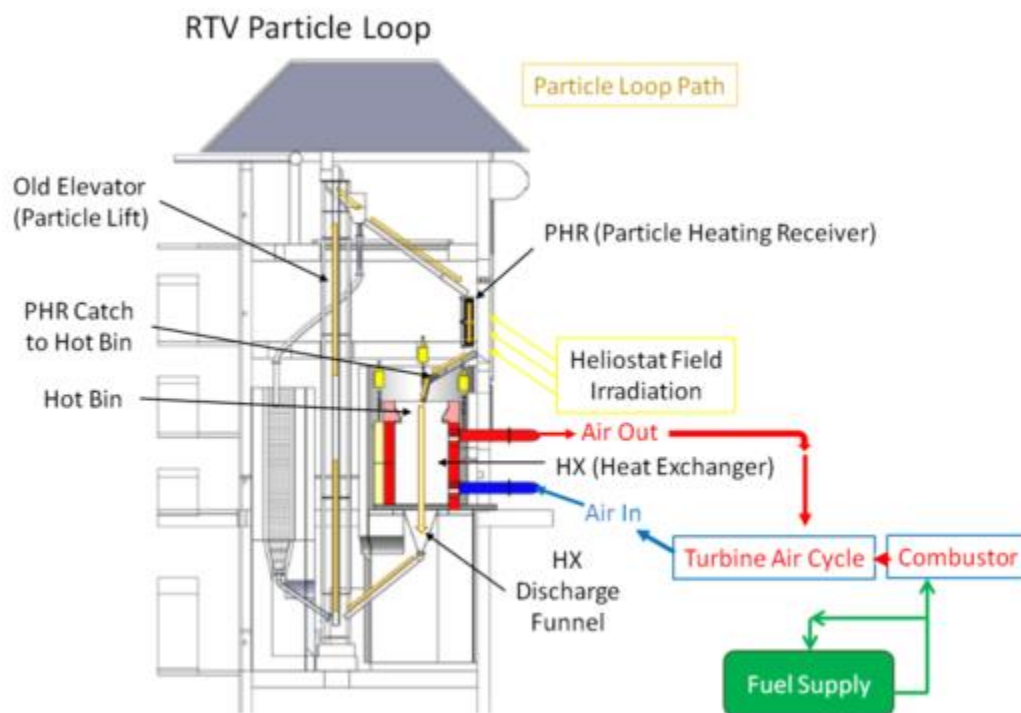


Figure 7: Schematic of the Solar Tower system, showing the three main systems and many of the components.

CHAPTER 3. LITERATURE REVIEW

3.1 Direct Contact Heat Exchangers

The direct contact heat exchanger uses two fluid streams that come into direct contact with each other. For this project, one of the streams is going to be a powder or granular and the other is going to be a gas. Compared to indirect heat exchangers which are currently used in solar towers, direct contact heat exchangers have numerous advantages. Some of these advantages include, the heat exchanger design becomes simpler and the construction as well as the maintenance becomes more economic. Secondly, the heat exchanger can achieve higher heat transfer rates since the two materials can mix together. This is due to the fact when particles are in direct contact with the gas the surface area becomes orders of magnitude larger. Lastly, in a direct contact heat exchanger, the fouling problem is eliminated as the heat exchanger internal design makes sure that there is no deposition of any material inside the heat exchanger [13].

3.1.1 Fixed Bed Heat Exchangers

A fixed bed heat exchanger would have a packed bed of particles in a tubular heat exchanger and would allow the gas to flow through the hot particles. This type of bed is typically used in the chemical industry between a catalyst and a reactant gas. In that process, a reaction between the reactants in the gas or vapor phase is mediated by the catalyst to produce the desired product. There are multiple configurations that can be employed to help maintain control of the temperature of the system. Another constraint that can occur in this type of heat exchanger is the pressure drop as the gas flows through

the bed. Another variable that some researchers have investigated, is the relative advantages of having an up flow or a downward flow across the bed. The up flow has a lower pressure drop and can help push fragmented particles to the top of the bed. However, using an up flow can lead to fluidization which makes the bed unsteady and can result in a pulsating flow. The downward flow has the advantage of ensuring a non-fluidized bed with a stable flow. However, the downward flow can increase compression in the bed and thus increased pressure drops [14].

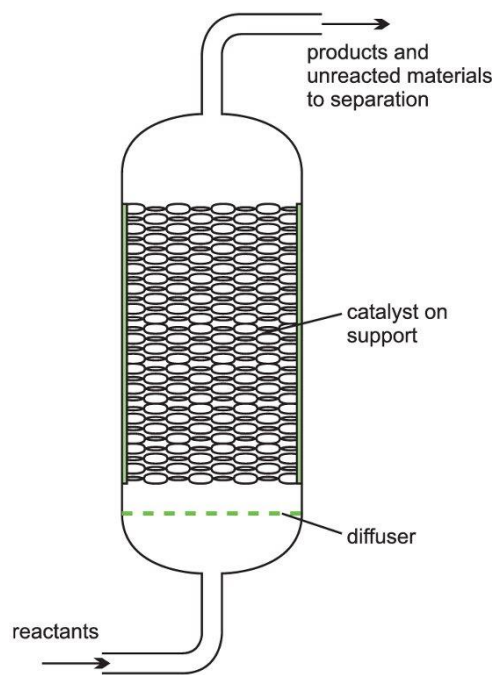


Figure 8: Schematic of a fixed bed heat exchanger [15].

3.1.2 Moving Bed Heat Exchanger

In a moving bed heat exchanger, particles fall downwards due to gravity in a plug flow. This means the bed moves together downwards and all particulates move approximately with the same velocity. The gas moves upward through the heat exchanger and the particulates, then exits from the top. The internal part of the heat exchanger can have various designs to slow down the particulate flow. Another method to slow down the particulate flow is by increasing the air velocity. After passing through the heat exchanger, the particulates are then removed from the bottom and recirculated to the top to re-enter the heat exchanger for another cycle. Furthermore, these types of heat exchangers need to maintain good control of particulate flow which requires special control valves for this kind for application. Moreover, the particulates need to be evenly distributed throughout the heat exchanger and thus good distribution techniques must be employed to supply an even flow of particulates [14].

For this application, this heat exchange can be classified as a moving bed heat exchanger, this type of exchanger, as mentioned in the above section, can be direct or indirect. Solid particles or powders are used in heat exchanger typically in energy and chemical industries. For example, ceramic solid particles can be used at very high temperatures because of their high melting temperatures and great heat capacity. Consequently, using these solid particles in a moving bed heat exchanger can be very advantageous. There are two types of moving bed heat exchangers, direct and indirect. In the direct moving bed heat exchanger, the particles encounter the gas or liquid and are then separated upon exit. However, the gas could have contaminants that would affect the heat

transfer process. In the indirect moving bed heat exchanger, the particles do not encounter the gas or fluid, and it is currently being employed in the industry [16].

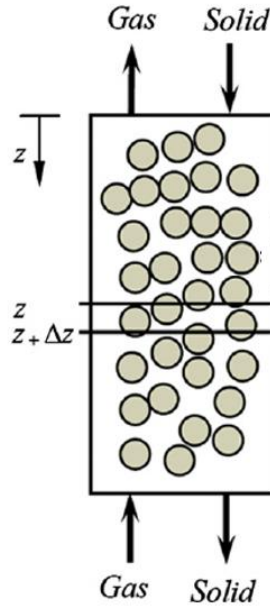


Figure 9: Schematic of a moving bed heat exchanger, having a direct contact between a gas and a solid [16].

Furthermore, the direction of the flow also affects the heat transfer occurring in the system. The flow can be classified either as a parallel or counter flow depending on its direction relative to the solid particles. Park also concluded that counter flow heat exchangers that are vertical have the highest heat exchanger effectiveness. His paper compared counter flow, parallel, and cross-flow type heat exchangers using numerical analyses [17]. The Figure 10, Figure 11, Figure 12, and Figure 13 show some examples of various airflow patterns. Consequently, in this study we will be using the direct contact counter flow heat exchanger, this due to several reasons. First, using a direct contact heat exchanger can achieve a much higher heat transfer effectiveness versus an indirect contact

heat exchanger. Further, manufacturing and maintaining a direct contact heat exchanger is more economic when compared to an indirect heat exchanger. Also, in a direct contact heat exchanger, the user can control the flow of particulates by changing the internal designs of the heat exchanger which is not possible in an indirect heat exchanger. Finally, using a counter flow heat exchanger design over other designs will help us separate particles from the air easier, have a lower pressure drop, and achieve a higher air outlet temperature [17].

The moving bed heat exchangers use two bins to control the flow of solid particles through the heat exchanger. The inlet air, in this case, is pumped from the bottom and exits at the top and the particles fall from the hot bin through the heat exchanger to the cold bin by gravity. The particle flow is controlled by a set of valves between each particle bin and the heat exchanger. Another advantage of this type of heat exchanger is that there are no moving parts which lower installation and maintenance costs [18].

Most of the previous work done on moving packed bed heat exchangers was done on specific applications and not for general design tools. A paper, written by Botterill and Denloye, showed that near the walls of a packed bed of particles there was a higher void fraction for the particles compared to the center. Consequently, this would lower the thermal conductivity near the walls of the heat exchanger [19]. Another paper, wrote by Henda and Falcioni, also examined the heat transfer in solid particles in a moving packed bed heat exchanger. However, rather than having two fluids, the paper modeled the heat transfer by having a specified wall temperature and measuring how much heat is transferred to the particles [20]. Additionally, Baumann and Zunft used computational fluid dynamics (CFD) tools to simulate a moving packed bed heat exchanger. They have concluded that the Eulerian-Eulerian model is the most accurate in simulating moving packed beds. This

is due to the fact that this model was compared to PIV measurements and showed that it captures the velocity profiles of particulates around the internal tubes [21].

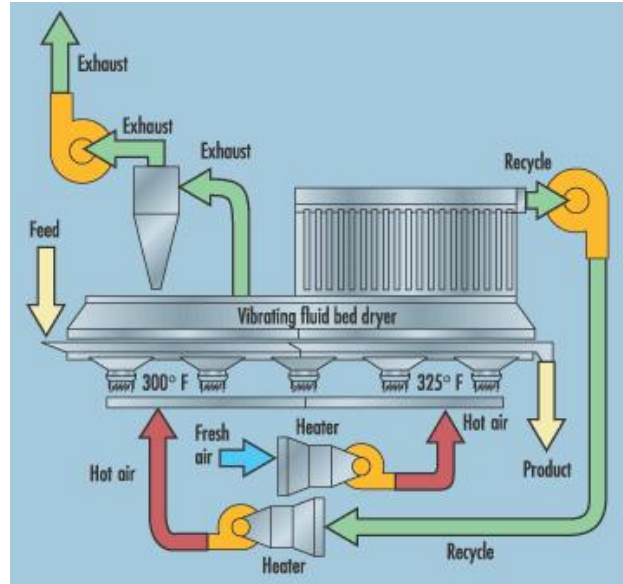


Figure 10: An example of a crossflow horizontal moving bed heat exchanger used in food dryers [22].

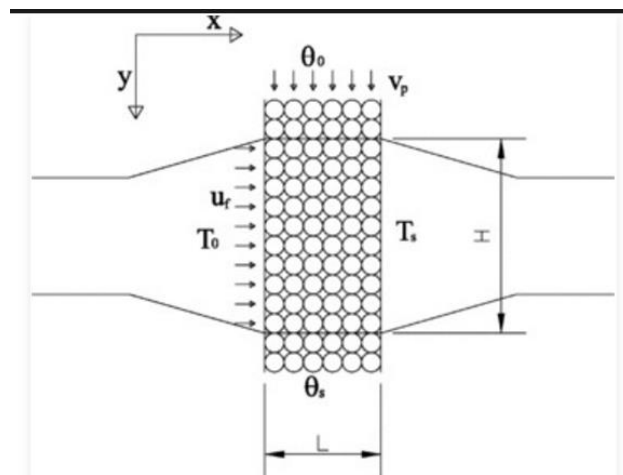


Figure 11: An example of a vertical crossflow moving bed heat exchanger [23].

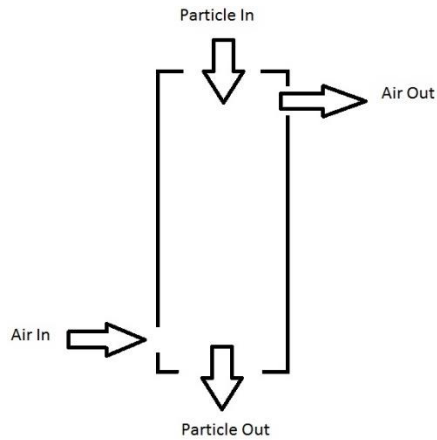


Figure 12: A schematic of a vertical counter flow moving bed heat exchanger.

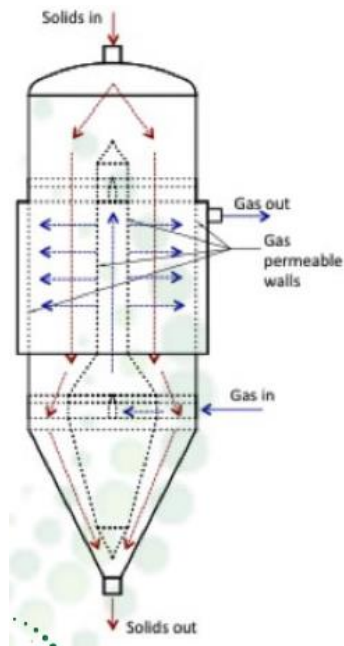


Figure 13: An example of a radial flow moving bed catalyst reactor used in the chemical industry [24].

3.1.3 Fluidized Bed Heat Exchangers

In a fluidized bed heat exchanger, particles are held in place using a supporting grid that does not allow them to fall downwards. Particles are fed into the heat exchanger from the top or side and are fed out of the heat exchanger from the bottom or side of the particle

bed. The grid allows air to go through but not particles and thus air can lift the particles from the grid till they reach the top of the bed. This upward motion of the particles creates a constant motion in the bed and therefore mixing occurs in all regions of the bed. The fluidized bed heat exchanger was first employed as a fluidized bed reactor in the petroleum industry for catalytic cracking to convert crude oil into gasoline and other products. The fluidized bed reactors are now used for both catalytic and non-catalytic reactions. Furthermore, the fluidized bed heat exchanger is best used when the particle size ranges from 10 to 300 microns [14]. However, knowing the particle size distribution is very important as beds with the same size particles fluidize poorly compared to beds with a good particle size distribution. In large beds, poor fluidization, such as slugging, spouting, and bumping, can have a great effect on the structure that is holding the bed. But, by employing a distribution of different particle diameters, the fluidization process can greatly be improved as this allows for better mixing in the bed and permits flexible operation [14].

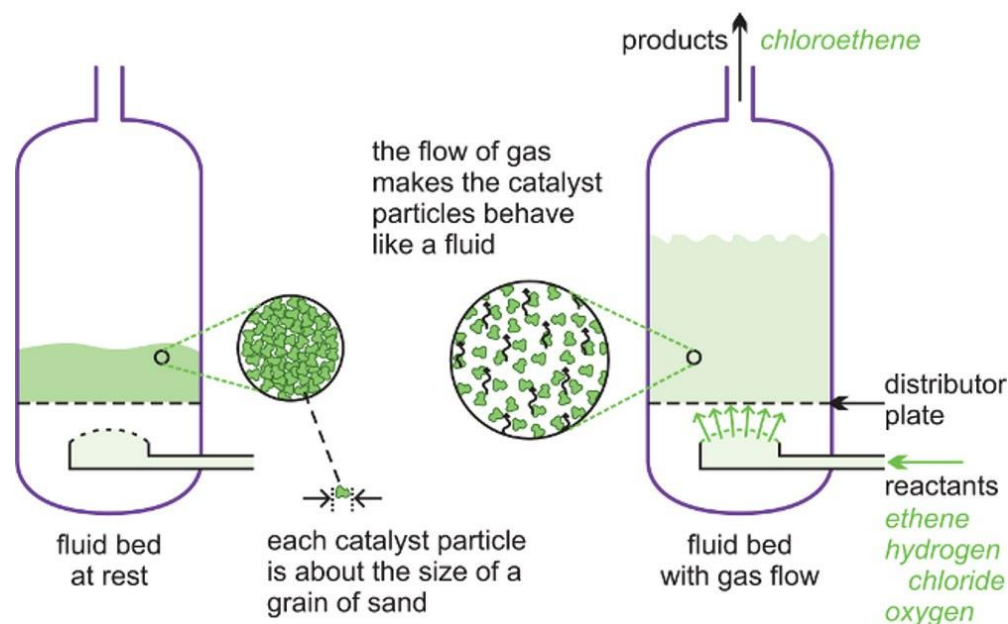


Figure 14: A diagram to illustrate a fluid bed reactor. On the left side, the particles are at rest. On the right side, the particles are now acting as a fluid, as the gaseous reactants pass through the solid [15].

Additionally, in the Solar Energy Research Institute (SERI) report the design of the heat exchanger was a direct contact heat exchanger but using a multistage fluidized bed as shown in Figure 15 [25]. The air inlet is still from the bottom of the heat exchanger and the outlet on top. But the air passes through several fluidized beds before exiting. The particulates enter from a pipe to the side of the heat exchanger in the first bed. The particulates then flow from one bed to another through the stand pipe as they are fluidized. The particulates moving through the pipe are not fluidized and flow from the top of the first bed to the bottom of the second bed. This multistage design is expensive and challenging to maintain. This design requires cyclone particle separators to ensure that there is no particle entrainment in the air flow that is going to the turbine. This is due to the fact that particulates movements and air flows can be very inconsistent in fluidized beds. Thus, resulting in higher risk of particle carry over in the air flow to the turbine.

Furthermore, their heat transfer analysis has not taken into consideration particle carryover nor the radiation heat transfer between each fluidized bed stage.

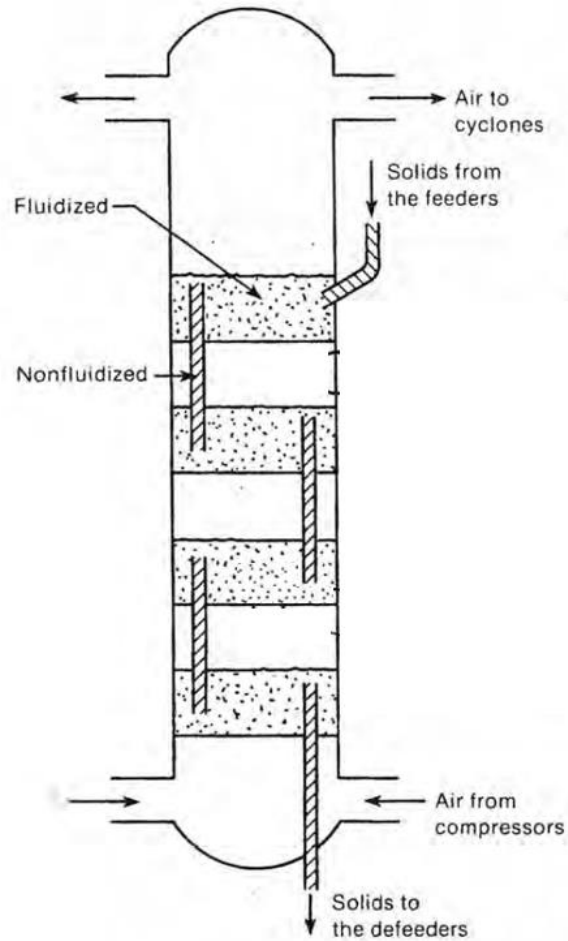


Figure 15: Multistage fluidized bed heat exchanger that was studied by SERI [25].

3.1.4 Baffles

In addition, I used baffles to decrease the flow of particulates and increase the heat transfer time. Baffles are mostly used in shell and tube heat exchangers to direct the fluid flow in the shell across the tubes. However, in this project, the baffles are used in a direct contact heat exchanger to decrease the particulate flow rate and increase the heat transfer time between the air and the particulates. There are many different types and shapes of baffles but the three most common ones are the single segmented baffle, the double segmented baffle, and the disc and doughnut baffle, as shown in Figure 16.

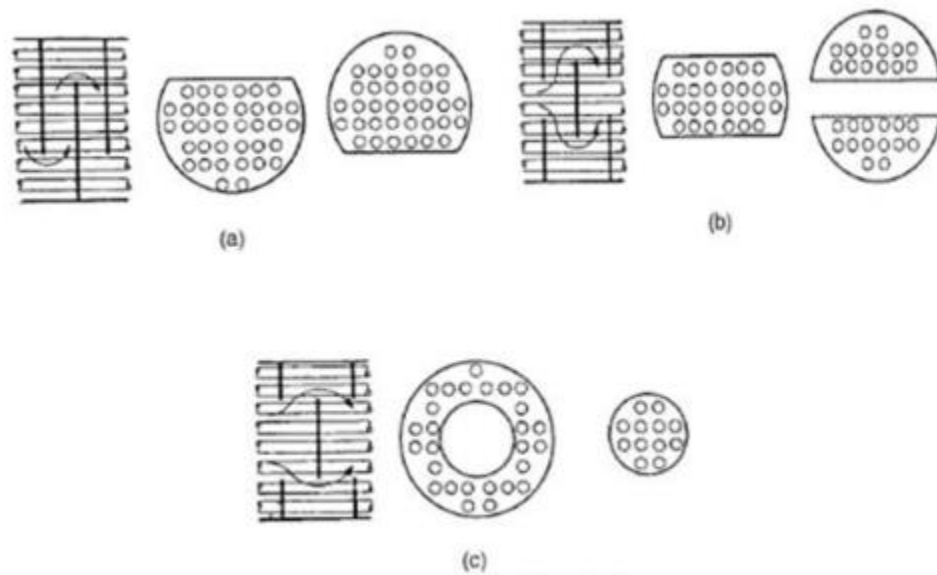


Figure 16: Types of Baffles used in heat exchangers. (a) Single segmented baffles, (b) Double segmented baffles, and (c) Disc and donut baffles [26].

The baffle diameter refers to the outer diameter of the baffle. To avoid shearing of the baffle, there must be a clearance between the shell, or inner diameter of the heat

exchanger, and the outer diameter of the baffle. Table 2 shows for each shell diameter its baffle diameter and tolerance.

Table 2: Baffle diameter and tolerances [26].

	Shell Diameter, D_s	Baffle Diameter	Tolerance
Pipe Shells	152 to 635 mm	$D_s - 1.6$ mm	+ 0.8 mm
Plate Shells	152 to 635 mm	$D_s - 3.2$ mm	+ 0.8 mm
	686 to 1067 mm	$D_s - 4.8$ mm	+ 1.6 mm

For segmented baffles, the baffle cuts make a huge difference on how the user wants to redirect the flow. But most of the time single segmented baffles have a 45% cut and double segmented baffles have a 25% cut as shown in Figure 17 [26].

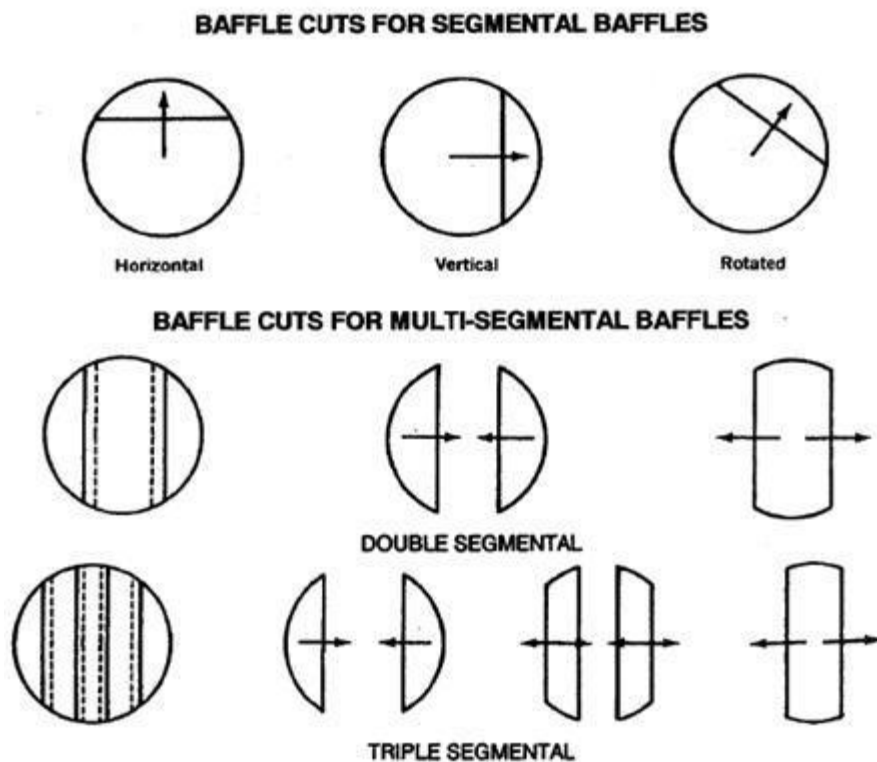


Figure 17: Types of baffle cuts that can be inserted in the heat exchanger [26].

Another important aspect is the baffle spacing in the heat exchanger and it is defined as the distance between two consecutive baffles, as shown in Figure 18. In shell and tube heat exchangers the typical baffle spacing ranges from 0.2 to 1 the size of the shell inner diameter. The smaller the baffle spacing in the heat exchanger the more time the fluid will need to exit the heat exchanger. This means that as the number of baffles in the heat exchanger increases, the heat transfer coefficient increases and the pressure drop is higher. The optimum spacing is commonly between 0.3 to 0.5 times size of the shell diameter; the equation defines the average baffle spacing for a given shell inner diameter.

$$B_s = 0.4(D_s) \quad (1)$$

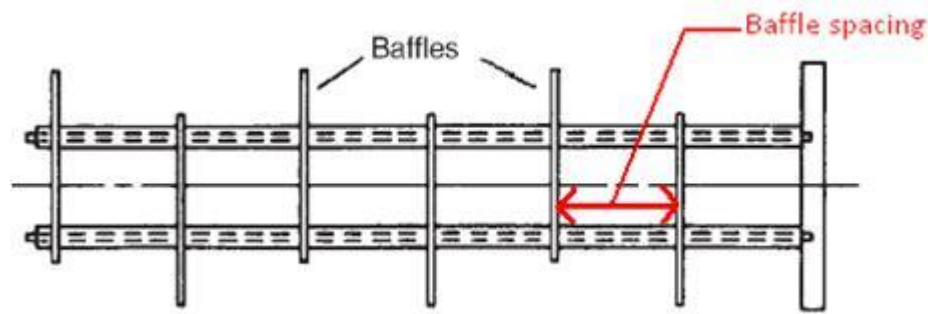


Figure 18: Baffle alignment and spacing in a heat exchanger [26].

Furthermore, Figure 19 shows how the direct contact heat exchanger will work with a disc and doughnut baffle. As shown in Figure 19 the particles will be able to flow through the baffles that is made of perforated plates. However, most of the air is expected to flow as shown with the green lines around the disc and doughnut baffles, a combination of counter and cross flow patterns [27].

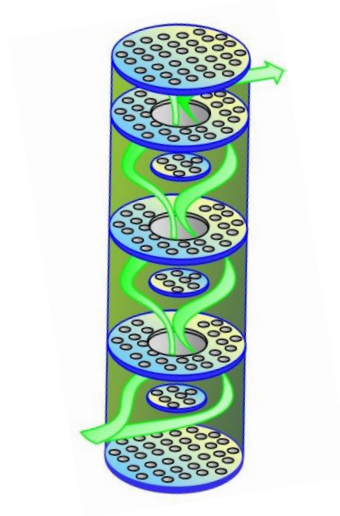


Figure 19: Schematic showing how most of a fluid will flow through a disc and donut baffle design [28].

3.2 Particulate Flow

3.2.1 *Falling Particles*

Particles falling from rest will initially experience high acceleration and this acceleration will then be decreased by the drag force to a point where forces will balance. When this occurs, the particle is said to have reached its terminal velocity, meaning the acceleration is zero. Since the particle in use is spherical we will only be using equations pertaining to spherical particles. By defining the net force on the particle as well as the drag force, we can drive the following equations:

$$F_{net} = -F_g + F_D \quad (2)$$

$$F_g = mg \quad (3)$$

$$F_D = \frac{CdApU^2}{2} \quad (4)$$

Because it is a vertical descent the acceleration with no forces acting on it, at terminal velocity the acceleration will be zero and the net forces acting on a single particle will be zero as well. Therefore, the velocity of the particle will be equal to the terminal velocity. Furthermore, The Reynolds number for a single particle (Re_p), the drag coefficient (C_D) and the force per projected area on a spherical particle. ($R_{particle}$) is defined below [29]:

$$Re_p = xU \frac{\rho_f}{\mu} \quad (5)$$

Where x and μ are the particle diameter and the fluid viscosity, respectively.

$$C_D = \frac{R_{particle}}{(0.5\rho_f U^2)} \quad (6)$$

$$R_{particle} = \frac{F_D}{(\frac{\pi x^2}{4})} \quad (7)$$

Moreover, Figure 20 shows the drag coefficient for motion of a sphere in a fluid. Note that the graph can be divided into three sections; stokes' law, intermediate, and Newton's law, which is based on the relative velocity of the particle.

Table 3 summarizes the drag coefficient equation for different Reynold numbers for a single particle [29].

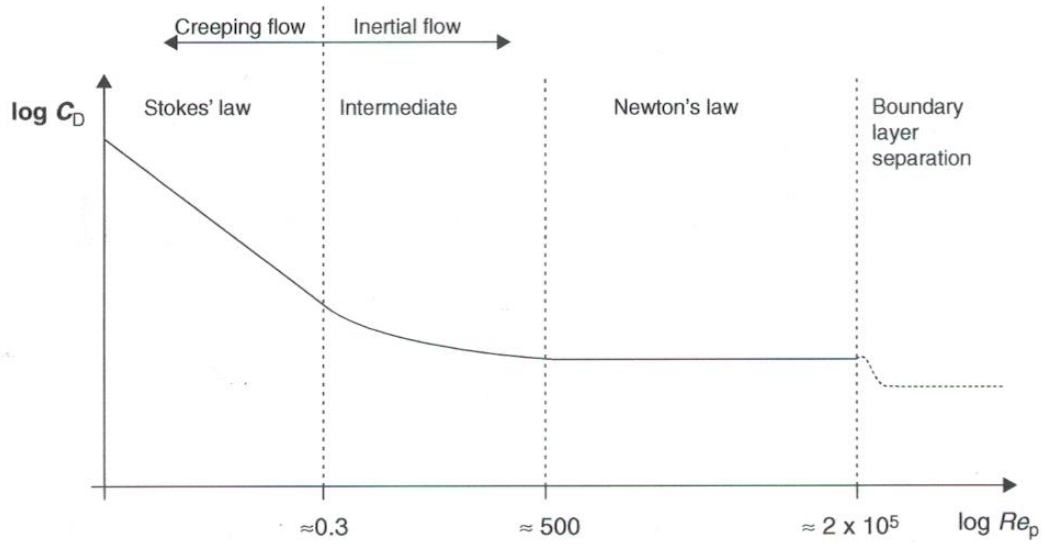


Figure 20: Drag curve for motion of a sphere in a fluid [29].

Table 3: Single particle drag coefficient correlations based on its Reynolds number [29].

Region	Re_p Range	C_D
Stokes' law	$Re_p < 0.3$	$C_D = \frac{24}{Re_p}$
Intermediate	$0.3 < Re_p < 500$	$C_D = \frac{24}{Re_p} (1 + 0.15 Re_p^{0.687})$
Newton's Law	$500 < Re_p < 2 \times 10^5$	$C_D \sim 0.44$

Particles motion under gravity can be very complicated to model and predict especially when there are baffles or any other components in the heat exchanger that mix the particles. This is due to the interaction of particles with the heat exchanger walls, with other particles, and with the air. Furthermore, particles shape and size might vary over time

due to attrition. Therefore, this makes predicting the particle flow very complex. However, a lot of research has been done to predict the particles terminal velocity accurately. Particles falling from rest under gravity can be simplified using a free body diagram showing all forces acting on a single particle, as shown in Figure 21 [29].

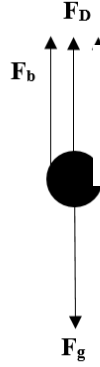


Figure 21: Free body diagram of the particle while falling due to gravity in the heat exchanger.

$$\text{Gravity} - \text{Buoyancy} - \text{Drag} = \text{Acceleration Force} \quad (8)$$

$$\frac{\pi x^3}{6} \rho_p g - \frac{\pi x^3}{6} \rho_f g - R_{particle} \frac{\pi x^2}{4} = 0 \quad (9)$$

By substituting the value of R' from the previous equation 5 into equation 9,

$$\frac{\pi x^3}{6} (\rho_p - \rho_f) g - C_D (0.5 \rho_f U^2) \frac{\pi x^2}{4} = 0 \quad (10)$$

Solving for the drag coefficient (C_D),

$$C_D = \frac{4gx}{3U^2} \left(\frac{\rho_p - \rho_f}{\rho_f} \right) \quad (11)$$

Therefore, solving for the terminal velocity (U) in the three regions,

Table 4: Terminal velocity of a single particle based on its Reynolds number [29].

Region	Re_p Range	U_T
Stokes' law	$Re_p < 0.3$	$U_T = \frac{x^2(\rho_p - \rho_f)g}{18\mu}$
Intermediate	$0.3 < Re_p < 500$	No explicit expression
Newton's Law	$500 < Re_p < 2 \times 10^5$	$U_T = 1.74 \left(\frac{x(\rho_p - \rho_f)g}{\rho_f} \right)^{0.5}$

3.2.2 Particle Bed Fluidization

When air passes through a particle bed column there occurs a pressure drop due to the frictional resistance as the air flow between the particles from the bottom of the bed to the top. However, the fluid exerts an upward drag force on the bed (F_D) and the bed weight exerts an opposite force due to gravity (F_g). When these two forces are equal or balanced ($F_D = F_g$), fluidization occurs. When the bed is fluidized, the particles are distanced from one another and mixing occurs as particles move throughout the bed. Consequently, since fluidization begins when the two forces are balanced, the pressure drop (ΔP) is equal to the force balance divided by the cross-sectional area of the bed (A_{cs}).

$$\Delta P = \frac{F_g - F_D}{A_{cs}} \quad (12)$$

Since a bed of particles will always have some voids between the particles themselves, we need to account for the void fraction in the bed (ϵ). Furthermore, the

gravitational force and the upward drag force can be calculated using the respective densities of each material and the volume. Therefore, the pressure drop will be equal to:

$$\Delta P = \frac{HA(1-\varepsilon)(\rho_p - \rho_f)g}{A} \quad (13)$$

$$\Delta P = H(1 - \varepsilon)(\rho_p - \rho_f)g \quad (14)$$

Where H is the height of the bed, g is the gravitational acceleration, and ρ_p and ρ_f are the densities of the particle and fluid, respectively. This equation is used in the fluidization region of the bed, and the start of fluidization can be interpreted by the minimal fluidization velocity. The minimal fluidization velocity (U_{mf}), which is discussed further in chapter 4, is the velocity at which fluidization begins in the bed, transforming the fixed bed into a fluidized bed [29].

3.2.3 *Classification of Powders*

In 1973, Geldart was the first person to classify fluidization into several categories, he studied characteristics of particles in the air and their fluidization mechanisms. He suggested four main categories, based on particle properties; Cohesive (C), Aeratable (A), Bubble readily (B), and Inertial (D) particles. C particles are particles that are small in size and have strong inter particle forces and exhibit poor fluidization. A particles are particles that have weaker inter particle forces and larger in size than C particles, these particles also fluidize faster. B particles are particles that mix well in fluidization, have weak inter particle forces, and are larger than A particles, they are generally sand-like particles. D particles are particles that are dominated by inertial forces and have minimal inter particle forces, they can be easily fluidized but have do not mix well due to their larger sizes. These

classifications were later extended by Geldart to include the characteristics of particles in several types of gases and two-phase systems [30]. Table 5 shows some examples of the various classification as well as summarizes several properties for each group.

Table 5: Geldart's particle classification [29].

	C	A	B	D
Characteristic	Cohesive and difficult to fluidize	Ideal for fluidization and has a good range of non-bubbling fluidization	Starts bubbling at the minimal fluidization velocity	Coarse solids and difficult to mix
Example	Flour and cement	Cracking catalyst	Sand and ID50	Gravel and coffee beans
Bed Expansion	Low	High	Moderate	Low
De-aeration Rate	Fast	Slow	Fast	Fast
Bubble Properties	No bubbles only channels	Bubbles split and merge together. Has a maximum size.	No limit to bubble size.	No limit to bubble size.
Solids Mixing	Very low	High	Moderate	Low
Gas Mixing	Very low	High	Moderate	Low
Spouting	No	No	Only in shallow beds.	Yes, even in deep beds.

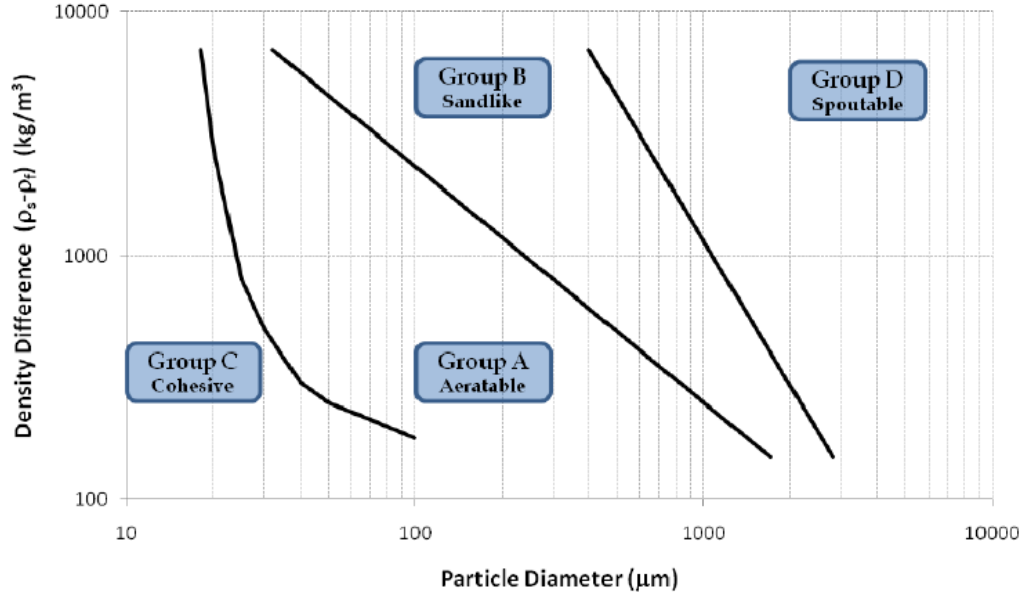


Figure 22: Geldart's particle classification [31].

Figure 22, shows the various fluidization regimes that were classified by Geldart, based on the Archimedes number. Archimedes number (Ar), is a dimensionless number that helps determine the motion of fluids and particles based on the density differences. It is defined as the ratio of gravity and buoyancy forces to the viscous forces of the fluid.

$$Ar = \frac{8g\rho_f(\rho_p - \rho_f)r^3}{\mu_s^2} \quad (15)$$

The equation is the standard equation for the Archimedes number for a fluidized bed. However, there two other equations were defined by Grace as boundary equations to the original equation. The first equation, shown below, is when the inter particle forces do not dominate but are strong (Bubbles readily (B) to Aeratable (A) boundary), the Archimedes number can be defined as follows:

$$Ar = \frac{8g\rho_f(\rho_p - \rho_f)r^3}{\mu_s^2} = 10^6 \left(\frac{\rho_s - \rho_f}{\rho_s} \right)^{-1.275} \quad (16)$$

The second equation, shown below, is when the viscous and inertial forces dominate while the inter-particle forces are weak (Inertial (D) to Bubbles readily (B) boundary) [30].

$$Ar = \frac{8g\rho_f(\rho_p - \rho_p)r^3}{\mu_s^2} = 1.45 \times 10^5 \quad (17)$$

Furthermore, by increasing the volume flow rate of the gas entering the fluidized bed, the velocity of the gas will increase, since the cross-sectional area remains constant. Figure 23, shows the various stages that the bed can experience as increasing the gas velocity.

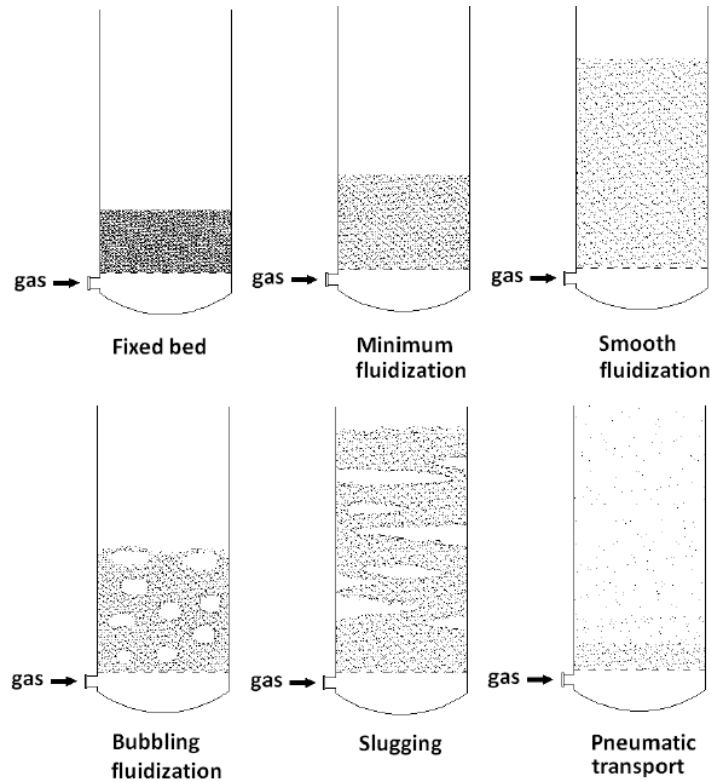


Figure 23: Schematics of various fluidization regimes [31].

3.2.4 Particle Properties

Particle density (ρ_p) can be calculated by dividing the mass of a particle by its hydrodynamic volume. The hydrodynamic volume is the volume of the particle when it interacts with a fluid, this volume can be measured for both porous and non-porous particles, as seen in Figure 24.

$$\text{Particle density} = \frac{\text{mass of particle}}{\text{hydrodynamic volume of particle}} \quad (18)$$

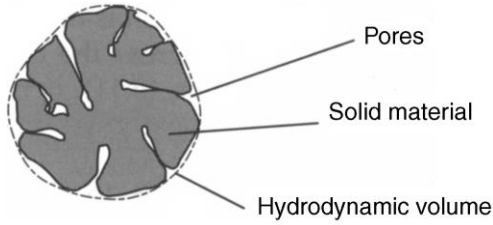


Figure 24: Schematic showing the hydrodynamic volume of a particle [29].

For non-porous particles, the particle density is redefined as ‘absolute density, as this is the density the true density of the material the particle is made of.

$$\text{Absolute density} = \frac{\text{mass of particle}}{\text{volume of solid material making up the particle}} \quad (19)$$

$$\rho_p = \frac{M_p}{V_{SM}} \quad (20)$$

For porous particles, the particle density is not easy to measure so in fluidized beds bed density (ρ_B) is used instead.

$$\text{Bed density} = \frac{\text{mass of particles in bed}}{\text{volume occupied by particles and voids between them}} \quad (21)$$

Similarly, bulk density is used when referring to powders.

$$\text{Bulk density} = \frac{\text{mass of particles}}{\text{volume occupied by particles and voids between them}} \quad (22)$$

Finally, bed void fraction (ε) can be then calculated using the bed density (ρ_B) and particle density (ρ_P).

$$\rho_B = (1 - \varepsilon)\rho_P \quad (23)$$

Furthermore, knowing the particle size is of great importance when designing a direct contact heat exchanger using particles. This is to understand the characteristics of the particle when interacting with the fluid as well as maintaining the heat exchanger. One method that is commonly used in industry to measure particle sizes is sieving. Sieving can also help identify the range of particle sizes after several runs of the experiment. This is also very important to minimize entrainment which will be later discussed. To calculate the mean diameter of a spherical particle using sieving the below equation is used

$$x_p = \frac{1}{\sum m_i/x_i} \quad (24)$$

Where x_p is the average diameter size of particles measures and m_i is the mass of each batch of particles collected for each sieve size of x_i [29].

3.3 Summary

Therefore, it can be concluded that there has been extensive research on fluidized bed reactors and heat exchangers. Yet, there is still a lot of research that needs to be done on moving bed heat exchangers especially when using smaller particulates at higher temperature and pressure. Moreover, the particulate flow has been researched and studied thoroughly, but there are still some areas that still need further investigation, these include particulate forces at different pressures and temperature. For example, I found that bridging occurs at specific pressures when the open area of the orifice was changed. This research will be discussed further in later chapters and should be investigated further.

CHAPTER 4. MINIMAL FLUIDIZATION VELOCITY

4.1 Introduction

This chapter examines an experiment for a simplified model of the system that will be discussed in chapter 6, to be consistent with literature. Furthermore, the design of this experiment will help identify future designs for heat exchangers with inlet standpipes. This investigation will verify that the minimal fluidization velocity equation can accurately calculate the pressure drop across a bed of particles. The equation is typically used in fluidized bed reactors to estimate the vertical pressure differences. This will help us understand the relationship between pressure drop, bed height and fluidization in a moving bed. In understanding this, I can control the bed height to limit fluidization and the blow out of particulates. If the bed height becomes too low, fluidization would occur and the flow would no longer be consistent. This can also lead to a higher risk of particulate blow out or carry over.

The minimal fluidization velocity equation is derived from simple mechanics that the weight of the bed (including the fluid and the solids) is equal to the difference in pressure at the top and bottom of the bed. The equation is as follows:

$$\Delta P = [(1 - \varepsilon)\rho_f + \varepsilon(\rho_s)]gH \quad (25)$$

Where ΔP is the pressure drop calculated across the bed and ε is the volume fraction of solid particles. ρ_f and ρ_s are the densities of the fluid and the solid in the bed. Finally, g is gravitational acceleration, 9.81 m/s^2 , and H is the solid particulate bed height [30].

4.2 Experimental Setup

4.2.1 Design

This experiment was built to visualize the particulate flow and test the minimal fluidization velocity equation as well as measure the different mass flow rates using various perforated plates. The experiment was setup so that there is enough storage for particulates to run the experiment for an adequate amount of time. As seen in Figure 25, the setup was built to have a storage area, valve, particle visualization area, air inlet, as well as a cap to extract and reuse the particulates after running. The storage area has a volume of 2471.1 cm³, it is a cylindrical pipe with a diameter of 5.08 cm with a height of 121.9 cm.

4.2.2 Measurements and Methods

To be able to measure the pressure drop as accurately as possible, 10 iterations were repeated at different heights starting at 14.7 cm to 104.7 cm. To start, the test the storage area was filled with solid particles until a specific height and the storage area was tapped to remove most of the air gaps in the particle bulk. The inlet air was then opened, and the pressure was increased to the theoretical value. Subsequently, the valve was opened, and the pressure was modified until small bubbling occurred at the top of the bed, at this point the pressure was measured. However, reading the pressure values manually at low bed heights is very challenging because of small fluctuations in the bed heights. Consequently, at low bed heights, the height measurement might not be accurate.

A pressure gauge was placed at the air inlet, shown in Figure 26, to measure the pressure. Tick marks were placed in intervals along the particulate column to mark the

exact bed heights required, as shown in Figure 27. Particle density, air density, and volume fraction were taken from the literature and from the particle properties. Before the experiment was conducted, a theoretical calculation was done using some given values from the literature and plugging them in equation 25. Table 6, shows the particulate material values that was taken from the literature.

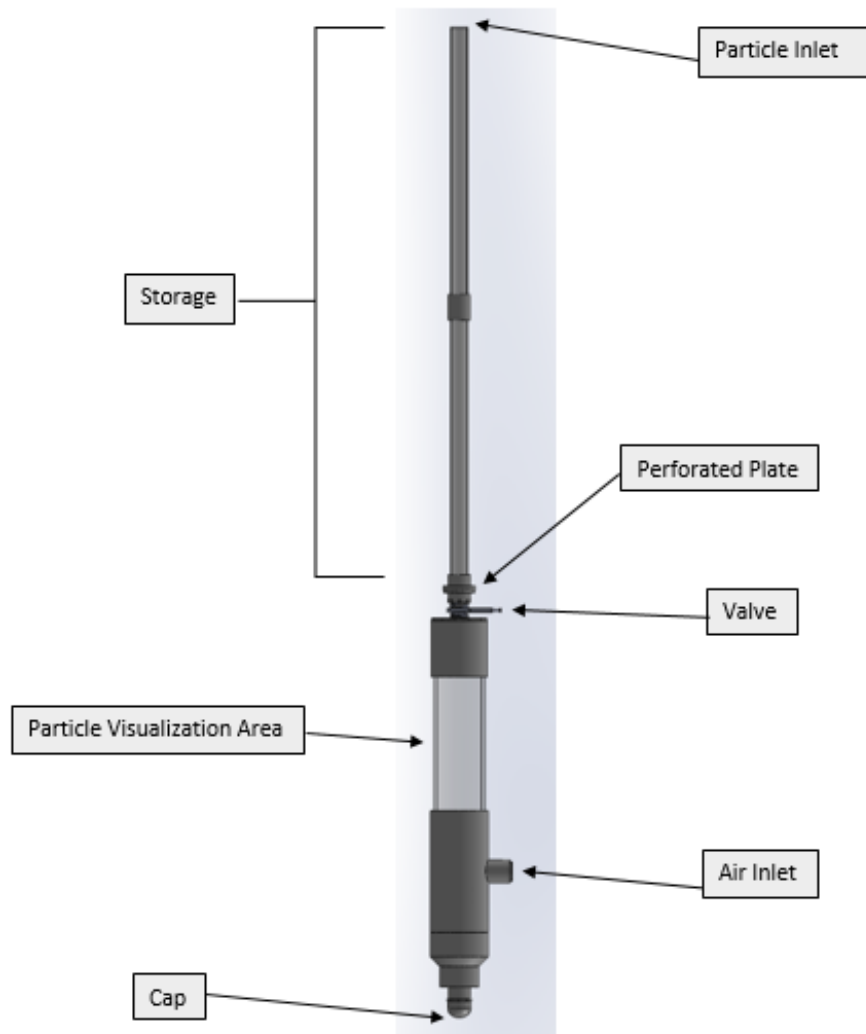


Figure 25: Experimental setup to visualize the particulate flow and test the minimal fluidization velocity equation.



Figure 26: Pressure gauge used to measure the air pressure at the inlet.

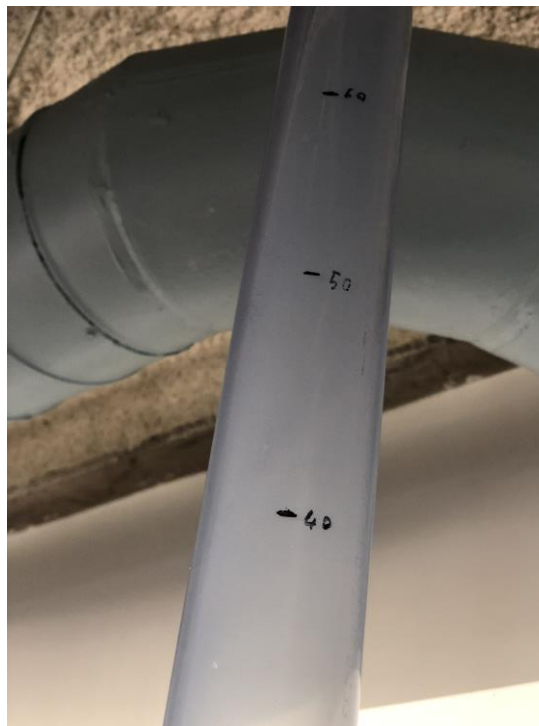


Figure 27: Particle column marked at specific intervals to make it easier to read the height of the bed.

Table 6: CARBO Accucast ID50 particle properties [32].

Property	Value
Mass-median particle diameter	280 microns
Particle density	3300 kg/m ³
Loose bulk density at 1100°C	1810 kg/m ³
Packed bed bulk density at 1100°C	2000 kg/m ³
Bulk porosity / Void fraction	0.39 for packed & 0.45 for loose
Packed bed bulk thermal conductivity at 1100°C	0.7 W/m-K
Specific heat	$365T^{0.18}$ for $50^{\circ}\text{C} \leq T \leq 1100^{\circ}\text{C}$ J/kg-k
Sphericity	0.9
Composition	75% Al ₂ O ₃ , 11% SiO ₂ , 9% Fe ₂ O ₃ , 3% TiO ₂

4.3 Results and Discussion

In conclusion the minimal fluidization velocity equation accurately measures the pressure drop, as the percentage error was less than 5% for all readings except for two outlier points. These two points are the first two readings at a low bed height, where it was very challenging to get accurate measurement due to the sensitivity of the bed with small pressure changes. Figure 28, shows the experimental and theoretical pressure drop values for this experiment. The blue line indicates the theoretical values that were calculated in Microsoft Excel using equation 25. The orange circles indicate the ten readings at different bed heights with the recorded pressure drops. Finally, the dotted line shows the linear best fit line for the data, as can be seen in the figure there is a small difference between the

theoretical and experimental slopes. The table below shows the experimental data collected with the device uncertainty given in the table header.

Table 7: Raw data for the minimal fluidization velocity experiment.

Height (cm) ± 0.05 cm	Pressure Drop (kPa) ± 0.3 kPa
14.7	1.8
24.7	3.8
34.7	6.2
44.7	7.2
54.7	8.9
64.7	11.1
74.7	12.4
84.7	14.8
94.7	17.6
104.7	19.3

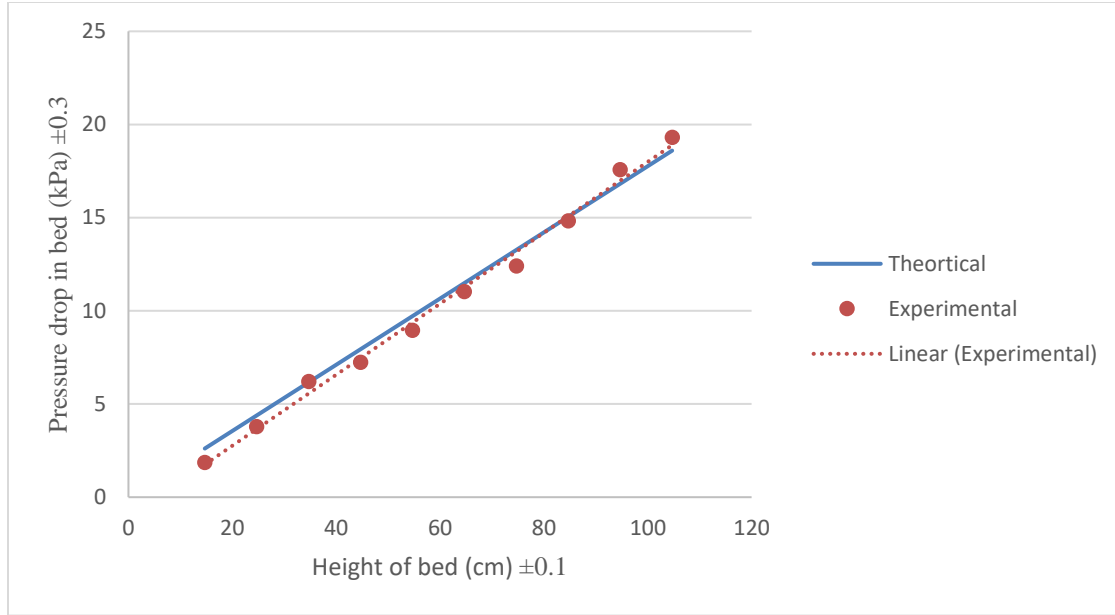


Figure 28: Experimental and theoretical pressure drops values for moving bed of particulates in a vertical column.

There is a bias or device uncertainty for each of the devices used to measure the height as well as the pressure. The device used to measure the height is a tape measure with the smallest increment of 0.1 cm. Thus, the uncertainty for the device is ± 0.05 cm, this was also verified by a calibrated caliper. To measure the height the measurements were made before the experiment on the empty particulate column. So that the column itself has horizontal lines indicating the height of the particulates. This allowed me to easily measure the height of the column and then by changing the pressure until initial bubbling is observed in the bed. The wire mesh placed underneath the particulate column insured that particles do not fall, and that the particulate column behaves as a fluidized bed only for this experiment. Furthermore, the device uncertainty for the pressure gauge was 0.05 psi based on the manufacturer's website, which can be converted to about 0.3 kPa [33]. The pressure was measured at the start of each experimental run.

CHAPTER 5. OVERVIEW OF INTERNAL DESIGNS OF HEAT EXCHANGERS

5.1 Introduction

In this chapter, there are presented several internal designs of heat exchangers that help mix the air with the particles. In this application, almost certainly the air will be pumped from the bottom to the top of the heat exchanger, while the particulates will be moving downwards by the force of gravity. One of the most important aspects of the design is to ensure that the air and particulates mix well. The goal of this chapter is to find an applicable design that will be suitable for the solar tower application. Further, to be able to change the internal design of the heat exchanger easily and in a cost-effective method, the experiment was designed in a modular design. This enabled me to easily exchange the internal parts of the heat exchanger while ensuring a good pressure seal throughout the experiment. In Figure 29, the transparent PVC pipe acts as the shell for the heat exchanger. The use of a clear PVC is to enable a good view of the interaction of air with the particulates in various designs. In Figure 30 shows an example of one of the internal parts of the heat exchanger, which can be replaced when experimenting with other designs. Moreover, since in the experimental model the heat exchanger is cylindrical, all the designs are done to fit that specific design. However, when sizing up the heat exchanger the design might change to rectangular and thus changing the internal designs, but the concepts will stay the same.

In literature, it was proven that some of these designs work for specific applications. For example, the disc and donut design was concluded to be used in a direct contact heat

exchanger between liquid and gas [34]. This design was chosen because it provides a large amount of surface area or ‘curtain’ per unit of volume of the heat exchanger which thus increases the effectiveness of the heat exchanger [35]. Furthermore, other research has also shown that the disc and donut design have some advantages over other designs. These advantages include radial and counter flow patterns, low pressure drops, and freedom of inlet and outlet air nozzles [36]. Other designs such as the chevrons and the zigzag designs also have shown advantages in liquid and vapor counter flow heat exchangers at low velocities. These designs as well as the disc and donut design have also proven to have a fouling resistant attribute [37]. Finally, I have chosen to peruse these four designs (Conical, disc and donut, zigzag, and chevrons), as they can be easily manufactured and assembled at a laboratory scale. Furthermore, from literature it was seen that these designs might be good candidates for this application.

Moreover, the tubular design has also been explored in literature more specifically the circular tubular design. The design was tested in two research papers targeting particulate flow in solar tower applications. One paper shows that this design slows down particulates and creates a “pachinko” effect [38]. However, the second paper shows that this design can have an impact on the particulates since the particulates are constantly hitting the tubes which can cause abrasion and wear to the particulates [39].



Figure 29: Transparent PVC pipe that was used in the experiment.



Figure 30: Internal parts for the conical design of the heat exchanger.

5.2 Material Geometry

5.2.1 Conical Design

In the conical design, the flow of particles is forced to disperse by using an upward conical shape, as shown in Figure 31. The flow is dispersed from the normal central flow with a diameter of 2 in. (50.8 mm) to a 6 in. (152.4 mm). This dispersion is then followed by an inverted cone with a middle hole to allow the flow through. The diameter of this hole is 1.5 in. (38.1 mm), to get the particles close together and enable efficient mixing with the air. The air, on the other hand, is flowing from the bottom to the top. The air follows the conical pattern and takes longer to pass through the heat exchanger in this design. However, one major advantage of this design is that the air mixes thoroughly with the particles at the 1.5 in. (38.1 mm) hole.

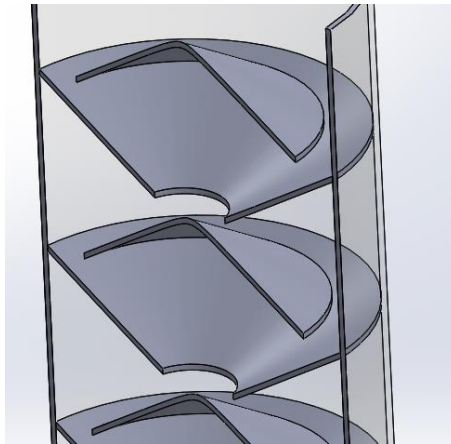


Figure 31: Conical design made on SolidWorks.

To be able to get this design in the cylindrical PVC tube, three holes were made in the design to pass three threaded rods through and then small nuts were used to secure the design in place. A total of six nuts were used for each cone and twelve for both the upward

and downward facing cones. Finally, each set of cones (upward and downward facing) were 3 in in length and no spacing was placed between each set.

5.2.2 Disc & Donut Design

In the disc and donut design as shown in Figure 32, the flow of particles is first dispersed from the top of the heat exchanger using a cone. The dispersed particles then enter the heat exchanger and hit the disc and donut, the particles momentum will minimize any particles from staying on top of the surface. However, to eliminate this problem completely, the use of a perforated plate is preferred. The donut has an outer diameter of 6 in and an inner diameter of 3 in. (76.2 mm), the disc has a diameter of 4.25 in. (107.95 mm). The reason why the disc is larger than the inner diameter of the donut is to increase the mixing efficiency between the particulates and the air.

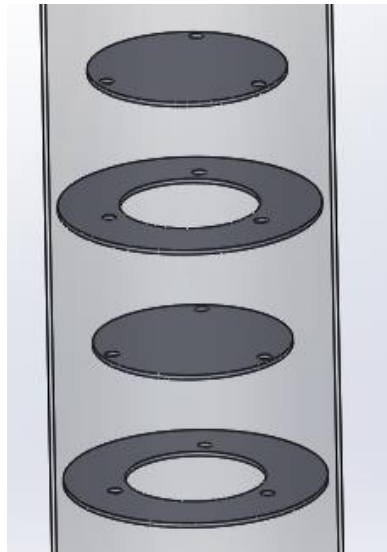


Figure 32: Disc and donut design made on SolidWorks.

Three holes were made in the design to be able to get this design in the cylindrical PVC tube, as can be seen in Figure 30. Three threaded rods passed through the discs and

donuts, and nuts were used to secure the design in place. A total of six nuts were used for each disc and each donut. Finally, the distance between the disc and the donut was 3 in. (76.2 mm) in length.

5.2.3 Zigzag Design

Figure 33 shows the zigzag design, the particles falling from the top follow the direction of the plates placed and the air coming from the bottom stays in contact with the articles along the surface. The air also mixes with the particles at the ends of each section. This design can be easily integrated to a rectangular design as well and is much cheaper to manufacture than other designs.

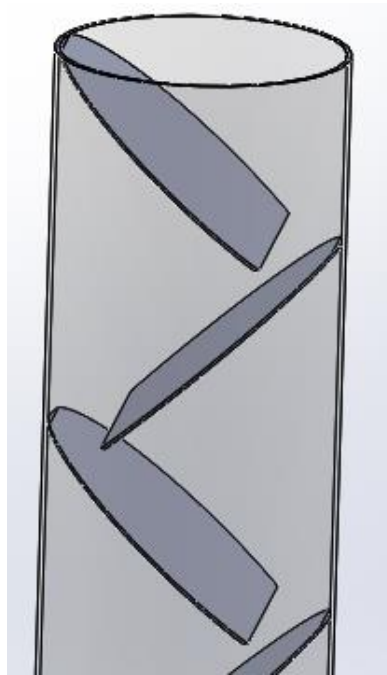


Figure 33: Zigzag design made on SolidWorks.

To be able to get this design in the cylindrical PVC tube, three holes were made on the same line with the angle direction of the surface. Three threaded rods were then passed

through the holes and then nuts were used to secure the design in place. The nuts helped make sure the placement of the plates is at the correct distance. The plates were angled to 45° each direction and there was no spacing between each plate.

5.2.4 *Chevrans Design*

In the chevron design, shown in Figure 34 and Figure 35, the particles falling from the top get distributed using a cone at the top of the heat exchanger, this expands the falling diameter of the particles from 2 in. (50.8 mm) to 5 in. (127 mm). The particles are then disturbed even further through the chevrons. The chevrons placement is in a 2-1-2 configuration. This a simple configuration due to the size of the experiment. The chevrons are relatively easier to manufacture and assemble in a rectangular heat exchanger, thus making this design sizable. Furthermore, each chevron is bent at a 90° angle and is cut in the size of the 6 in. (152.4 mm) outer tube of the heat exchanger.

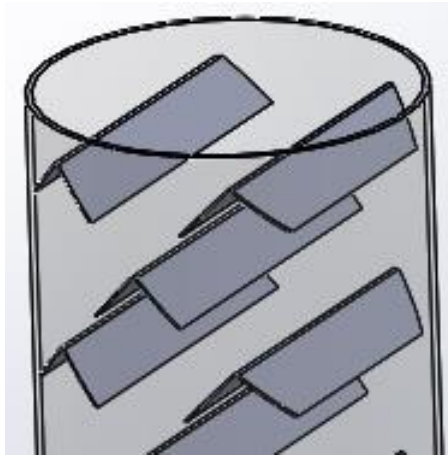


Figure 34: Chevron design made on SolidWorks.



Figure 35: Side view of the chevron design for the heat exchanger.

Moreover, the air being pumped from the bottom can have several stagnant areas if the chevrons are made from a solid material. Thus, this design would be more appropriate if used with a perforated plate or a wire mesh. Three holes were made in each chevron, to be able to get this design in the cylindrical PVC tube in a modular fashion. Three threaded rods passed through the chevron, and nuts were used to secure the chevron in place; Moreover, the distance between each stage of chevrons is 1 in. (25.4 mm).

5.2.5 Tubular Designs

There are also several tubular designs that can also be used to distribute and mix the flow. These tubular designs are hollow, meaning that the tubes have no fluid flowing inside them and are not out of a solid material. Figure 36, shows a grid of square tubes, the advantage of this of grid alignment is that it can simply be shifted or changed to acquire specific flows.

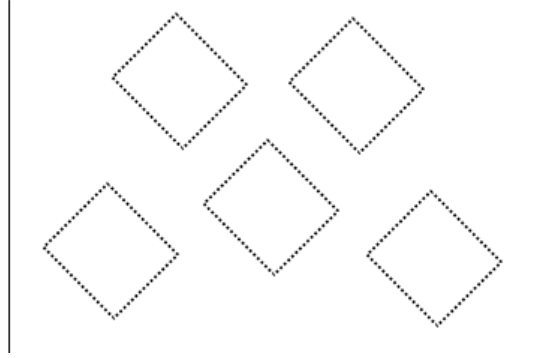


Figure 36: Side view of the square tubes grid design for the heat exchanger.

Similar to the rectangular tubes, Figure 37 shows a circular tube grid. In this design the particles and the air both have a smoother flow around each tube.

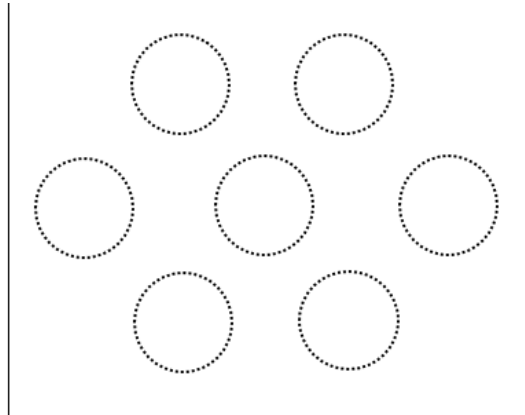


Figure 37: Side view of the circular tubes grid design for the heat exchanger.

Finally, the triangular tube grid, shown in Figure 38, is very similar to the rectangular grid in distributing the particles but different from the perspective of the air flow. The air will have many stagnation points in this design and will take longer to pass through the heat exchanger.

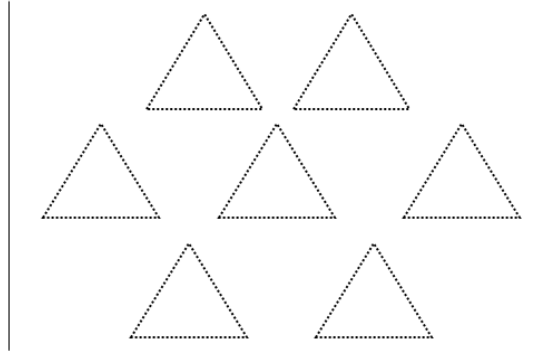


Figure 38: Side view of the triangular tubes grid design for the heat exchanger.

5.2.6 *Corrugated Sheets Design*

Another design concept is using corrugated sheets, the benefit of such design is mainly cost. It has the same principles as the chevron design but is much cheaper to manufacture. Furthermore, Figure 39 shows an example of two sets of corrugated sheets, with the same open ratio but not the same hole diameter. The design can be customized in many ways to increase the effectiveness of the heat exchanger. Moreover, in these designs, the trenches in the corrugated sheets will be cut to minimize any particles from sitting in these areas.

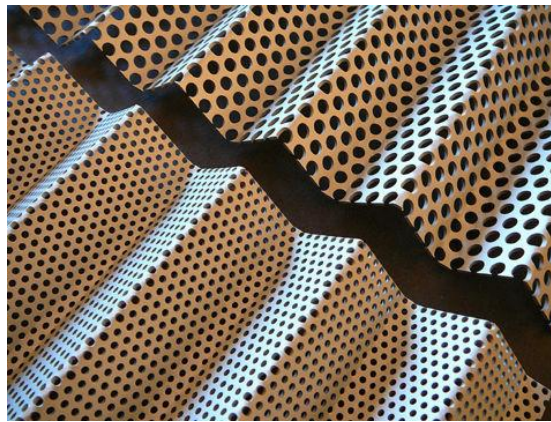


Figure 39: Perforated corrugated sheets that can be used in the heat exchanger.

5.2.7 Helical Design



Figure 40: Schematic of a helical static mixer, which is mostly used in the chemical industry [40].

This helical design, shown in Figure 40, is categorized as a medium performance static mixer, it consists of right and left helical twists, which results in a relatively low pressure drop. This design can be much harder to manufacture but can be very effective especially in smaller sized heat exchangers. This is due to the fact that the particle flow is divided into two portions at every helical twist and this forces the particle to vigorously mix with the air at every stage [40].

5.2.8 Cross Zig Zag Design



Figure 41: First type of a cross zigzag static mixer design that is used in smaller heat exchangers [40].



Figure 42: Second type of a cross zigzag static mixer design that is used in larger heat exchangers [40].

The cross zigzag design, shown in Figure 41 and Figure 42, is categorized as a medium performance static mixer. This kind of mixer will be able to thoroughly mix particulates and air in a smaller space but might be more challenging to maintain. This design would also increase the heat transfer between the particulates and the air and thus could increase the effectiveness of the heat exchanger [40].

5.3 Type of Porous Structure

5.3.1 Perforated Plate

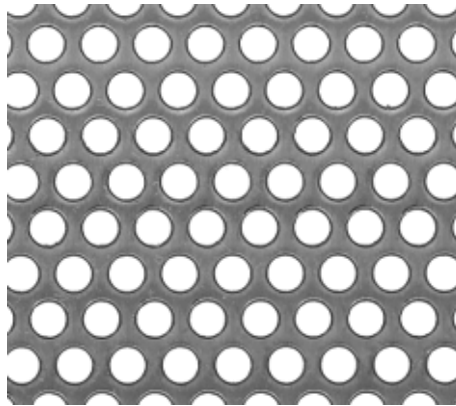


Figure 43: Perforated plate that was used in one of the direct contact heat exchanger design.

This type of porous structure is typically made from steel, the material can come in different thicknesses, hole diameters, and opening percentage. They are sold in sheets and then cut to the required shape and size to conduct the experiment. These types of porous structures are hard to shape since most of them are made from thick steel sheets. Figure 43 shows a sample of the perforated steel material that was used in the experiment.

5.3.2 Wire Mesh

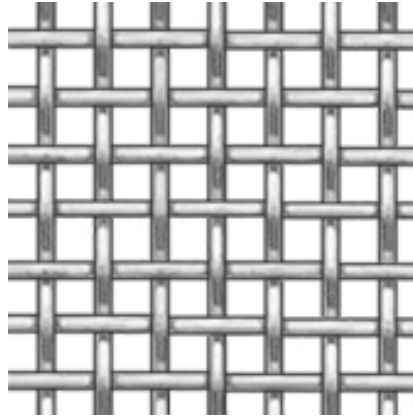


Figure 44: Steel wire mesh that was used in one of the direct contact heat exchanger design.

This type of porous structure is made from steel, the material can come in various wire diameters, opening sizes, and open area percentage. It is sold in sheets and then cut to the required shape and size. These materials are easier to shape as the wire diameter decreases. Figure 44 shows a sample of the steel wire mesh that was used in the experiment.

5.3.3 Foam



Figure 45: Aluminum foam or porous structure.

This type of porous structure is made from aluminum, the material can vary in cell size as well as thickness of the plate. It is sold in flat plates and then cut to the desired shape; Figure 45 shows an aluminum foam that was cut to a 2 in. (50.8 mm) disc.

5.3.4 *Directional Porous Structure*

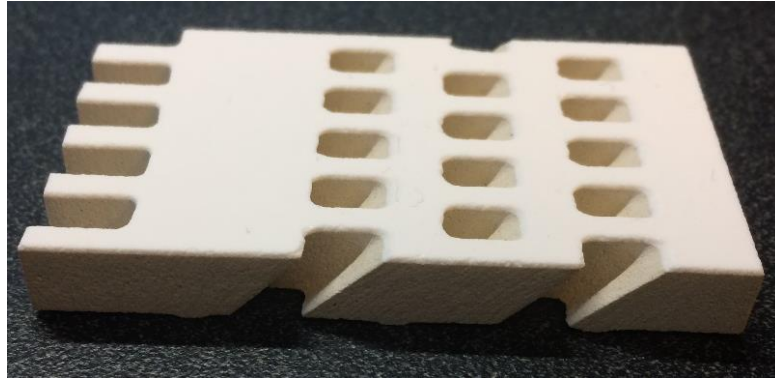


Figure 46: Directional porous structure, the material used here was ceramics.

This type of porous structure could be made from many materials, but in this design, ceramics was used. The sheets are then cut with the waterjet to the desired shape. The water jet also cuts the holes at an angle to create the shape seen in the Figure 46

5.4 **Heat Exchanger Material Requirements**

There are several requirements for the material of the internal parts of the heat exchanger, ranging from physical and mechanical properties to the resistivity to corrosion. The material should have specific physical properties, which include a high heat transfer coefficient with a high thermal conductivity. It should also have a low thermal expansion coefficient and to account for thermal cycling conditions. Furthermore, the mechanical properties for the material, should include that the material has a high tensile strength as well as good creep properties. This includes, good creep ductility for localized strains and

high creep rupture strength for operation at high temperature. Other mechanical properties include high impact strength, fracture toughness, and fatigue. Moreover, the material needs also to be able to resist corrosion and thus should have a low corrosion rate, resistance to corrosion, and tolerance for chemical corrosion [41].

5.5 Orientation of Heat Exchanger

Some heat exchangers are placed at a 90 degree from the ground so that gravity can play a role in the flow of the fluid inside the heat exchanger, as shown in Figure 47. However, some designs have shown that by tilting the heat exchanger it can increase the time it takes for particles to mix with the air and thus increasing the effectiveness of the heat exchanger, as can be seen in Figure 48. Keeping the tilt in mind the internal design of the heat exchanger can be very different to utilize the force of gravity on the particles. The tilt might also be helpful in designing the heat exchanger to minimize particle entrainment.

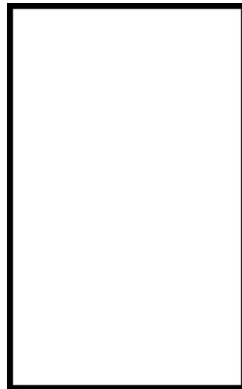


Figure 47: Right angled heat exchanger design (standard orientation).

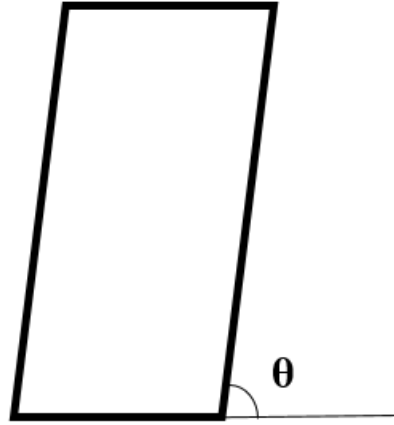


Figure 48: Tilted heat exchanger design.

5.6 Concluding Remarks

The direct contact particle heat exchanger can be developed to efficiently transfer heat from the particulates to the air. The particles are fed from the top and the air is pumped from the bottom of the heat exchanger. There are a lot of advantages for such a system when compared to indirect contact heat exchanger. This includes, a higher thermal contact area between the particles and the air, a better use of the heat exchanger capacity, a greater dynamic range, superior resistance to fouling, and a lower pressure drop. In the direct contact heat exchanger there is no intermediate boundary and thus there are no appreciable temperature gradients between the two materials. The pressure drop is also highly reduced because there are no solid fins or tubes [41].

As can be seen in this chapter, there can be a lot of various designs for the direct contact particle heat exchangers depending on the application. The designer can alter the design of the heat exchanger to fit into the system requirements of the application. Consequently, using a direct contact design would also reduce the price of the heat

exchanger as there would be no tubes or fins in the system, which are made from expensive materials to withstand corrosion and heat. The goal of the design is to slow down the air velocity, to minimize particle entrainment, and to increase the time it takes the particles to exchange heat with the air. Finally, the design chosen was the disc and donut design as this was one of the mostly used in other industries as well as its simplicity in manufacturing the design. It is also an ideal candidate for a cylindrical heat exchanger that was built in the lab.

CHAPTER 6. INVESTIGATION OF PARTICLE INLET

6.1 Introduction

The goal of this chapter is to investigate the particle inlet and study the particle mass flow. This will be done using several types of perforated plates, the mass flow will be studied by varying the percent of open area, the diameter of the open area, and the supply air pressure. This investigation will help formulate a better understanding of the inlet mass flow for particulates entering the heat exchanger. One important aspect about the inlet flow to the heat exchanger is how much particles are needed and how fast are they falling. To answer these questions, we need to know the particle properties and particle flow principles. The particle mass flow rate or rate of discharge is independent of the height of the particle column, meaning that height does not affect the pressure on the outlet in static particle columns. This observed behavior is called a Beverloo flow. Therefore, according to literature the equation to calculate the mass flow rate for this kind of system is given below,

$$\dot{m}_p = (0.58\rho_B)g^{0.5}(d_{out} - kd_p)^{2.5} \quad (26)$$

Where \dot{m}_p is the mass flow rate for the particles (kg/s), ρ_B is the bed density (kg/m³), g is the gravitational constant (9.81 m/s²), and d_{out} is the outlet size (m). k is a constant depending on the particle shape typically 1.5 for spherical particles, and d_p is the particle size (m). This equation is called the Beverloo equation and is widely known in the powder technologies field [42].

6.2 Design and Setup

6.2.1 Instrumentation

There are three main instruments that were used in this experiment. First, the vane anemometer, shown in Figure 49, was used to measure air leakage from the top of the material column. Second, the rotameter to measure the volume flow rate of air as it enters the heat exchanger, shown in Figure 50. Third, two pressure gauges, as shown in Figure 51, were used; one at the supply air outlet to control the overall flow and one right after the rotameter before the supply air enters the heat exchanger. Moreover, a water ruler was constantly used before each experiment to make sure that the apparatus is not tilted. Furthermore, the device uncertainty for the pressure gauge was 0.05 psi based on the manufacturer's specifications, which can be converted to about 0.3 kPa [33]. The pressure was measured at the start of each experimental run. The vane anemometer was not used during the experiment, as the air velocity was too low at the exit to rotate the blades. As for the rotameter, the device accuracy is $\pm 5\%$ of the reference value, according to the device manufacturer's specifications [43].



Figure 49: Vane Anemometer that is used to measure the air outlet in the experiment.



Figure 50: RotaMeter that is used to measure the supply air in the experiment.



Figure 51: Pressure Gauge that is used to measure the pressure inlet in the experiment.

6.2.2 First Iteration

The first iteration of the experiment was used to analyze the minimal fluidization velocity as well as measuring the mass flow and the air velocity. As seen in Figure 52, there is an air connection for the air inlet, a gate valve to control the start of the experiment, and the material column that holds the particulates that will fall through the transparent PVC pipe. Furthermore, a vane anemometer was placed at the top of the material column which is the same as the inlet for the particulates. In this setup, the PVC pipes were glued or cemented together using PVC cement to minimize air leakage in the experiment. However, the disadvantage of this setup is that it is rigid and not flexible for change thus we cannot analyze any other principles or properties. The objective of this first iteration was to measure the velocity of the air at the outlet. Since the air at the outlet was at very low velocities and I was unable to use the rotameter to measure the flow rate. By having one inlet and one outlet, I can measure the air flow rate at the inlet and it will be equal to the air flow rate at the outlet.

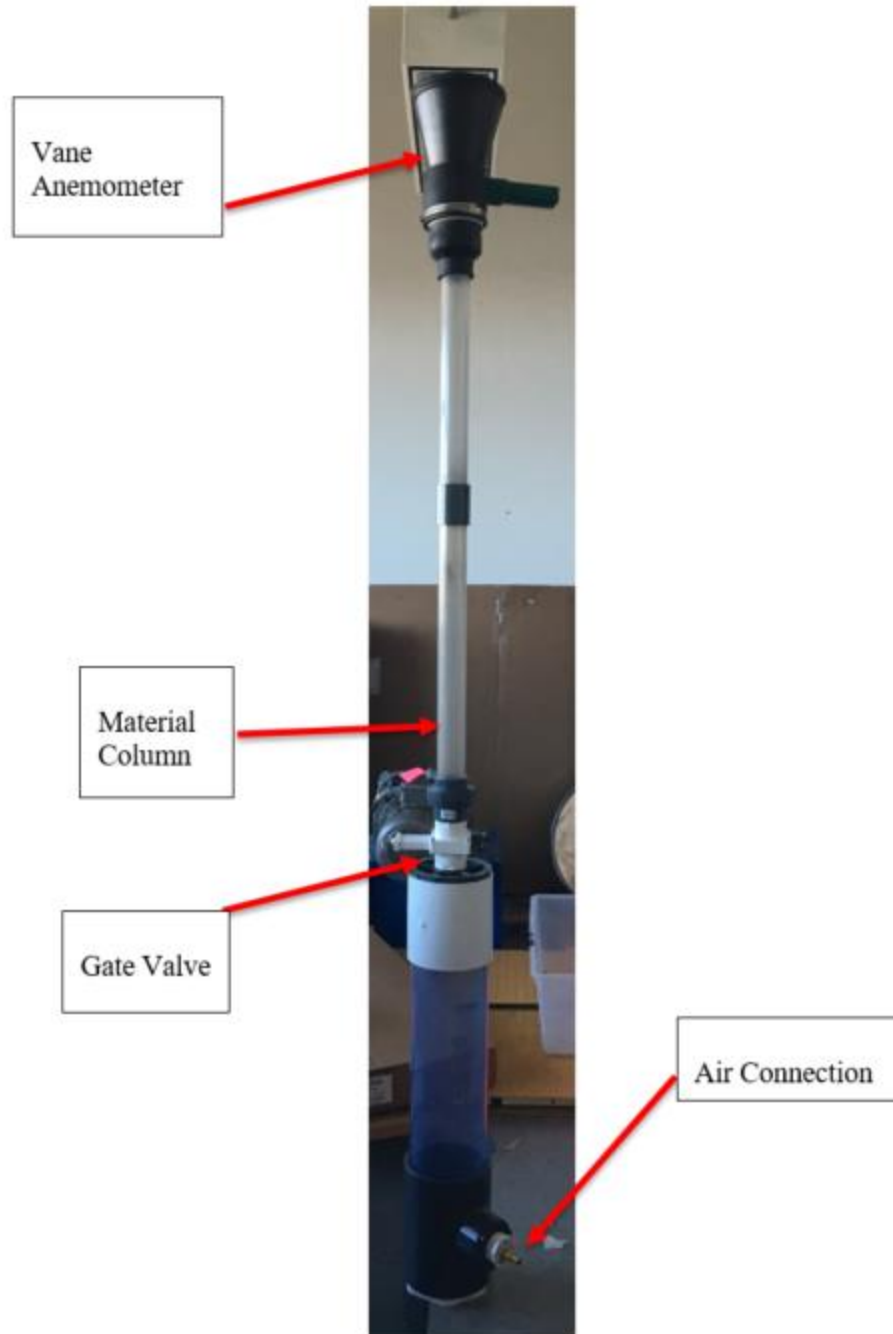


Figure 52: The first iteration of the experiment.

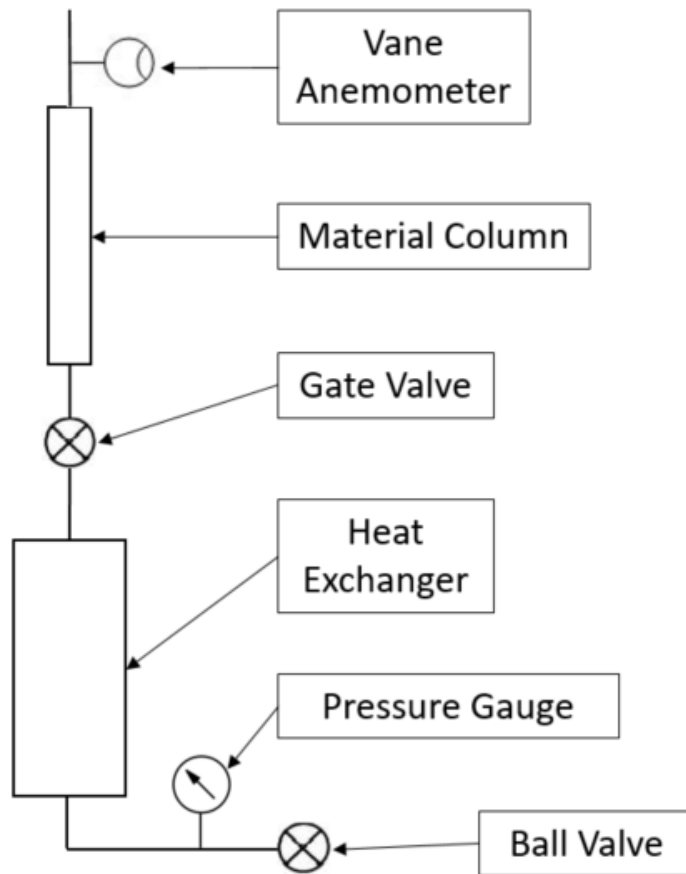


Figure 53: Schematic of the first iteration of the experiment.

6.2.3 *Second Iteration*

In the second iteration of this setup, there were many factors taken into consideration to make the design flexible and easily changeable. This setup was built using a modular design and having flanges to connect pipes together rather than using the PVC cement. Furthermore, rubber gaskets were used to ensure a good seal and minimize air leakage. Each section of this experiment will also be discussed in more details below. The setup looks like Figure 52, but with the replacement part in Figure 61. The wye section shown in Figure 54, was initially used however creates several problems. One of these problems was the size and weight of this part, because it was very heavy to transport to the top of the system. The second problem was that it was 2 feet in height and that created a long free fall drop for the particles which was not the requirements needed for this experiment. Third, another problem was the height, the experiment was very tall, and it was very challenging to refill the particulate column. Therefore, this part was eliminated and replaced with a smaller part in the next iteration.



Figure 54: The 6 in diameter PVC Y-fitting that was used in the second iteration of the apparatus for the air outlet connection.

6.2.4 *Third Iteration*

This was the third iteration of the design and was the final design. Figure 55, shows the full system with the material column taken out of the system to be refilled. This system was designed so that the material column can be taken out refilled with particles manually and then reattached to the top of the system. This enabled easy and fast refilling rather than climbing up the stairs with buckets of particles. This feature also increased the safety of the person conducting the experiment. Furthermore, the system was a modular design with 5 modules, each with a different function. As one moves from the top to bottom in Figure 55, the first module is the material column with the gate valve. Then the 2 in. (50.8 mm) wye module, and then the heat exchanger module. After that, there is the air inlet 6 in. (152.4 mm) PVC tee module, and finally the storage bin with a release valve. Each of these modules will be discussed in further details below. Also, note that the Unistrut structure that was made to support not only the experiment but also the users of the experiment.

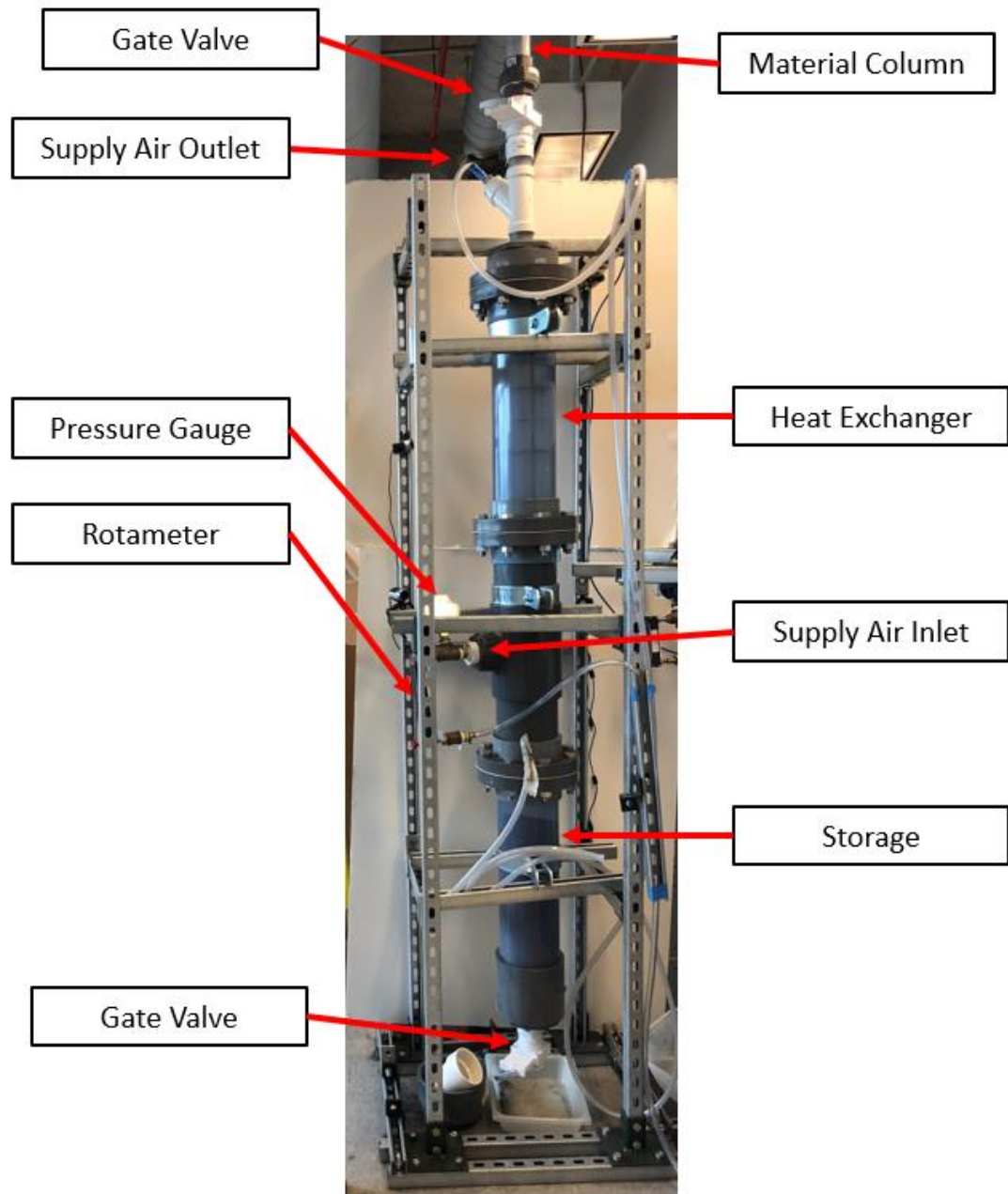


Figure 55: The third iteration of the apparatus.

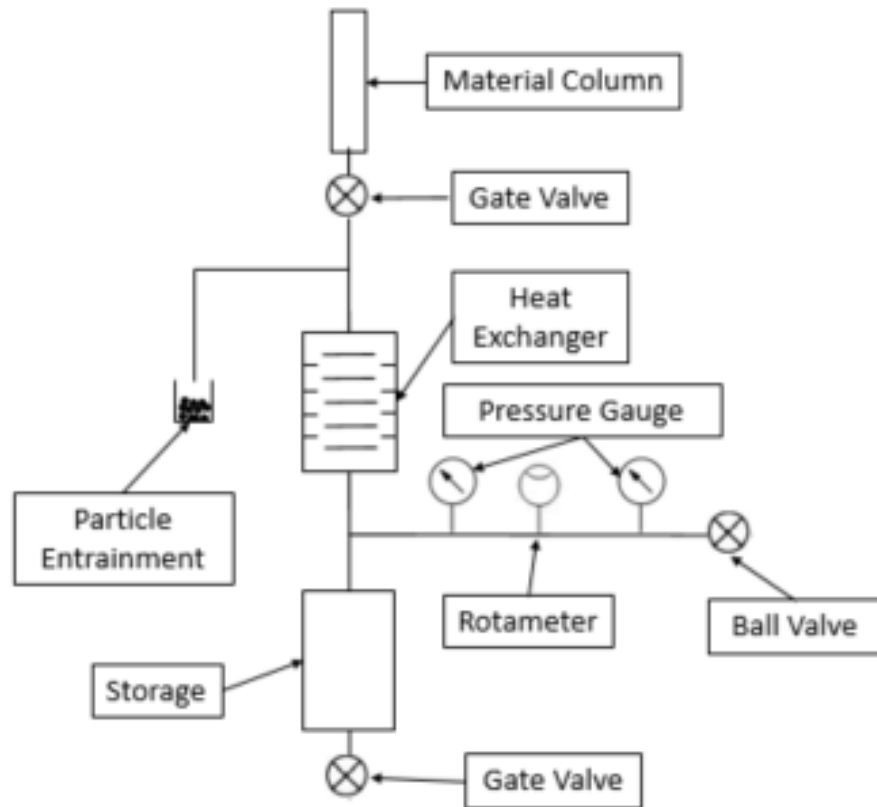


Figure 56: Schematic of the third iteration of the experiment.

This is the top storage bin or material column that is used to store 43.3 in. (1099.82 mm) of particulates in the 2 in. (50.8 mm) diameter column. As shown in Figure 57, at the top of this is a removable funnel to help fill the material on the ground before carrying back to the top of the experimental setup. At the bottom, there is a gate valve which controls the start and end of the experiment as well as helps make the refilling process much less challenging. While refilling the gate valve is closed and particles are poured from the top of the chamber to the required height. After that this whole module is carried to the top of the experiment and reconnected to the rest of the apparatus.

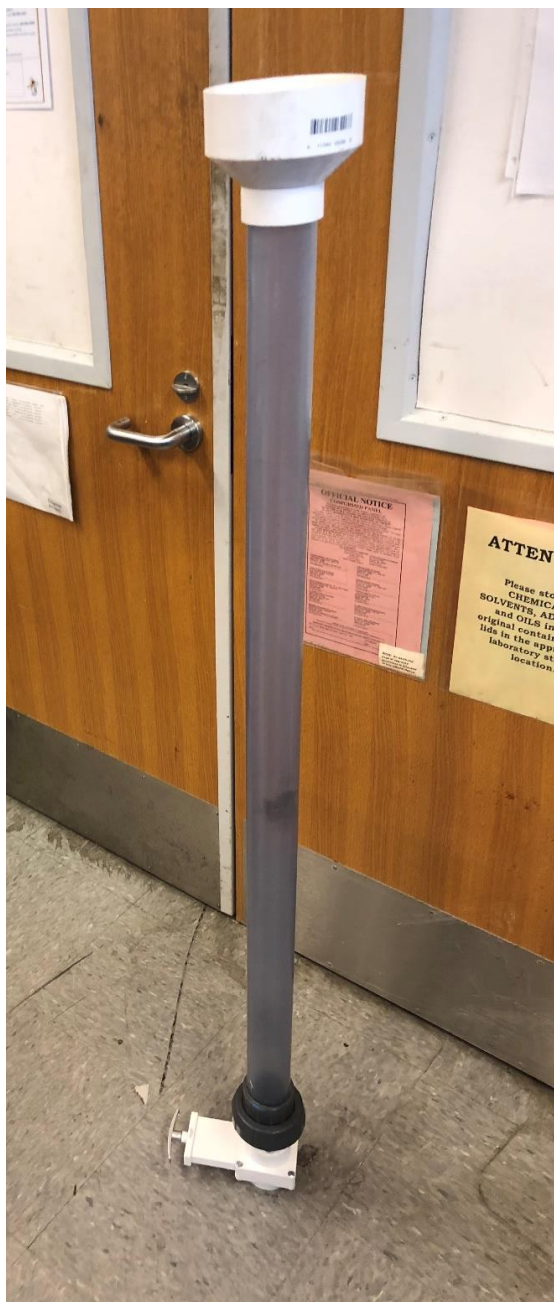


Figure 57: The material column that is used to be attached to the top of the apparatus.

Figure 58, takes a closer look at the gate valve. The valve is constructed out of PVC, but the gate is made of stainless steel and the gate seat, shown in black, is made from santoprene. The operation of the valve is simple, and the gate seat helps keep the particles

from blocking the valve. Moreover, this gate valve is an on and off valve that is designed for water. However, this valve is great for experimental work with particulates and can be used as a shut-off valve as well as a flow control valve (half opened).



Figure 58: Gate valve that is used in the experiment.

The perforated plate holder is placed between the 2 in. (50.8 mm) PVC pipe and the gate valve. This plate holder is of vital importance to this apparatus, as it allows us to change the perforated plate type and shape. As can be seen in Figure 59 and Figure 60, the plate holder looks like a pipe connection but has the advantage of being adaptable to many types of perforated plates. There is also a rubber seal that maintains the pressure in the vessel and limits air leakage.



Figure 59: Perforated disc holder in its assembled position.



Figure 60: Perforated disc holder in its disassembled position.

The second module is the Y pipe fitting, this module is very important as it is where the air outlet is and where the particulates enter, as shown in Figure 61. The particle inlet is from the vertical column and the air outlet comes out in the hose. The hose is used to measure how much particles are entrained when conducting the experiment. This is a vital part of the experiment that would help us identify any entrained particles. Furthermore, a perforated disc was also placed right before the particles enter the heat exchanger to slow down the flow as it has accelerated while falling from the material column.



Figure 61: A 2 in. Y-fitting air connection for the experiment.

This is the heat exchanger module and is the third module of the design. As can be seen in Figure 62, the heat exchanger is made of the clear PVC pipe. Flanges were also cemented to the clear PVC pipe to be able to interchange the part easily. The gasket used between the flanges can also be seen in this figure which is made from rubber. Moreover, a set of cameras were also used to record all the experiments and to show the flow of the particulates. As can be seen in Figure 62, the disc and donut design has been placed in this setup to be tested. The advantage of this design is that it is very simple to interchange the internals of the heat exchanger. Figure 63, shows an example of the internals of the heat exchanger separated from the system. The example, shown in the figure does not have the flanges attached to it yet. In Figure 64, one can also see the use of a diffuser at the top of the heat exchanger as well as a perforated plate. The diffuser is used to separate the flow from a 2 in. (50.8 mm) diameter to a 6 in. (152.4 mm) diameter and the perforated plate

has two main functions. The first is to attach the internals to the top of the heat exchanger and easily remove it from the system when needed. The second is to ensure that the particles are entering the heat exchanger at a regulated speed.



Figure 62: Heat Exchanger module used in the experiment.

Figure 65 shows the lower section after the heat exchanger, and this is the air connection module. It is made of a tee fitting and has the pressure gauge at the inlet of the heat exchanger. Further, a camera is placed to also observe and record the pressure when the experiment is running. Also, in the background of the figure, a pipe clamp is used to hold each section of the apparatus for easy disassembly and assembly.



Figure 63: Heat exchanger module detached from the system.



Figure 64: Particle distributor used on top of the heat exchanger module.



Figure 65: Pressure gauge attached to the inlet and with a camera recorder.

Below the air connection section comes the last module which is the storage bin, shown in Figure 66. It is made of clear PVC and it is transparent to enable us to check how much of it was filled. At the bottom of the storage bin there is a release valve so that the particles can be discharged when the bin is filled. A small bucket is then used to remove particles from the experiment back to their original containers where they can be reused for future experiments.



Figure 66: Storage bin with a release valve to reuse the particulates.

Copper wire was incorporated into the experiment when static charges started to increase. When the particles hit any plastic surface, they create a charge but due to the increased use and numerous iterations of experiments the particles needed to be discharged. Figure 67, shows how much the particles were charged. Thus, the experiment required to have a copper wiring to ground the static charges generated by the particle flow. The copper wire, shown in Figure 68, was attached in different parts around the experiment to discharge the static charges to a ground source.



Figure 67: Particulates statically charged after several runs through the apparatus.



Figure 68: Copper wire used to discharge the particulates and minimize any static charges.

6.3 Methodology

This experiment was conducted using four types of perforated plates, these include two perforated plates from each opening area percentage. Each perforated plate disc was tested from 0 to 2 bar pressures with a 0.5 bar step size, so in total 5 experiments were done. Furthermore, each pressure was then tested several times using a total particle height of 1100 mm in the particle column. A stopwatch was used to measure the time it takes the particles to pass a 10-cm tick mark on the particle column. By knowing the volume of the space and the time it takes for particles to pass through that space, one can calculate the volume flow rate. Moreover, by doing this for each 100-mm column then we can take an average of all the measurements and calculate the average volume flow rate. Then by using the density of the particle, we can calculate the mass flow rate. Further, by knowing the cross-sectional area the particle column we can estimate the average velocity for each particle. Consequently, each experiment will have the same methodology to stay consistent but only varying the perforated disc. The first experiment used the 51% open area 2 in. (50.8 mm) disc with a thickness of 0.036 in. (0.914 mm) and a hole diameter of 0.14 in. (3.55 mm) (small diameter), as shown in Figure 69. The Second experiment used the 51% area open area 2 in. (50.8 mm) disc with a thickness of 0.036 in. (0.914 mm) and a hole diameter of 0.1875 in. (4.76 mm) (large diameter), as shown in Figure 70. The third experiment used the 40% open area 2 in. (50.8 mm) disc with a thickness of 0.036 in. (0.914 mm) and a hole diameter of 0.125 in. (3.175 mm) (small diameter), as shown in Figure 71. The fourth experiment used the 40% open area 2 in. (50.8 mm) disc with a thickness of 0.036 in. (0.914 mm) and a hole diameter of 0.25 in. (6.35 mm) (large diameter), as shown in Figure 72.

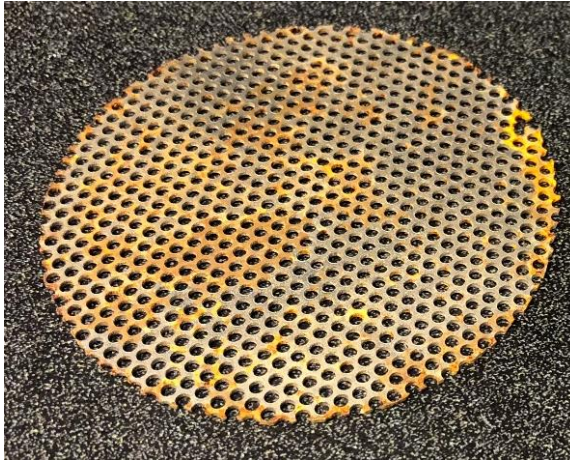


Figure 69: A perforated 2 in disc that has a 51% open area, with a hole diameter of 0.14 in (small diameter).

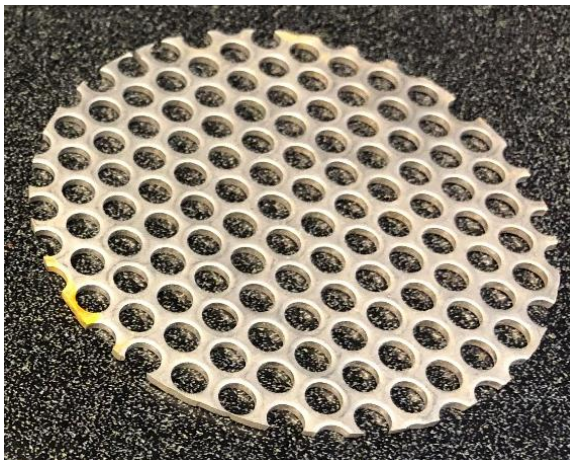


Figure 70: A perforated 2 in disc that has a 51% open area, with a hole diameter of 0.1875 in (large diameter).



Figure 71: A perforated 2 in disc that has a 40% open area, with a hole diameter of 0.125 in (small diameter).

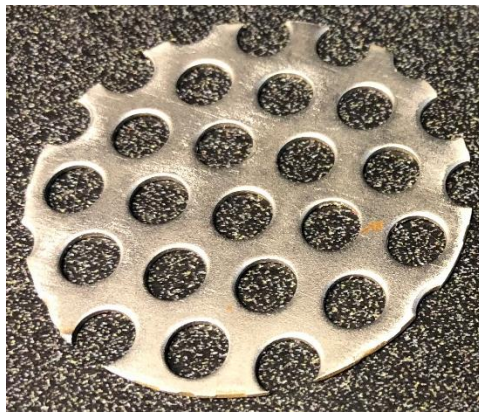


Figure 72: A perforated 2 in disc that has a 40% open area, with a hole diameter of 0.25 in (large diameter).

Finally, fluidization has occurred in all runs except for the runs done without pressure (i.e. no supply air). Therefore, when fluidization occurs the flow becomes inconsistent and erratic and thus should be taken into consideration when measuring the mass flow rate. Because fluidization has occurred in all the experiments, a measurement was done to check when fluidization occurs and at what high for each test. As this is useful information for future research and operation of the apparatus.

6.4 Results

6.4.1 Small D - Perforated Plate with 40% Open Area

Table 8 to Table 12 show the results and calculations done to calculate the mass flow rate for the perforated 2 in. (50.8 mm) disc that has a 40% open area and a hole diameter of 0.125 in. (3.175 mm) (small diameter).

Table 8: Volume flow rate and mass flow rate for the small hole diameter with a 40% open area and a pressure of 0 bar (no supply air).

Time (s)	Volume Flow (cm ³ /s)	Mass Flow (kg/s)
3.64	55.7	0.184
3.96	51.2	0.169
3.69	54.9	0.181
3.99	50.8	0.168
3.85	52.6	0.174
4.08	49.7	0.164
4.15	48.8	0.161
4.23	47.9	0.158
4.17	48.6	0.160
4.40	46.1	0.152

Average Volume flow: 50.63 cm³/s
Average Mass Flow: 0.17 kg/s
Average Velocity: 0.025 m/s

Table 9: Volume flow rate and mass flow rate for the small hole diameter with a 40% open area and a supply air pressure of 0.5 bar.

Time (s)	Volume Flow (cm³/s)	Mass Flow (kg/s)
3.98	50.9	0.168
4.98	40.7	0.134
5.16	39.3	0.130
5.93	34.2	0.118
5.48	36.9	0.122
5.85	34.6	0.114
6.61	30.7	0.101
6.83	29.7	0.098

Average Volume flow: 37.13 cm³/s
Average Mass Flow: 0.12 kg/s
Average Velocity: 0.018 m/s

Table 10: Volume flow rate and mass flow rate for the small hole diameter with a 40% open area and a supply air pressure of 1 bar.

Time (s)	Volume Flow (cm³/s)	Mass Flow (kg/s)
12.62	16.1	0.0523
12.37	16.4	0.0541
12.35	16.4	0.0542
12.40	16.3	0.0540
14.42	14.1	0.0464
15.33	13.2	0.0436
15.94	12.7	0.0420

Average Volume flow: 15.03 cm³/s
Average Mass Flow: 0.05 kg/s
Average Velocity: 0.007 m/s

Table 11: Volume flow rate and mass flow rate for the small hole diameter with a 40% open area and a supply air pressure of 1.5 bar.

Time (s)	Volume Flow (cm³/s)	Mass Flow (kg/s)
18.41	11.	0.0363
18.60	10.9	0.0360
19.13	10.6	0.0350
18.74	10.8	0.0357
18.40	11.	0.0364
19.38	10.5	0.0345

Average Volume flow: 10.8 cm³/s
Average Mass Flow: 0.036 kg/s
Average Velocity: 0.005 m/s

Table 12: Volume flow rate and mass flow rate for the small hole diameter with a 40% open area and a supply air pressure of 2 bar.

Time (s)	Volume Flow (cm³/s)	Mass Flow (kg/s)
20.16	10.1	0.0332
20.03	10.1	0.0334
20.98	9.7	0.0319

Average Volume flow: 9.94 cm³/s
Average Mass Flow: 0.033 kg/s
Average Velocity: 0.005 m/s

6.4.2 Large D - Perforated Plate with 40% Open Area

Table 13 to Table 17 show the results and calculations done to calculate the mass flow rate for the perforated 2 in. (50.8 mm) disc that has a 40% open area and a hole diameter of 0.25 in. (6.35 mm) (large diameter).

Table 13: Volume flow rate and mass flow rate for the large hole diameter with a 40% open area and a supply air pressure of 0 bar.

Time (s)	Volume Flow (cm³/s)	Mass Flow (kg/s)
2.03	99.8	0.329
2.15	94.3	0.311
2.28	88.9	0.293
2.18	92.9	0.307
2.18	93.0	0.307
2.30	88.1	0.291
2.19	92.5	0.305
2.30	88.1	0.291
2.32	87.4	0.288

Average Volume flow: 91.68 cm³/s
Average Mass Flow: 0.3 kg/s
Average Velocity: 0.045 m/s

Table 14: Volume flow rate and mass flow rate for the large hole diameter with a 40% open area and a supply air pressure of 0.5 bar.

Time (s)	Volume Flow (cm³/s)	Mass Flow (kg/s)
4.26	47.6	0.157
5.06	40.1	0.132
4.41	45.9	0.152
4.22	48.0	0.159
4.37	46.3	0.153

Average Volume flow: 45.6 cm³/s
Average Mass Flow: 0.15 kg/s
Average Velocity: 0.022 m/s

Table 15: Volume flow rate and mass flow rate for the small hole diameter with a 40% open area and a supply air pressure of 1 bar.

Time (s)	Volume Flow (cm³/s)	Mass Flow (kg/s)
5.03	40.3	0.133
5.78	35.1	0.116
5.77	35.1	0.116
5.80	34.9	0.115
5.97	33.9	0.112

Average Volume flow: 35.87 cm³/s
Average Mass Flow: 0.12 kg/s
Average Velocity: 0.0177 m/s

Table 16: Volume flow rate and mass flow rate for the large hole diameter with a 40% open area and a supply air pressure of 1.5 bar.

Time (s)	Volume Flow (cm³/s)	Mass Flow (kg/s)
6.21	32.6	0.107
6.66	30.4	0.101
6.09	33.3	0.109

Average Volume flow: 32.12 cm³/s
Average Mass Flow: 0.11 kg/s
Average Velocity: 0.016 m/s

Table 17: Volume flow rate and mass flow rate for the large hole diameter with a 40% open area and a supply air pressure of 2 bar.

Time (s)	Volume Flow (cm³/s)	Mass Flow (kg/s)
8.46	23.9	0.0791
8.97	22.6	0.0746

Average Volume flow: 23.28 cm³/s
Average Mass Flow: 0.077 kg/s
Average Velocity: 0.011 m/s

6.4.3 Small D - Perforated Plate with 51% Open Area

Table 18 to Table 22 show the results and calculations done to calculate the mass flow rate for the perforated 2 in. (50.8 mm) disc that has a 51% open area and a hole diameter of 0.14 in. (3.55 mm) (small diameter).

Table 18: Volume flow rate and mass flow rate for the small hole diameter with a 51% open area and a supply air pressure of 0 bar.

Time (s)	Volume Flow (cm ³ /s)	Mass Flow (kg/s)
4.59	44.2	0.146
5.11	39.7	0.131
5.29	38.3	0.126
5.4	37.5	0.124
5.51	36.8	0.121
5.1	39.7	0.131
5.43	37.3	0.123
5.63	36.0	0.119
5.9	34.4	0.113
5.86	34.6	0.114
5.66	35.8	0.118

Average Volume flow: 37.66 cm³/s
Average Mass Flow: 0.124 kg/s
Average Velocity: 0.02 m/s

Table 19: Volume flow rate and mass flow rate for the small hole diameter with a 51% open area and a supply air pressure of 0.5 bar.

Time (s)	Volume Flow (cm³/s)	Mass Flow (kg/s)
7.13	28.4	0.09381
7.09	28.6	0.09433
7.03	28.8	0.09514
6.59	30.8	0.10150
7.28	27.8	0.09190
7.39	27.4	0.09051
8.67	23.4	0.07714

Average Volume flow: 27.9 cm³/s
Average Mass Flow: 0.092 kg/s
Average Velocity: 0.014 m/s

Table 20: Volume flow rate and mass flow rate for the small hole diameter with a 51% open area and a supply air pressure of 1 bar.

Time (s)	Volume Flow (cm³/s)	Mass Flow (kg/s)
8.23	24.6	0.0813
8.11	24.9	0.0825
9.08	22.3	0.0736
10.3	19.7	0.0649
9.65	21.0	0.0693

Average Volume flow: 22.53 cm³/s
Average Mass Flow: 0.074 kg/s
Average Velocity: 0.011 kg/s

Table 21: Volume flow rate and mass flow rate for the small hole diameter with a 51% open area and a supply air pressure of 1.5 bar.

Time (s)	Volume Flow (cm³/s)	Mass Flow (kg/s)
15.83	12.8	0.0423
15.81	12.8	0.0423
15.96	12.7	0.0419

Average Volume flow: 12.77 cm³/s
Average Mass Flow: 0.042 kg/s
Average Velocity: 0.006 m/s

Table 22: Volume flow rate and mass flow rate for the small hole diameter with a 51% open area and a supply air pressure of 2 bar.

Time (s)	Volume Flow (cm³/s)	Mass Flow (kg/s)
16.27	12.5	0.0411
16.78	12.1	0.0340
16.94	11.9	0.0395

Average Volume flow: 12.16 cm³/s
Average Mass Flow: 0.04 kg/s
Average Velocity: 0.006 m/s

6.4.4 Large D - Perforated Plate with 51% Open Area

Table 23 to Table 27 show the results and calculations done to calculate the mass flow rate for the perforated 2 in. (50.8 mm) disc that has a 51% open area and a hole diameter of 0.1875 in. (4.76 mm) (large diameter).

Table 23: Volume flow rate and mass flow rate for the large hole diameter with a 51% open area and a supply air pressure of 0 bar.

Time (s)	Volume Flow (cm ³ /s)	Mass Flow (kg/s)
2.48	81.7	0.270
2.34	86.6	0.286
2.75	73.7	0.243
2.4	84.5	0.279
2.81	72.1	0.238
2.56	79.2	0.261
3.02	67.1	0.221
2.87	70.6	0.233
2.73	74.2	0.245
2.27	89.3	0.297

Average Volume flow: 77.905 cm³/s
Average Mass Flow: 0.26 kg/s
Average Velocity: 0.04 m/s

Table 24: Volume flow rate and mass flow rate for the large hole diameter with a 51% open area and a supply air pressure of 0.5 bar.

Time (s)	Volume Flow (cm³/s)	Mass Flow (kg/s)
3.8	53.3	0.176
4.84	41.8	0.138
6.95	29.2	0.096
6.28	32.3	0.107
5.88	34.5	0.114

Average Volume flow: 38.22 cm³/s
Average Mass Flow: 0.13 kg/s
Average Velocity: 0.019 m/s

Table 25: Volume flow rate and mass flow rate for the large hole diameter with a 51% open area and a supply air pressure of 1 bar.

Time (s)	Volume Flow (cm³/s)	Mass Flow (kg/s)
5.15	39.4	0.129
6.09	33.3	0.109
6.96	29.1	0.0961
8.67	23.4	0.0771
10.43	19.4	0.0641
11.61	17.5	0.0576

Average Volume flow: 27 cm³/s
Average Mass Flow: 0.09 kg/s
Average Velocity: 0.013 m/s

Table 26: Volume flow rate and mass flow rate for the large hole diameter with a 51% open area and a supply air pressure of 1.5 bar.

Time (s)	Volume Flow (cm³/s)	Mass Flow (kg/s)
8.92	22.7	0.0750
10.43	19.4	0.0641
11.06	18.3	0.0605
12.17	16.7	0.0550
12.51	16.2	0.0535
12.65	16.	0.0529

Average Volume flow: 18.23 cm³/s
Average Mass Flow: 0.06 kg/s
Average Velocity: 0.009 m/s

Table 27: Volume flow rate and mass flow rate for the large hole diameter with a 51% open area and a supply air pressure of 2 bar.

Time (s)	Volume Flow (cm³/s)	Mass Flow (kg/s)
10.16	19.9	0.0658
10.85	18.7	0.0616
11.61	17.5	0.0576
12.98	15.6	0.0515
13.63	14.9	0.0491

Average Volume flow: 17.31 cm³/s
Average Mass Flow: 0.057 kg/s
Average Velocity: 0.009 m/s

6.5 Uncertainty Analysis

The uncertainty analysis is done to validate the numbers calculated in this experiment. There are two main uncertainties that were established as these were the measured variables. The first measured variable is the volume, the volume was measured using the internal diameter of the pipe and the height. This was done using a tape measure with the lowest increment of 0.1 cm thus the uncertainty for that was ± 0.1 cm for each dimension measured. Since this was a volume the 0.1 cm is cubed and thus ± 0.001 cm³ for the volume. The volume remained constant throughout the experiment, so it was only measured once in the beginning. On the other hand, the time was constantly changing as this was measured to calculate the mass flow rate of the flow. The time was measured using a stopwatch with an uncertainty of ± 0.01 s. Therefore, I needed to calculate the statistical uncertainty, U_A , and the bias uncertainty, U_B . to be able to combine them and calculate the final combined uncertainty, U_C . U_C is the square root of the sum of squares of U_A and U_B , as the equation below shows,

$$U_C = \sqrt{U_A^2 + U_B^2} \quad (27)$$

A summary of all the uncertainties can be found in the below tables and more details about the calculation can be found in the appendix.

Table 28: Uncertainty analysis for the particulate mass flow of the 40% open area with a small diameter.

Diameter	Open Area	Pressure (bar)	Mass Flow (kg/s)	U_C	Upper Limit	Lower Limit
Small	40%	0.0	0.167	0.007	0.174	0.160
Small	40%	0.5	0.123	0.019	0.141	0.104
Small	40%	1.0	0.050	0.005	0.055	0.045
Small	40%	1.5	0.036	0.001	0.036	0.035
Small	40%	2.0	0.033	0.002	0.035	0.031

Table 29: Uncertainty analysis for particulate mass flow of the 40% open area with a large diameter.

Diameter	Open Area	Pressure (bar)	Mass Flow (kg/s)	U_C	Upper Limit	Lower Limit
Large	40%	0.0	0.303	0.010	0.313	0.292
Large	40%	0.5	0.150	0.013	0.164	0.137
Large	40%	1.0	0.118	0.010	0.129	0.108
Large	40%	1.5	0.106	0.012	0.118	0.094
Large	40%	2.0	0.077	0.029	0.105	0.048

Table 30: Uncertainty analysis for particulate mass flow of the 51% open area with a small diameter.

Diameter	Open Area	Pressure (bar)	Mass Flow (kg/s)	U_C	Upper Limit	Lower Limit
Small	51%	0.0	0.124	0.006	0.130	0.118
Small	51%	0.5	0.092	0.007	0.099	0.085
Small	51%	1.0	0.074	0.009	0.084	0.065
Small	51%	1.5	0.042	0.001	0.043	0.042
Small	51%	2.0	0.040	0.002	0.042	0.038

Table 31: Uncertainty analysis for particulate mass flow of the 51% open area with a large diameter.

Diameter	Open Area	Pressure (bar)	Mass Flow (kg/s)	U_C	Upper Limit	Lower Limit
Large	51%	0.0	0.257	0.064	0.321	0.193
Large	51%	0.5	0.126	0.040	0.166	0.087
Large	51%	1.0	0.089	0.029	0.118	0.060
Large	51%	1.5	0.060	0.009	0.069	0.051
Large	51%	2.0	0.057	0.009	0.066	0.049

6.6 Discussion

In the 40% open area perforated disc experiment runs, the data was collected, and an average mass flow rate was calculated for each pressure. After that, the graph in Figure 73 was created using the data from the two experiments conducted one for the small hole diameter perforated disc and the other one for the large hole diameter perforated disc. As can be seen in Figure 73, the solid dots are the average mass flow rate that was calculated using the raw data collected while running the experiments. On the other hand, the dotted curves are exponential curves of the curve that best fits the data. Further, the blue dots are representing the small hole diameter disc experiment, while the orange dots are representing the large hole diameter disc experiment. Similarly, the dotted blue exponential curve is the best fit curve from the calculated values for the small hole diameter disc experiment. While the dotted orange exponential curve is the best fit curve from the calculated values for the large hole diameter disc experiment.

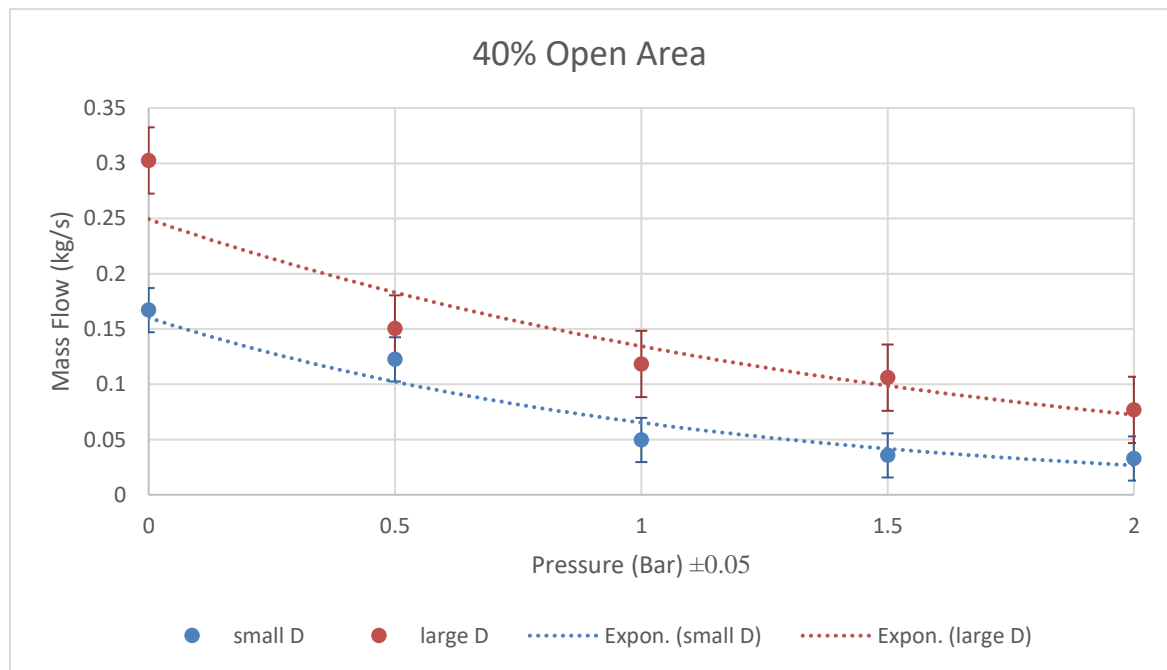


Figure 73: Graph showing the 40% open area mass flow rates both for the small and large hole diameters.

In the 51% open area perforated disc experiment runs, the data was collected, and an average mass flow rate was calculated for each pressure. After that, the graph in Figure 74 was created using the data from the two experiments conducted one for the small hole diameter perforated disc and the other one for the large hole diameter perforated disc. As can be seen in Figure 74, the solid dots are the average mass flow rates that were calculated using the raw data collected while running the experiments. But the dotted curves were exponential curves of the best fit for the data. Further, the blue dots are representing the small hole diameter disc experiment, while the orange dots are representing the large hole diameter disc experiment. Similarly, the dotted blue exponential curve is the best fit curve from the calculated values for the small hole diameter disc experiment. While the dotted orange exponential curve is the best fit curve from the calculated values for the large hole diameter disc experiment.

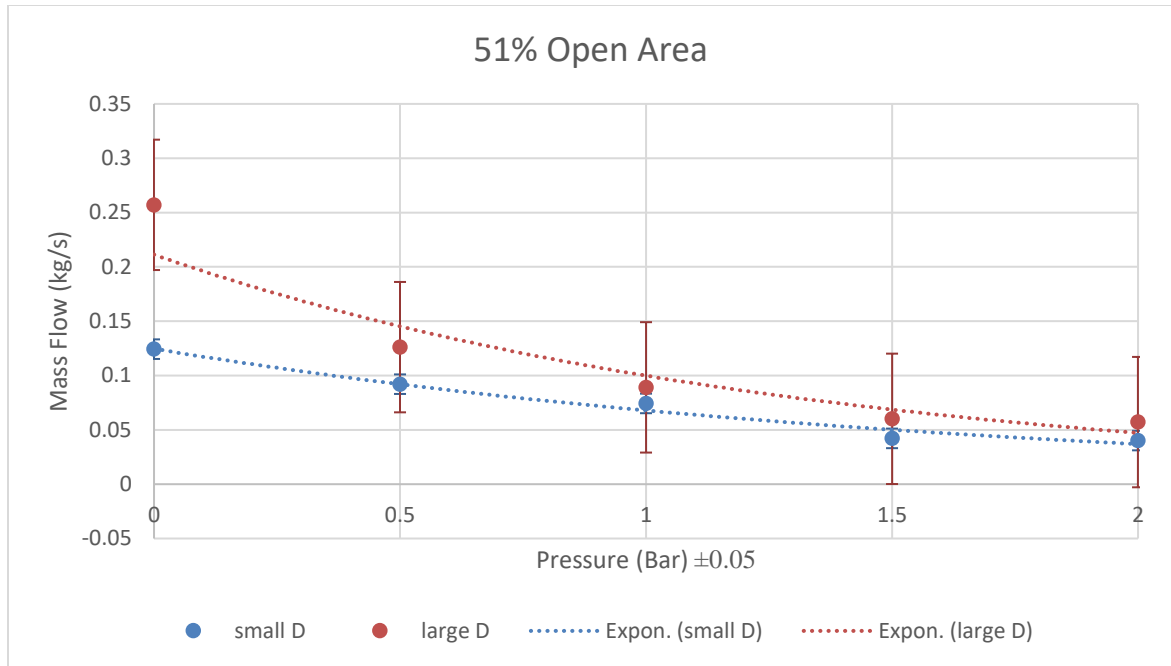


Figure 74: Graph showing the 51% open area mass flow rates both for the small and large hole diameters.

Finally, both graphs from Figure 73 and Figure 74, were combined into one graph in Figure 75, to compare all the data and check for any correlations. As can be seen in Figure 75, all the exponential curves are converging to a value close to 0.05 kg/s. Due to the limitations of the PVC pipes used in the experiment the maximum allowable pressure was 2 bars, this data is not complete but can serve as a first step into future iterations for higher pressures. Furthermore, there could have been some human error while reading the data as well as some inconsistency in the voids in the particle bed each time it was refilled. Therefore, more iterations are needed to confirm a more accurate correlation between the data. Moreover, the reason for choosing the specific sizes in this experiment is due to availability of the material in those sizes and open area ratios. However, in future research these perforated discs can be manually designed to test for a specific correlation between open ratio, hole diameter, and mass flow rates.

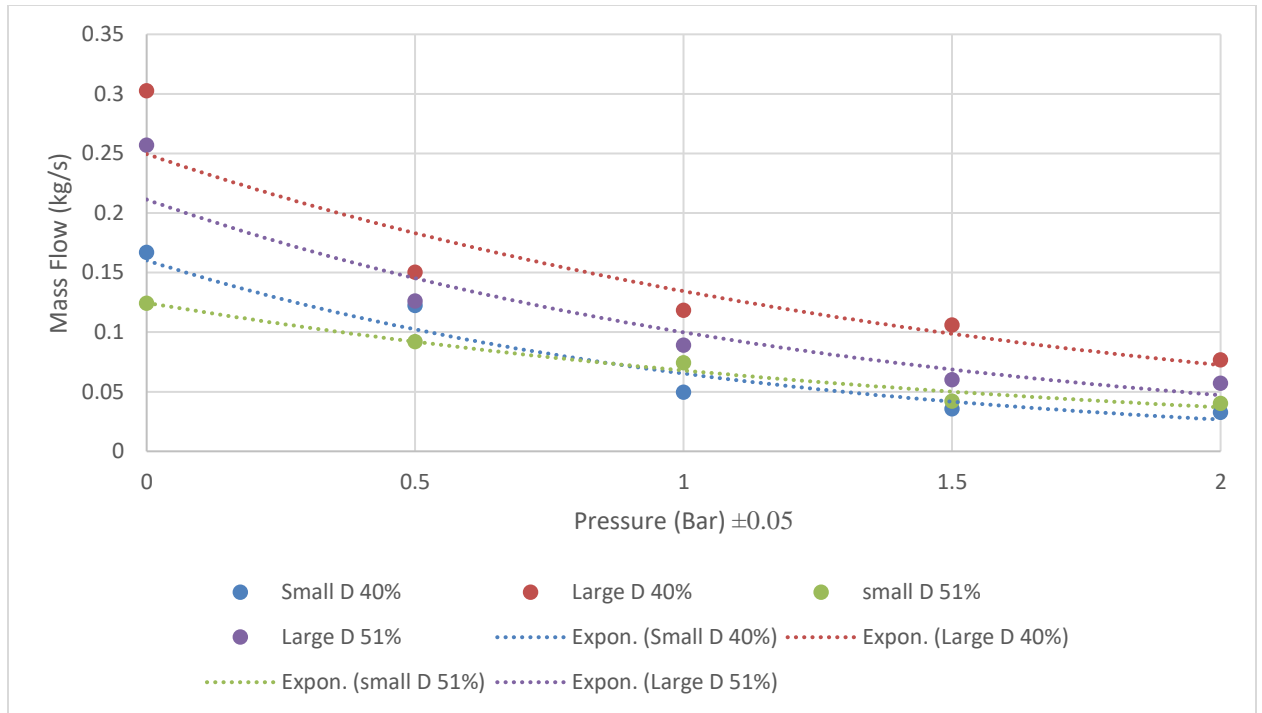


Figure 75: Graph showing the 40% and 51% open area mass flow rates both for the small and large hole diameters for each open area.

6.7 Conclusion

Consequently, it is evident from the data collected that the mass flow rate decreases as the pressure increases. It is also evident that fluidization occurs at specific heights in the bed depending on the pressure in the heat exchanger. Thus, it is important to keep note of this while scaling up this system as fluidization can have severe disruptions in the particle flow and can dramatically change the effectiveness of the heat exchanger. Furthermore, it is vital to note that fluidization was recorded in this experiment when bubbling was observed. When fluidization does occur, the particles are mixed vigorously in the particle column and there are sometimes air ejections from the bed itself. However, with no fluidization or bridging the flow is uniform and consistent.

Bridging also occurred at several times during the experiments, but no pattern was identified. Bridging is when the particles create a bridge around the perforated disc holes and stop the flow. When this happens, the pressure from the air and the pressure from the weight of the particles are balanced and thus the particle flow stops. Bridging was identified only in the 51% open area and not the 40% open area. But earlier experiments that were conducted, when the air outlet and the particle inlet were the same. I have found that bridging occurs at specific heights depending on the pressure, open area, and hole diameter. This should be investigated further in future research as bridging might be a very significant aspect in controlling particle flow. Moreover, understanding the factors that affect the particulate mass flow at various pressures is very important when scaling up. Future research should also reiterate this experiment at various particle temperatures as this might contribute to the particle mass flow.

CHAPTER 7. INVESTIGATION OF PARTICLE FLOW

7.1 Introduction

The purpose of this chapter is to identify several important aspects of particle flow that was noticed throughout the conducted experiments. These properties of the flow and particles would enable us to understand the flow better and develop better exchanger designs. The terminal velocity of a single particle was first analyzed theoretically, then particle fluidization was studied. Further, particle entrainment was observed and needs to be addressed as particle entrained through the air outlet will affect the performance and life of the turbine downstream. Fluidization was also calculated theoretically based on some assumptions that were made based and, on the data, available. Finally, some designs were simulated on Blender to establish a preliminary conception of the particle flow.

7.2 Particle Fluidization

As discussed in chapter 6, the fluidization that occurred during the experimental runs were further investigated. An experiment was designed to measure the height at which fluidization occurs. This will help identify the height of the hot bin and further understand particle flow properties and prevent fluidization during entrainment experiments. The experiments were conducted on the two perforated plates with the 40% open area as well as for the two perforated plates with the 51% open area. Table 32 and

Table 33 show the results recorded for each pressure. Since fluidization makes the flow inconsistent and it was observed while conducting several experiments, such as the entrainment experiment. This experiment was conducted to know at what height fluidization occurs and try to avoid these heights when conducting other experiments.

Table 32: Fluidization height for a perforated disc with a 51% open area.

	Small D	Large D
Pressure (bar)	Fluidization Height (cm)	Fluidization Height (cm)
± 0.05	± 0.1 cm	± 0.1 cm
0.0	0	0
0.5	14	27
1.0	25	58
1.5	46	74
2.0	62	93

Table 33: Fluidization height for a perforated disc with a 40% open area.

	Small D	Large D
Pressure (bar)	Fluidization Height (cm)	Fluidization Height (cm)
± 0.05	± 0.1 cm	± 0.1 cm
0.0	0	0
0.5	23	49
1.0	28	53
1.5	37	74
2.0	64	78

The preceding data may indicate that a simple perforated plate greatly increases the resistance of the particulate column to bubbling fluidization. This observation has

important implications to direct contact heat exchanger design and deserves further consideration. Furthermore, the observed data also indicates that the perforated plate open area and hole diameter seems to affect the height at which the bed fluidizes. Consequently, a standpipe could be a feasible option, as the height required for the standpipe can be reduced based on the type of perforated plate used. However, further investigation is needed to test such an application.

7.3 Particle Entrainment

7.3.1 Calculated Entrainment

Calculating particle entrainment will allow us to predict and by design eliminate or minimize any particle carryover to the turbine downstream. The calculation will assist in designing the heat exchanger and will make sure that the turbine is not damaged by the entrained particles. The calculations were done by calculating the terminal velocity at which the viscous drag on the particle equals its weight. More information can be found in the appendix. The first set of calculations were done in Engineering Equation Solver (EES) using four pressure ratios and by varying the temperature as well as the particle size. The results of these calculations can be seen in the series of Figure 76 to Figure 79. Figure 76 shows the calculation was done at 0.5 bars of pressure for four particle sizes; 100, 300, 500, and 1000 microns. Furthermore, the temperature was varied from 25°C to 1200°C. Then Figure 77 shows the calculation was done at 1 bar of absolute pressure for four particle sizes; 100, 300, 500, and 1000 microns. Furthermore, the temperature was varied from 25°C to 1200°C. After that Figure 78 shows the calculation was done at 1.5 bars of pressure for four particle sizes; 100, 300, 500, and 1000 microns. Furthermore, the

temperature was varied from 25°C to 1200°C. Finally, Figure 79 shows the calculation done at 2 bars of pressure for four particle sizes; 100, 300, 500, and 1000 microns. Also, the temperature was varied from 25°C to 1200°C.

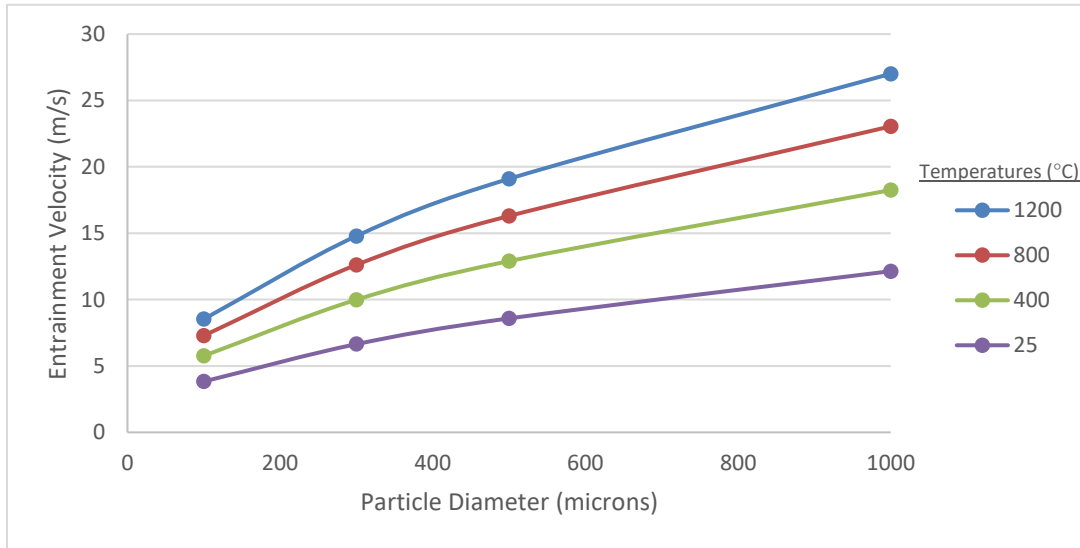


Figure 76: Entrainment velocities for an absolute pressure of 0.5 bars.

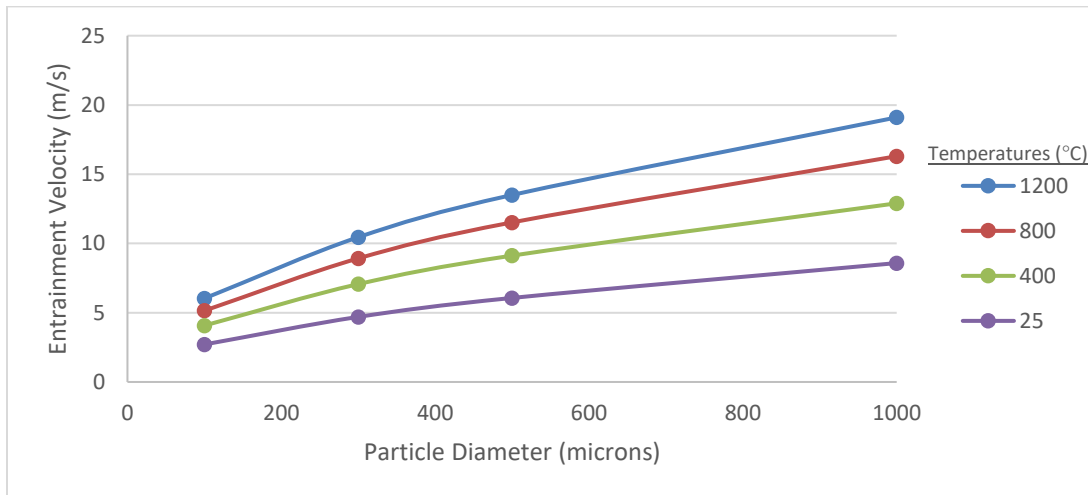


Figure 77: Entrainment velocities for an absolute pressure of 1 bar.

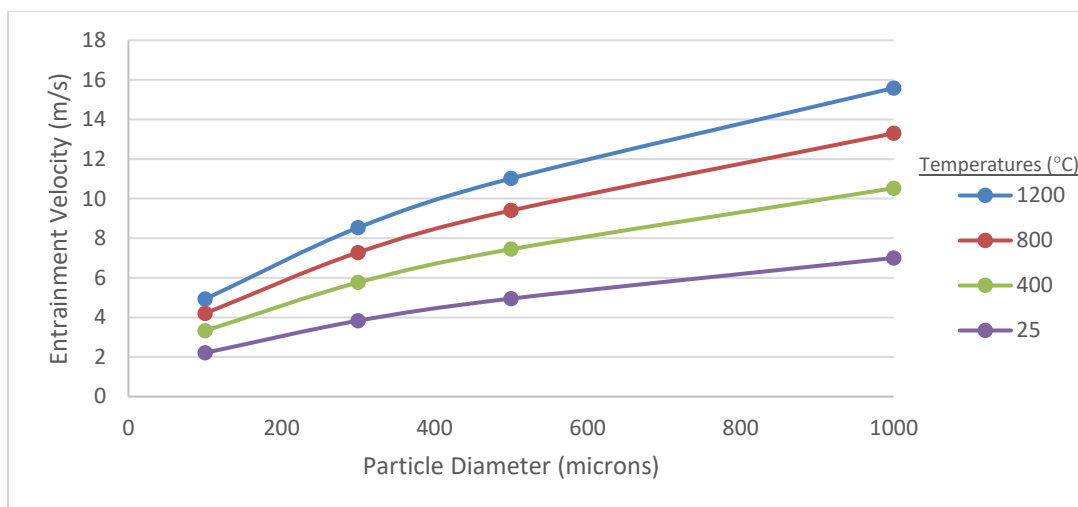


Figure 78: Entrainment velocities for an absolute pressure of 1.5 bars.

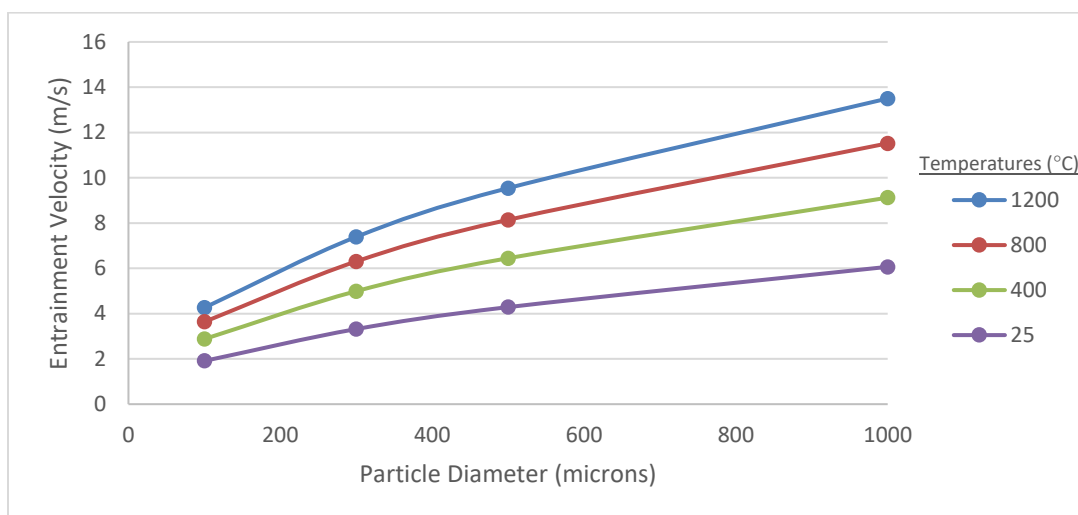


Figure 79: Entrainment velocities for an absolute pressure of 2 bars.

Another set of calculations were also conducted to analyze the scale up system. The systems have higher pressure ratio based on values in the industry, a potential turbine for this system can operate at 4 bars and another turbine can operate at a higher pressure of 15.7 bars. This system had slightly different conditions from the initial calculations that were conducted. The temperatures for this system were higher as well as the pressure and the range of particle size is larger. Using EES, 2 pressure ratios were examined on particle

sizes ranging from 50 microns to 1200 microns and four temperatures were examined; 300°C, 600°C, 900°C, and 1200°C. Figure 80 and Figure 81 shows the results from the calculations and it can be inferred as the pressure ratio increases the entrainment velocity decreases. Moreover, as the temperature increases the entrainment velocity increases due to the decrease in air density and thus the decrease in the drag force on the particle.

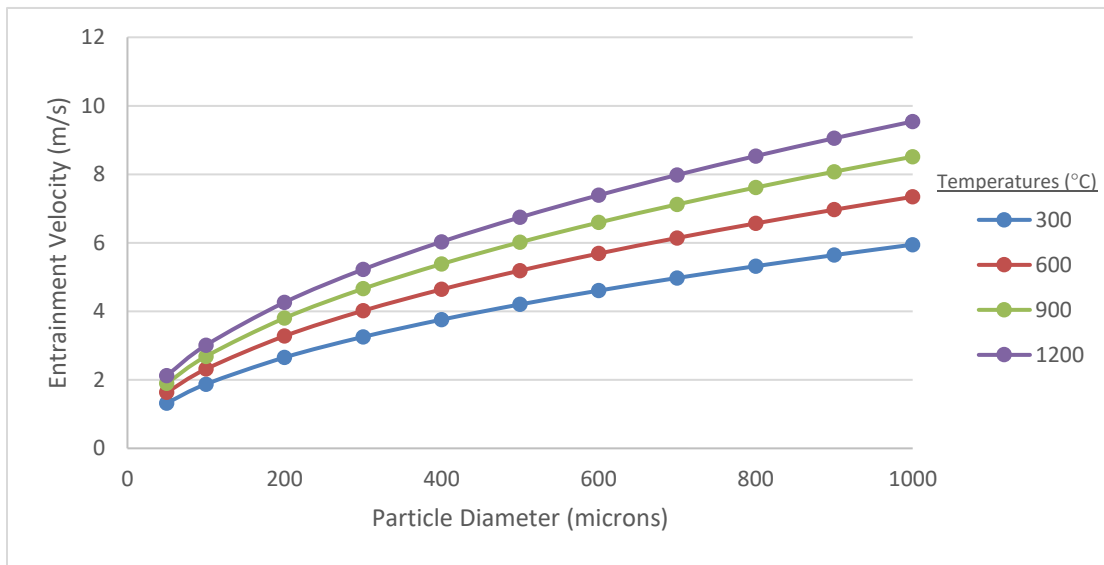


Figure 80: Entrainment velocities for an absolute pressure of 4 bars.

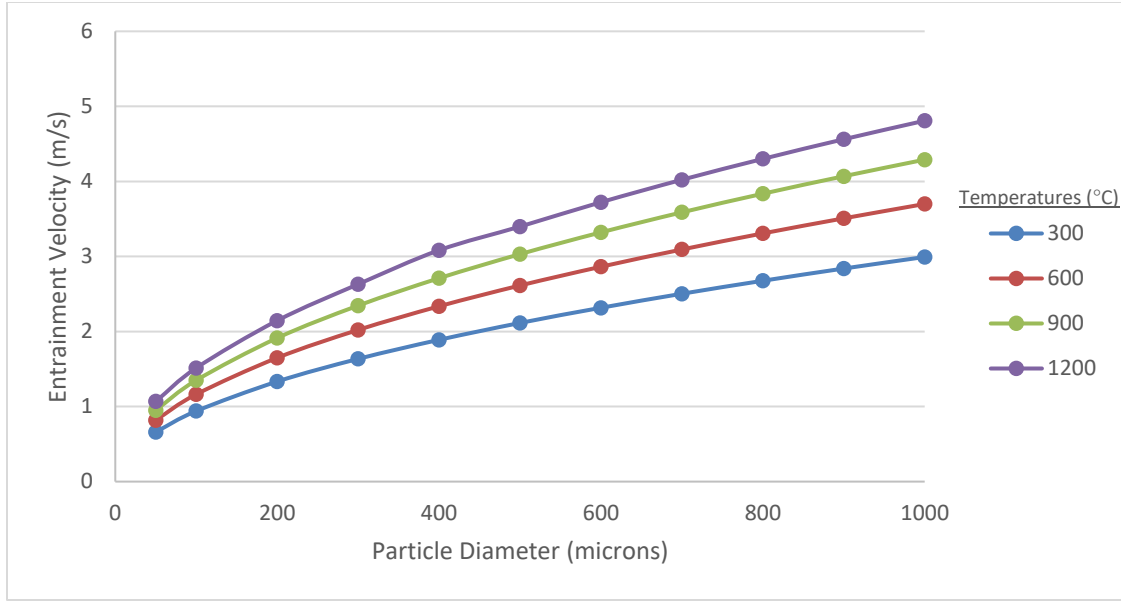


Figure 81: Entrainment velocities for an absolute pressure of 15.7 bars.

7.3.2 Experiment Entrainment

To be able to verify the theoretical calculations that were done at atmospheric pressure, we need to conduct experiments that would allow us to measure mass flow, particle entrainment, and air velocities. Consequently, this section discusses the setup and the measuring equipment used as well as the results. First, the thermo-anemometer, shown in Figure 82 was used to measure the air velocity at two locations of the pipe. This is a TSI 8350 Veloci-Calc air velocity meter that has an specified accuracy of ± 3 fpm. [44]. The velocity is measured near the center and near the wall of the pipe as shown in Figure 83. This type of measurement is sometimes referred to as duct traverse [45]. In this measurement, more samples are taken depending on the size of the duct. However, since the pipe diameter in this case is only 2 in., only two points were needed, one near the center and the other near the wall. The exact locations were determined using the traverse method and thus the first distance is $0.316 R$, where R is the radius of the pipe. This would thus

measure 1.75 cm from the edge of the pipe. The second location, which is close to the wall, is $0.707 R$, where R is the radius of the pipe. This would thus measure 0.75 cm from the edge of the pipe [45]. Figure 84 shows an example of how the measurements were taken. The velocities were measured at various inlet supply air pressures to have a wide velocity range in which we can test the particle entrainment on. Furthermore, the velocities were measured ten times for each location in the pipe and each pressure. This was done while the gate valve was closed, and all the air is coming out of the air outlet. For this experiment we are assuming there is zero to minimal air leakage through the bed.



Figure 82: Thermo-anemometer (TSI VelociCalc Model 8350) that was used to measure the air velocities in the pipe.

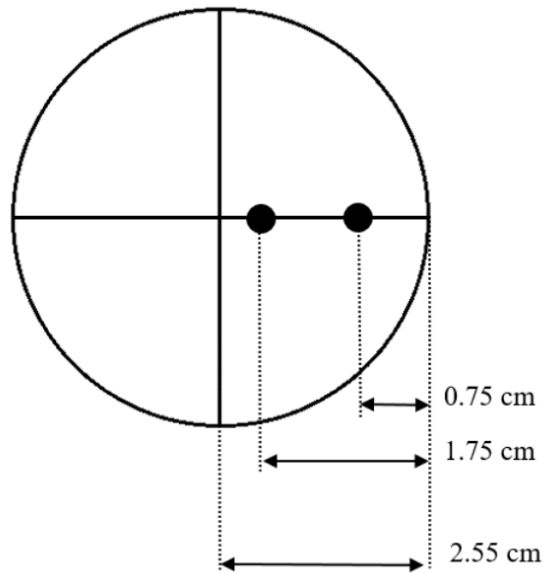


Figure 83: Location of measurement points in the 2-in. pipe both near the center and near the walls.



Figure 84: Thermo-anemometer that was used to measure the air velocity at two radial locations in the 2-in. pipe.



Figure 85: Scale (Ohaus GT 210) that was used to measure the mass of the particles entrained in the outlet filter.

The particles were then filled in the material column and the inlet pressure was set. A particle collector filter (a common knitted stocking) was placed on the outlet to collect any particles entrained during the experiment. The particle collector allows air to go out normally but not particles, thus it's a feasible way to capture particles. After filling the material column and setting the pressure at the inlet, the gate valve was opened, and the experiment starts. Time was measured as soon as the valve was open and until the material column is empty. The time will help us calculate the mass flow rate of the particles and thus the particle speed. Furthermore, the particles entrained were collected and then put on a mass scale, shown in Figure 85 to measure their mass. This is a GT 210 Ohaus electronic balance scale with an accuracy of $\pm 5\%$ [46]. Since the volume of the particle bed used in each run was measured and the density of the particle is known, we were able to calculate the total mass. Knowing the total mass and the mass entrained, we develop a mass fraction

to represent the mass entrained compare to the average velocities that were measured. The velocity calculated was based on the ten measurements taken near the center and near the walls of the pipe, which were then averaged to represent the velocity in the pipe.

Consequently, after conducting the experiment for six inlet pressures each providing a different air velocity at the exit, we could quantify the data and produce some useful results. Table 34 to Table 40 show the results for each run, in details. Figure 86 shows the summary of the results showing that as velocity increases the percentage of entrained particles increases. It can also be seen from the tables that the air velocity near the walls are slightly lower than the air velocities in the center of the pipe, which was expected, as the Reynold numbers for the air flow, which range from 5800 to 28800, indicated that the air flows were all in the turbulent region. Finally, uncertainty analysis was conducted on the data and can be seen in the appendix. The statistical uncertainty was calculated, and the bias uncertainty is ± 3 fpm or 0.015 m/s [44]. The coverage factor (K_c), which is based on the level of confidence of the data, has shown to be 2.62 for all the data.

Table 34: Air velocities in fpm at the outlet near the wall and at the center of the pipe for a 2-psi inlet pressure.

Wall	Center	Average
330	341	336
334	342	338
328	344	336
332	341	337
334	342	338
329	339	334
325	340	333
328	340	334
331	341	336
332	340	336

Average Velocity (FPM)	336
Average Velocity (m/s)	1.71
Mass Entrained (g)	0.00
Time (s)	25.8
Mass Total	4864.4
Mass Flow (kg/s)	0.19
Mass Ratio	0.00%
Kc	2.62

Table 35: Air velocities in fpm at the outlet near the wall and at the center of the pipe for a 5-psi inlet pressure.

Wall	Center	Average
440	461	451
436	463	450
431	458	445
433	460	447
441	457	449
442	460	451
446	463	455
445	462	454
436	465	451
443	457	450

Average Velocity (FPM)	450
Average Velocity (m/s)	2.29
Mass Entrained (g)	0.00
Time (s)	25.0
Mass Total	4864.4
Mass Flow (kg/s)	0.19
Kc	2.62

Table 36: Air velocities in fpm at the outlet near the wall and at the center of the pipe for a 10-psi inlet pressure.

Wall	Center	Average
540	553	547
539	552	546
534	555	545
534	556	545
540	555	548
537	557	547
539	555	547
536	556	546
533	553	543
537	557	547

Average Velocity (FPM)	546
Average Velocity (m/s)	2.77
Mass Entrained (g)	1.38
Time (s)	26.7
Mass Total	4864.4
Mass Flow (kg/s)	0.18
Mass Ratio	0.03%
Kc	2.62

Table 37: Air velocities in fpm at the outlet near the wall and at the center of the pipe for a 20-psi inlet pressure.

Wall	Center	Average
869	902	886
864	900	882
869	897	883
873	903	888
866	901	884
869	898	884
873	897	885
870	895	883
866	897	882
864	898	881

Average Velocity (FPM)	884
Average Velocity (m/s)	4.49
Mass Entrained (g)	9.76
Time (s)	24.8
Mass Total	4864.4
Mass Flow (kg/s)	0.20
Mass Ratio	0.20%
Kc	2.62

Table 38: Air velocities in fpm at the outlet near the wall and at the center of the pipe for a 30-psi inlet pressure.

Wall	Center	Average
1145	1192	1169
1150	1190	1170
1153	1195	1174
1147	1187	1167
1153	1188	1171
1147	1190	1169
1155	1192	1174
1147	1190	1169
1150	1187	1169
1153	1187	1170

Average Velocity (FPM)	1170
Average Velocity (m/s)	5.94
Mass Entrained (g)	50.06
Time (s)	25.6
Mass Total	4864.4
Mass Flow (kg/s)	0.19
Mass Ratio	1.03%
Kc	2.62

Table 39: Air velocities in fpm at the outlet near the wall and at the center of the pipe for a 40-psi inlet pressure.

Wall	Center	Average
1425	1508	1467
1422	1504	1463
1419	1508	1464
1425	1504	1465
1422	1508	1465
1428	1501	1465
1425	1497	1461
1424	1504	1464
1425	1508	1467
1426	1504	1465

Average Velocity (FPM)	1464
Average Velocity (m/s)	7.44
Mass Entrained (g)	75.21
Time (s)	23.4
Mass Total	4864.4
Mass Flow (kg/s)	0.21
Mass Ratio	1.55%
Kc	2.62

Table 40: Air velocities in fpm at the outlet near the wall and at the center of the pipe for a 50-psi inlet pressure.

Wall	Center	Average
1568	1765	1667
1565	1761	1663
1572	1769	1671
1578	1773	1676
1565	1769	1667
1567	1773	1670
1573	1761	1667
1572	1765	1669
1578	1769	1674
1569	1765	1667

Average Velocity (FPM)	1669
Average Velocity (m/s)	8.48
Mass Entrained (g)	105.16
Time (s)	25.4
Mass Total	4864.4
Mass Flow (kg/s)	0.19
Mass Ratio	2.16%
Kc	2.62

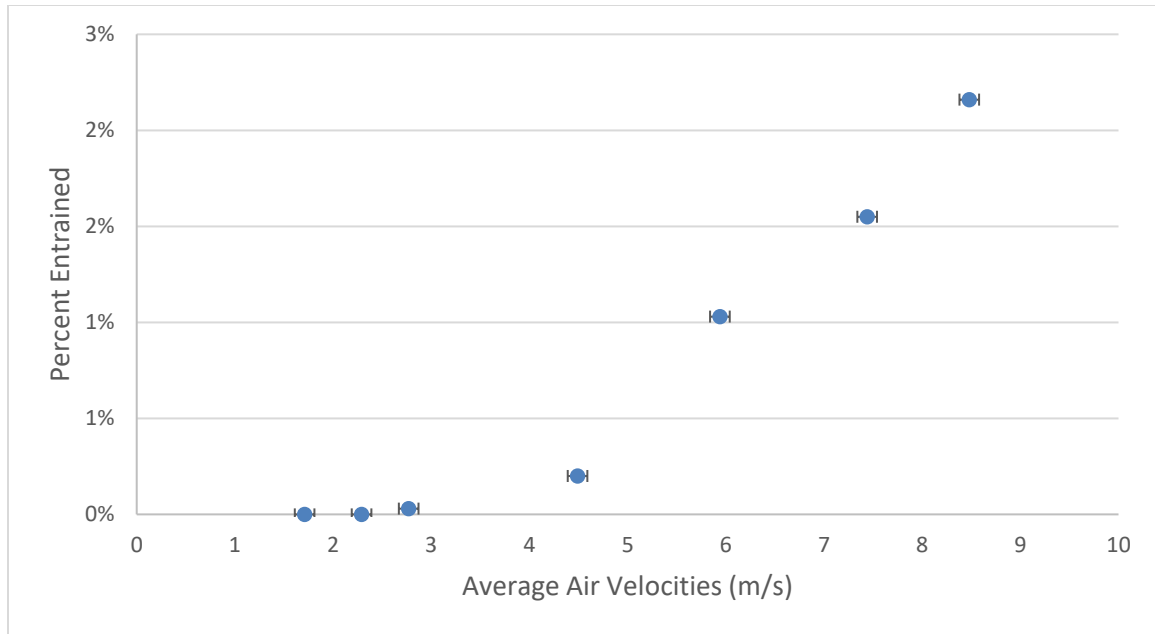


Figure 86: Average air velocity vs percentage of particles entrained at various inlet air supply pressures.

After calculating the average velocities from the measurements as well as calculating the mass fraction between the mass of the entrainment particles over the total mass of the flow, there is a need to know the particle entrainment size. The size of the entrained particles was measured using a microscope, a camera, and a microscopic slide ruler. Figure 87 shows the microscope and the camera attached. First a random sample of particles was taken from each bucket of entrained particles at various velocities. Then the particle sizes were measured using the microscopic slide ruler, which is shown in Figure 88. The result of this was the set of particle sizes shown in Figure 89. The figure shows the particle size distribution for each air velocity. The air velocities were obtained by setting the inlet pressure as shown in Table 41, each inlet pressure gives an average air velocity. Furthermore, Figure 90 shows an example of the view in the microscope and how the particle sizes were measured; further details as well as more figures of the microscopic

images are available in the appendix. Thirty particles were chosen based on how close they are to the ruler. The sizes of these particles were measured and then averaged for each air velocity.

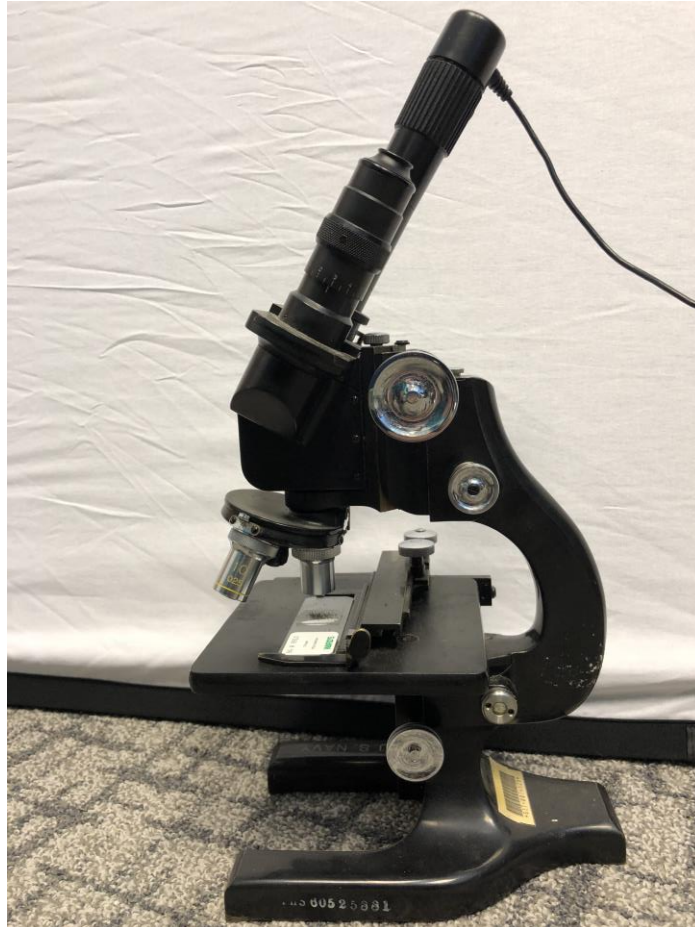


Figure 87: Microscope that was used to measure the particle sizes in the sample.



Figure 88: Microscopic view of the slide ruler that was used under the microscope to measure the entrained particle sizes.

Table 41: Average velocity measured at each inlet pressure.

Pressure Inlet (PSI) ± 0.5	Average Velocity (m/s) ± 0.05
2	1.71
5	2.29
10	2.77
20	4.49
30	5.94
40	7.44
50	8.48

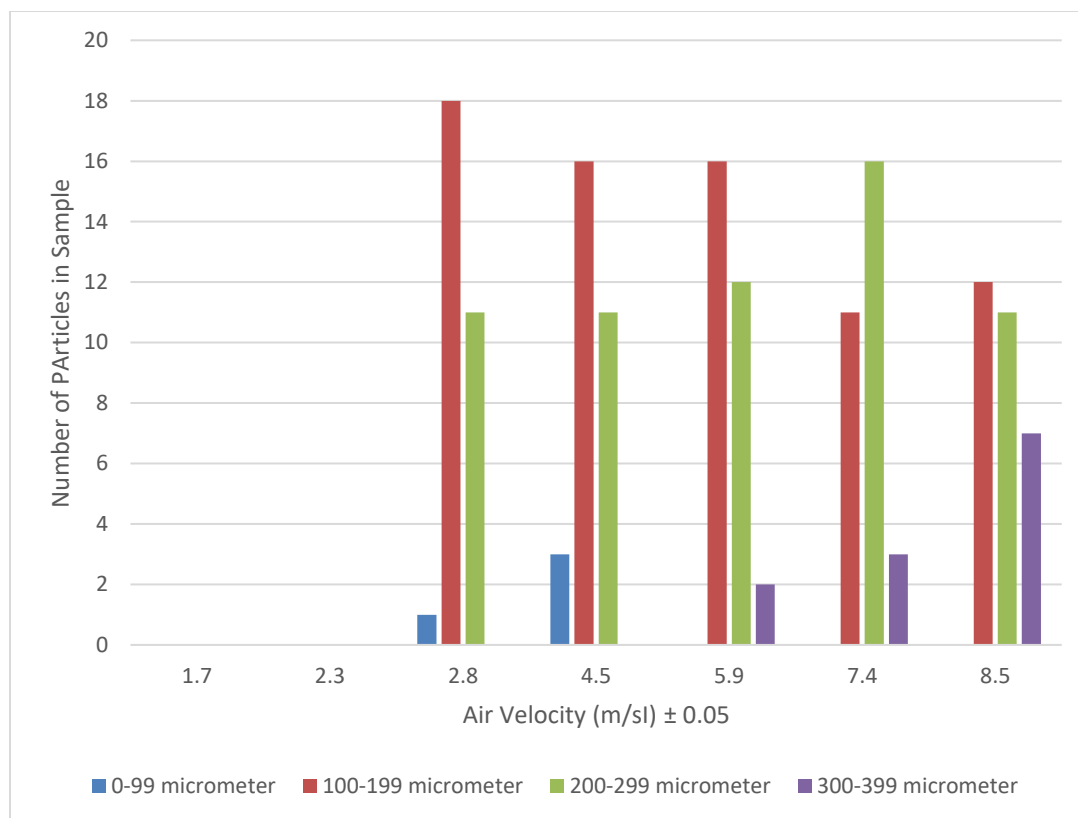


Figure 89: Particle size distribution in each sample divided into 100 micrometer segments.

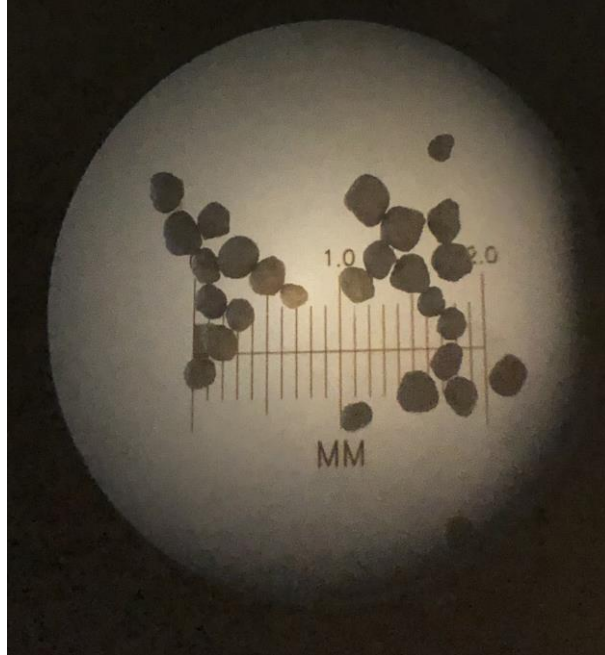


Figure 90: A sample microscopic view of measuring the particle sizes using the microscopic slide ruler.

Consequently, as the air velocity increases, the particle size entrained increases and the number of particles entrained increases. It can also be observed in Figure 89 that as the air velocity increases the particle distribution changes. At air velocities of 1.7 and 2.3 m/s there was no particle entrainment. However, starting at 2.8 m/s particles start to be entrained. Furthermore, at an air velocity of 2.8 m/s particle sizes ranged from 80 to 230 micrometer, where at an air velocity of 4.5 m/s particle sizes ranged from 80 to 260 micrometer, At an air velocity of 5.9 m/s the particle sizes ranged from 110 to 320 micrometer, at an air velocity of 7.4 m/s the particle sizes ranged from 120 to 320 micrometer, and at an air velocity of 8.5 m/s the particle sizes ranged from 140 to 340 micrometer. It was observed that 300-399 micrometer particles were only entrained starting at 5.9 m/s, for which the theoretical calculation predicted the entrainment of these particles to be 4.7 m/s. Moreover, the particle entrainment started at 2.8 m/s, for which the

theoretical calculations predict that a 100-micrometer particle will get entrained at 2.7 m/s. Therefore, it can be concluded that simple theoretical model can predict the particle entrainment at various air velocities.

7.4 Simple Particle Dynamic Simulation

The goal of this section is to get an initial estimate of how the particle flow will look like, this is meant to be only as a simple virtual visualization of the flow and is not meant to calculate any velocities or particle interaction. Therefore, the physics and menus available in Blender are highlighted in the appendix, so that the visualizations done in this section can be reiterated. Blender also uses something called Blender units, meaning everything is set to one “frame of reference”, and it is asserted that if the frame of reference does not change the physics and visualization should work well. In Blender some units were originally set to approximate a particle motion in real life. This includes setting the particle initial velocity to 0 as the particles are falling, setting the gravity as 9.81, changing the lifetime of the particle to 200 to be able to see the particle flow throughout the design, setting the particle size as 0.001, and finally selecting the size deflection mode. Moreover, the internal design was made as one part to be correctly imported into Blender and the heat exchanger tube was imported as a different object and made transparent so that the flow can be examined. This design was also made with no pressure meaning there is no air velocity component, and that only force components acting on a single falling particle are gravity and drag. It is also important to note that the internal designs mentioned here are made from a solid material. However, as discussed in chapter 5, by incorporating a porous structure for the material used, the flow can be greatly improved to mix the air with the particles.

7.4.1 Conical Design

In the cones design, shown in Figure 91 and Figure 92, the particles follow the path of the conical shapes and mix thoroughly throughout the heat exchanger. The cones have three holes that in experimental runs will be covered because of the rods holding the internal design in the heat exchanger. However, in this visualization the rods do not appear and thus some particles do fall from these holes and create various paths.

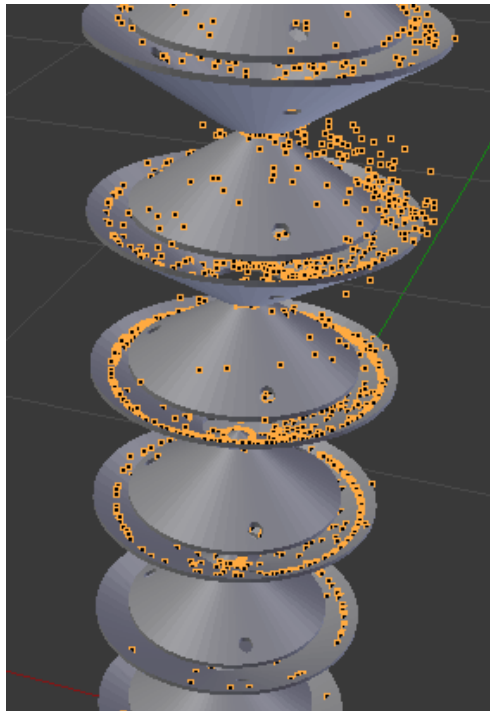


Figure 91: Flow visualization for conical design, oblique tilted view.

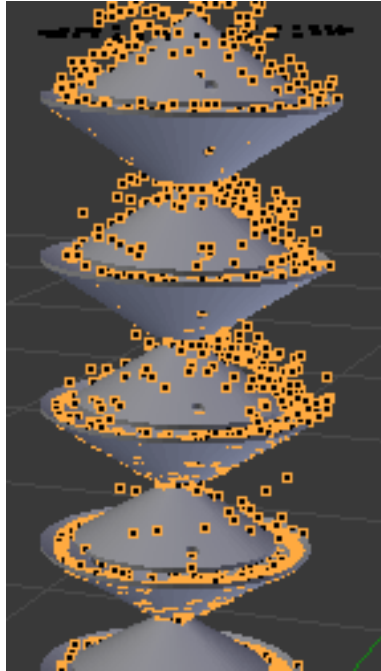


Figure 92: Flow visualization for conical design, oblique side view.

7.4.2 Disc and Donut Design

In the first design, the disc and donut, as shown in Figure 93 and Figure 94. The particles seem scattered and not showing the movement correctly compared to the experimental results. The particles bounce off the first surface and some particles do not interact correctly with other particles. This can be due to the number of interactions happening per time frame which can hinder the computational power that the software is made for. Thus, this flow was not a good indicator of the actual flow that was seen in experimental runs.

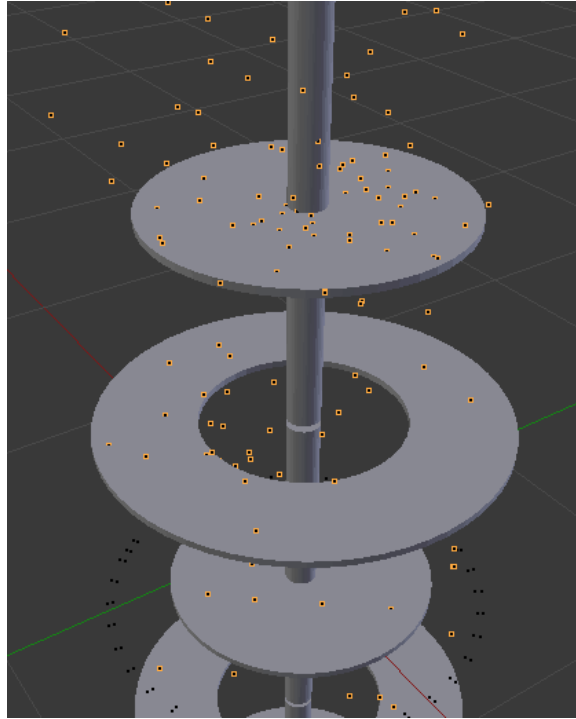


Figure 93: Flow visualization for disc and donut design, oblique tilted view.

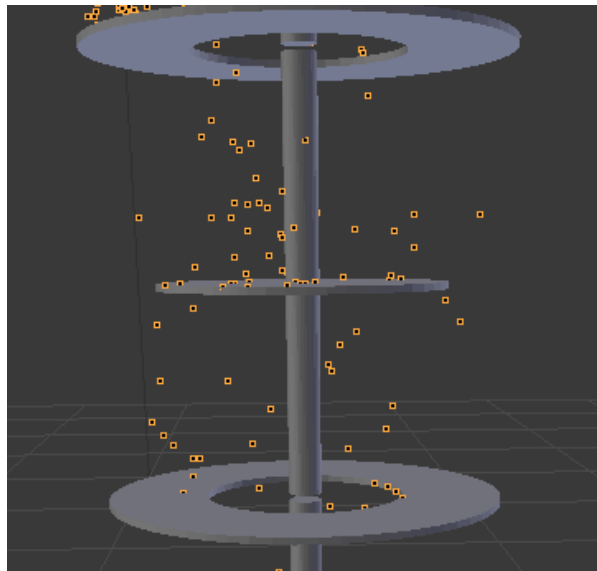


Figure 94: Flow visualization for disc and donut design, oblique side view.

7.4.3 Zigzag Design

For the zigzag design, discussed in chapter 5. The particles flow from one direction of the tube to another. As can be seen in Figure 95 and Figure 96, the flow seems to be following the same path of the particle flow one would see in the experimental runs. However, since Blender is not made for scientific purposes this is just a visualization and using this software in making decisions is not recommended.

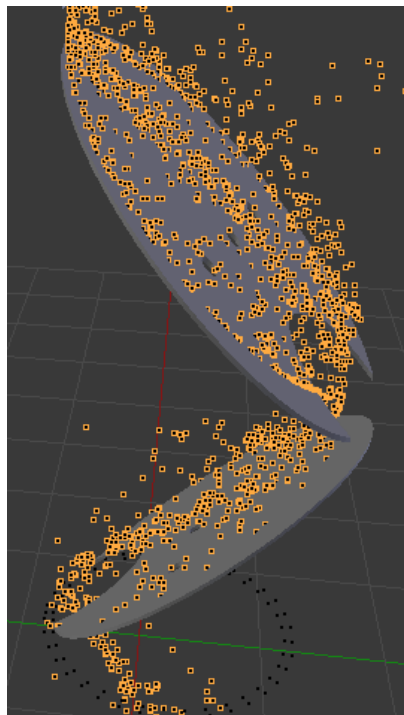


Figure 95: Flow visualization for zigzag design, oblique tilted view.

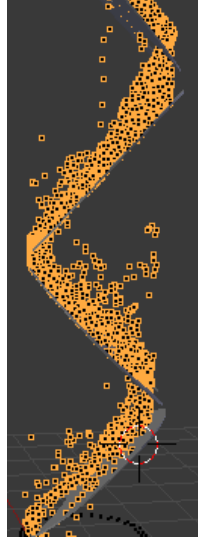


Figure 96: Flow visualization for zigzag design, oblique side view.

7.4.4 *Chevrans Design*

In the chevrons design, in Figure 97, the particle interaction looks very interesting on Blender, since the particles seem to follow the expected path. However, as seen in Figure 98 the particles at the top do not mix as much as particles at the bottom of the heat exchanger.

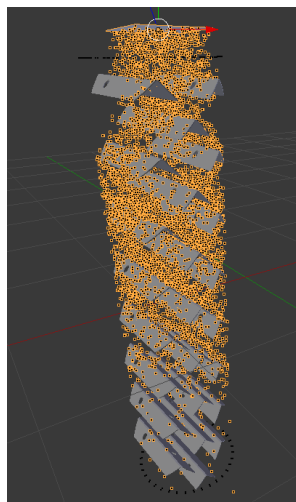


Figure 97: Flow visualization for chevrons design, oblique tilted view.

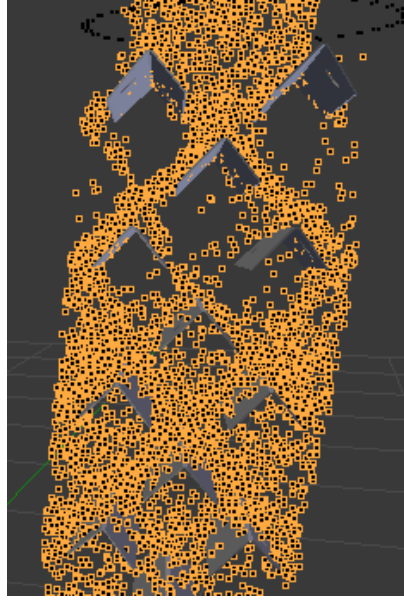


Figure 98: Flow visualization for chevrons design, oblique side view.

7.4.5 Conclusions

The simple or even simplistic Blender simulation program does generate particle flows that in some cases are at least qualitatively in agreement with experiment. Consequently, this program may be useful in preliminary investigations of particle flows in direct contact exchangers.

7.5 Experimental Observations of Particle Distribution

In the experimentation, several photographs were taken to show the distribution of the flow. However, because the particles are much dispersed in the heat exchanger, it was very challenging to show the distribution using still pictures. Before entering the heat exchanger, the particles enter the wye section, in this section the particles can be seen to be clearly forming streams as shown in Figure 99. Going further downstream to the heat exchanger, after the particles pass the distribution panel and pass the first stage of the disc and donut design, the particles become dispersed and very hard to see. As seen in Figure 100, the particles are barely visible. The red circles on the image show some particles that are visible in the image. The bigger circle, shows that some particles are being stuck in-between the perforated plate and the PVC tube. The smaller circle, shows that a concentration of particles; one can observe these concentrations in the darker region of the image. It appears that even the very preliminary internal designs tested so far can achieve adequately uniform particle distribution.

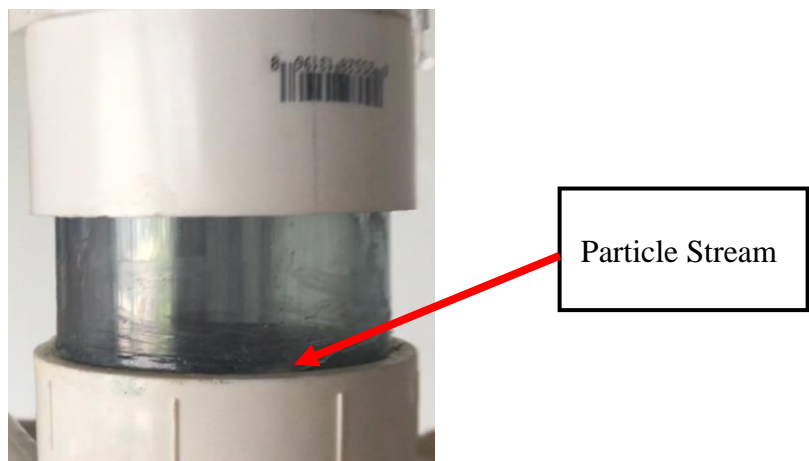


Figure 99: Uniform flow through the wye section, showing the individual particle streams that were made by the perforated plate.



Figure 100: Particles are distributed, thus difficult to observe using still pictures. The small red circle shows a group of particles (shown as a darker region of the heat exchanger). The larger red circle shows the particles that are trapped in between the perforated plate and the PVC tube.



Figure 101: Particle flow through the heat exchanger, particles can be seen dispersed and show a good distribution while falling.

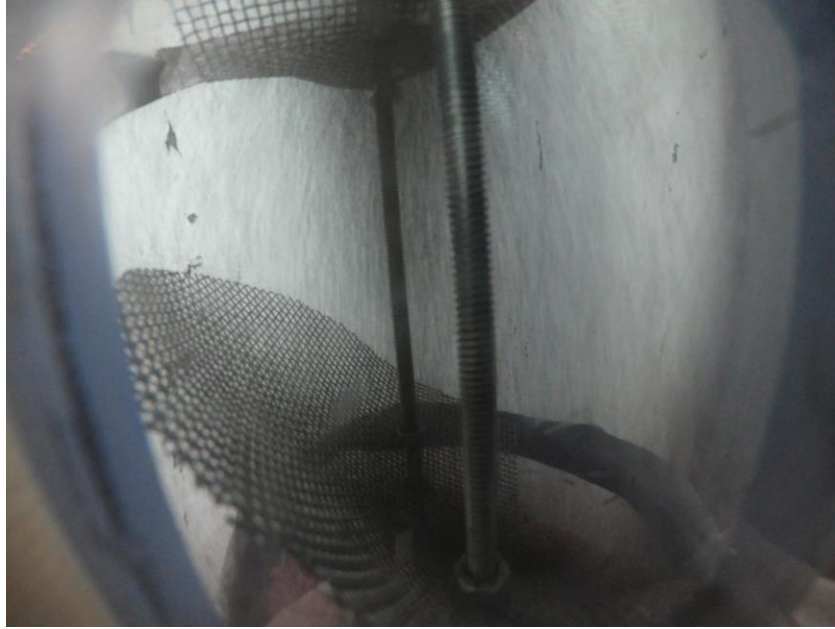


Figure 102: Another figure showing the good distribution of the particle flow in the heat exchanger.

7.6 Turbine Erosion

Previous research that was done can conclude that a turbine can tolerate dust loads in the range of 100 ppm, but 98% of the particles need to be less than 10 microns [36]. This research also concluded that particles smaller than 10 microns have a much less erosion rate compared to particles larger than 10 microns. However, previous research also mentions that this work was done on a small-scale turbine and that the effects of these small particulates in larger turbines might be reduced [36]. Other researchers have found that the erosion ratio of the turbine decreases by 75 percent when particles are smaller than 6 microns. In their research, their model simulated a turbine operation in a large utility gas plant that used coal [47]. The researchers have also found that particles less than 10 microns pass through filters and that more filtration and cleaning systems are needed for larger gas turbines. Consequently, it was concluded that erosion damage to turbine blades increase

with the increase of particle size and that it is confined to pressure surfaces of the turbine blade [48]. Furthermore, adding conical strainers would be effective in preventing any large particles from entering the turbine. The conical strainers, which are placed downstream of the compressor, has shown to be effective in practice at RTV demonstration. Also, the turbine being used should be resistant to some extent to very small particles since most of the literature studied investigated the erosion on a full system that includes the much more delicate compressor and the turbine.

7.7 Summary

In conclusion, separation was not seen throughout the various experiments conducted but a good distribution was seen using different designs. The heat exchanger designs chosen in this chapter were the disc and donut, conical, zigzag, and chevrons design. These designs were chosen as they are much more economic and easier to manufacture in the given time frame. Furthermore, these designs are also suitable for a cylindrical heat exchanger. The run was also conducted on Blender, to give us a rough idea how the particles will be distributed in the heat exchanger. Using Blender, I have also seen good distribution and consistency in the flow. However, further research needs to be done using PIV to analyze the flow distribution thoroughly, generate the velocity profile for the particles, and check for flow consistency at various levels. It is also recommended to use CFD for future research and validate that using the PIV analysis. Thus, by validating the CFD model, researchers would be able to simulate the particulate flow for a larger scale model. Moreover, in this chapter an EES model was developed to predict the velocity for particle entrainment at various pressures and temperatures for different particle sizes. This

model would be very useful in the design of the heat exchanger, especially for the design of the supply air outlet section of the heat exchanger.

CHAPTER 8. PARTICLE CONTROL

8.1 Introduction

To effectively be able to use particles as a medium for a solar tower system, a more durable valve needs to be used to control the flow. As discussed in chapter 6, the valve that was used in the experiment is shown in Figure 58. This valve is a PVC gate valve with a stainless-steel gate and rubber sealing. The valves that will be used in the large-scale solar tower will need to have a self-cleaning mechanism and some valves will require to withstand a high-pressure seal. Other requirements include that the valve has a low-pressure drop and can withstand high temperatures (up to 900°C). Furthermore, the valve needs to have low air leakage and the material used in the valve needs to be abrasive resistant. The objective of this chapter is to review the current candidates that can be used in a large-scale solar tower application and propose new designs that can be studied and tested for future research.

8.2 Type of Valves

8.2.1 Rotary Paddle Wheel

The rotary valve uses a series of flat blades that rotate to control the flow. As shown in Figure 103, the valve will rotate in one direction and by use of a motor the user can control the mass flow of the particles through the valve. However, this valve does not have a good pressure seal and will thus leak air as the blades are turning. Air leakage can be a great disadvantage for this type of valve as can be further explained in the appendix. Thus, some of these valves require multi stage air lock systems to be coupled with the valve [49].



Figure 103: Rotary paddle valve [50].

8.2.2 Butterfly Valve

The butterfly valve, shown in Figure 104, uses a central disc that rotates around a central rod to control the flow of the particles. The valve can be used as an on and off valve as well as a control valve by partially opening the valve. This valve is typically used in slurries and can be used for powders or particulates as well. The valve does have a disadvantage of having a pressure drop, especially when the valve is not fully open [51].

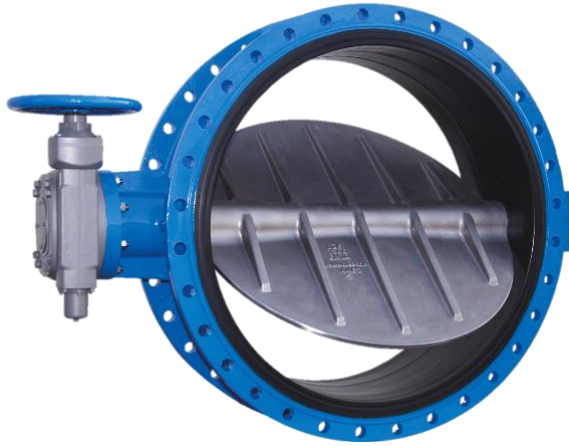


Figure 104: Butterfly valve [51].

8.2.3 *Gate Valve*

The gate valves are used for on and off operations but can be redesigned or configured to be used to regulate particulate flow. The gate valve consists of a steel knife gate that moves back and forth to open and close the valve. When using a gate valve with particulates or sand, one must consider a cleaning mechanism to ensure effective operation of the valve. Therefore, most of the gate valves used in powder or granular applications have a self-cleaning mechanism. As can be seen in Figure 105, the gate valve has a clearance so that the particles can be pushed in the clearance area and not damage the valve [52].



Figure 105: Gate valve with the self-cleaning mechanism [53].

8.2.4 *T-valve*

The T-valve, shown in Figure 106, is designed for heavy-duty use, such as slurries, heavy density materials, and abrasives. It can withstand high temperature and pressure (up to 3 bar) and can be used in a two-valve airlock system for optimal performance. The valve uses a T shaped steel plate that rotates to allow particulates pass through. The shape of the valve gives it the advantage for a self-cleaning mechanism that constantly allows the valve to operate effectively, this can be seen in detail in the appendix [54].



Figure 106: T-valve with a self-cleaning mechanism [54].

8.2.5 Pinch Valve

Pinch valves are used in slurries, sand and abrasive materials. However, they are not designed to with stand high temperature and pressure. Some new pinch valves can with stand relatively high pressures. They use a flexible material to basically pinch the flow and stop it, as shown in Figure 107 [55].

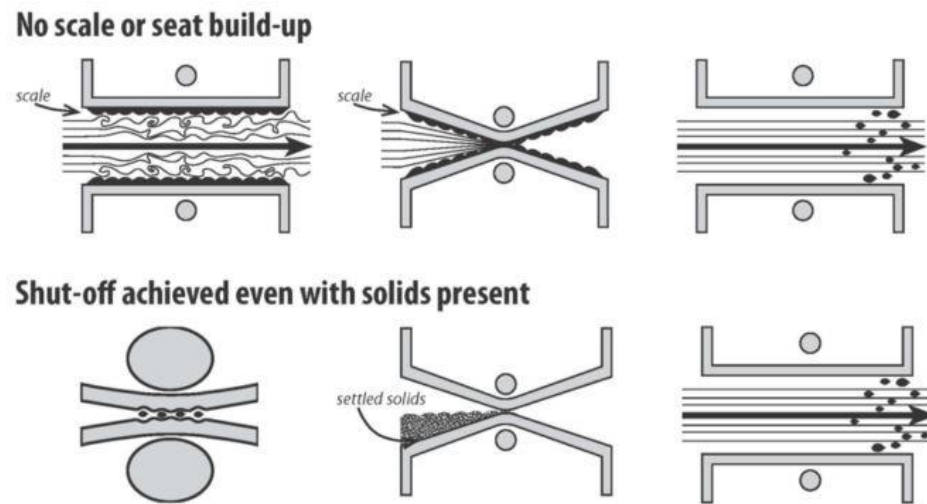


Figure 107: Schematic of pinch valve in operation [56].

8.3 Modified Valves

8.3.1 Rotating Pocket Valve

The valve acts as a pocket that constantly rotates counterclockwise. The idea here is to minimize any particles from getting stuck between the walls and the valve. But because the valve is rotating at a constant rate, it will clean itself. There might be a need to add a vacuum hole that will be used in case particles accumulate on top of the valve. Two perforated plates will also be installed upstream of the valve to regulate the flow, as shown in Figure 108.

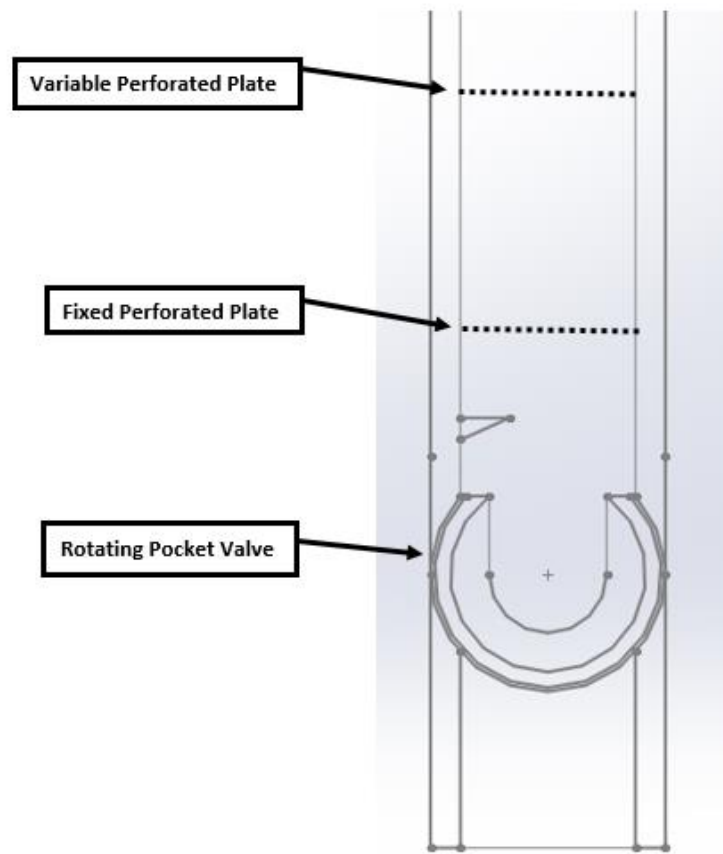


Figure 108: Rotating pocket valve conceptual design, side view.

8.3.2 *Rotated Diaphragm Valve*

The diaphragm valve in Figure 109, will be used in a 90-degree orientation and the angle of flow can be optimized to minimize any particulates getting stuck in the valve. The valve is used as a shut-off valve but might be designed to control the flow of the material [57].

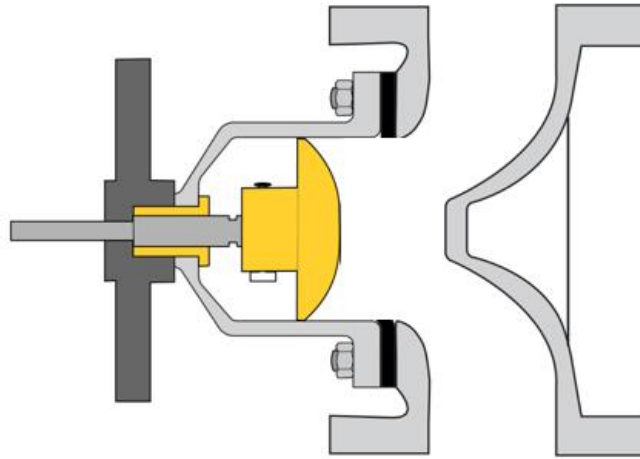


Figure 109: Rotated diaphragm valve [58].

8.3.3 *Particle Bridging to Control Flow*

Particle bridging, shown in Figure 110, can be used to control the flow of particulates by regulating the pressure and bed height. For a specific perforated plate, there is a specific bed height and pressure where bridging occurs. Thus, if there is a variable perforated plate that can be controlled it will help regulate the flow. The flow can also be regulated by regulating the pressure and bed height. Furthermore, when bridging occurs it shuts off the flow completely.

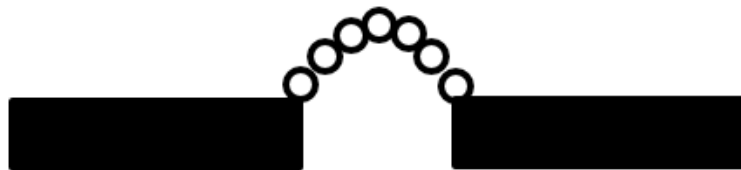


Figure 110: Particle bridging for particle flow control.

8.4 Particle control in a Solar Tower System

The system shown in Figure 111, shows a schematic of the solar tower system. The particle heating receiver (PHR) is located the top of the solar tower and it is where the light is concentrated in a small area by the heliostats on the ground to heat the particles. The particles then fall in a hot bin where they are stored temporarily. The hot bin has a valve at the bottom of the bin, labeled as valve 1. The bin is at atmospheric pressure; thus, the valve is not required to hold any pressure. Valve 1 connects the hot bin with the basic tank, which is just a tank to control the mass flow of the particles and ensuring the particle velocity to remain slow. Valve 1 can be a rotary paddle valve, a gate valve, a butterfly valve, or a T-valve, as discussed earlier. After the basic tank, the heat exchanger is placed and needs to maintain a pressure of 4 bars. Consequently, valve 2 and 3 need to hold pressure and airlock is recommended to minimize any air leakage or pressure losses.

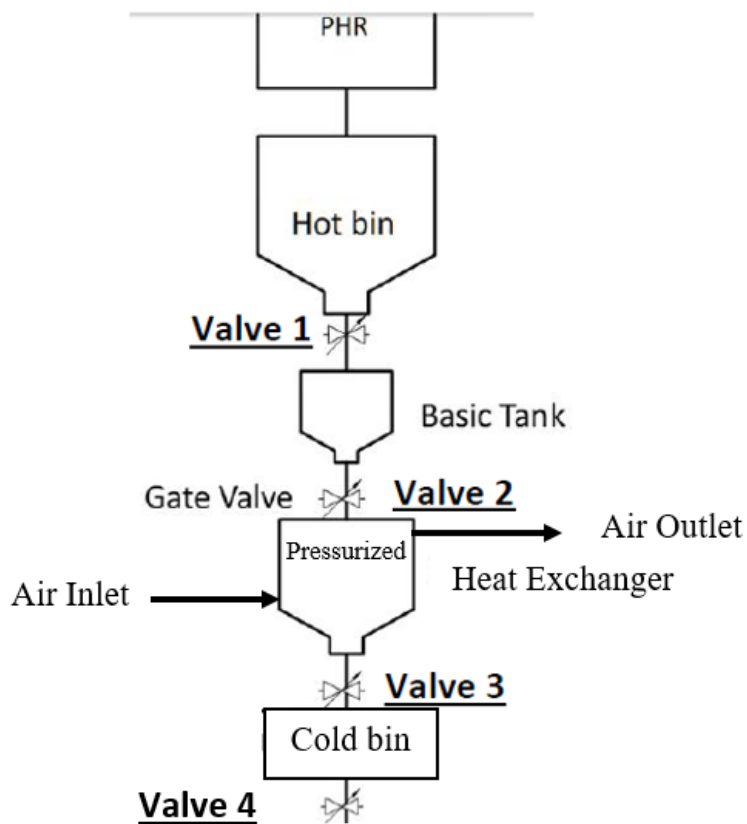


Figure 111: Schematic of solar tower system, showing all the valve locations.

Therefore, valve 2 and 3 are recommended to each have a two-valve airlock system, meaning that valve 2 will contain two valves and an airlock, and valve 3 will contain two valves and an airlock, as shown in the schematic of Figure 112. Valves 2 and 3 can be either a rotary paddle valve, a gate valve, or a T-valve. Valve 3 connects the heat exchanger to the cold bin that is not pressurized. The cold bin will have a valve at the bottom to also maintain control of the flow of particles throughout the system. Similar to valve 1, valve 4 which is located at the bottom of the cold bin does not need to hold any pressure and thus can be the same type of valve used for valve 1, which was either a rotary paddle valve, a gate valve, a butterfly valve, or a T-valve.

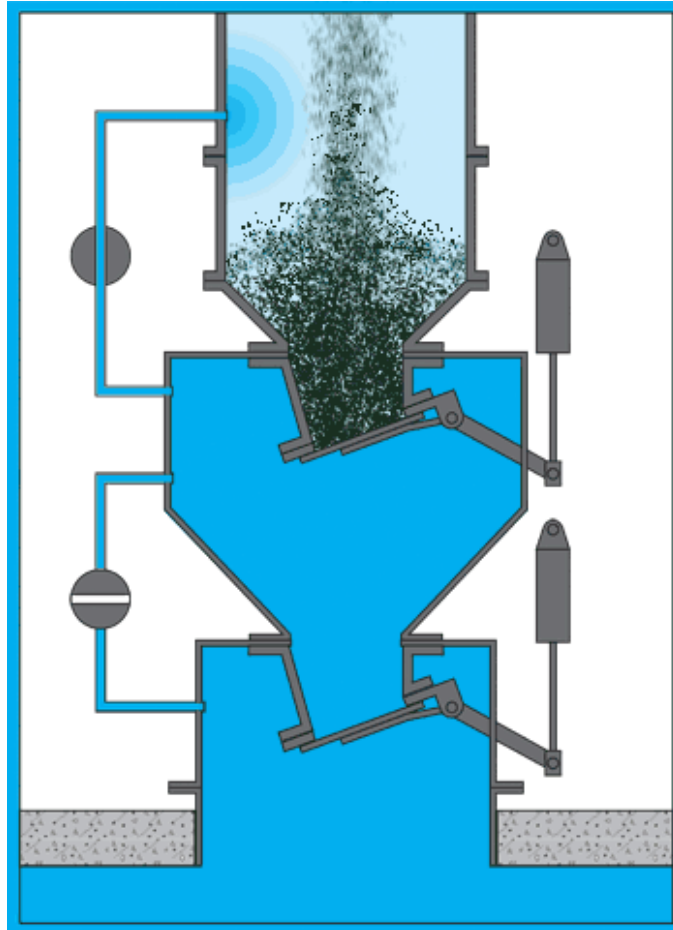


Figure 112: Schematic of valve airlock system [59].

8.5 T-Valve Airlock System

Due to the need for an airlock system that will be inserted both in the inlet to the heat exchanger and outlet from the heat exchanger, calculations were done for incorporating a T-valve with an airlock system that is shown in Figure 113. The objective of this calculation was to identify the number of cycles needed to know the size of the airlock that can be used in the system. Two materials were examined, Accucast ID50 and Cobalt, in the calculations that were done using the Engineering Equation Solver (EES) software.

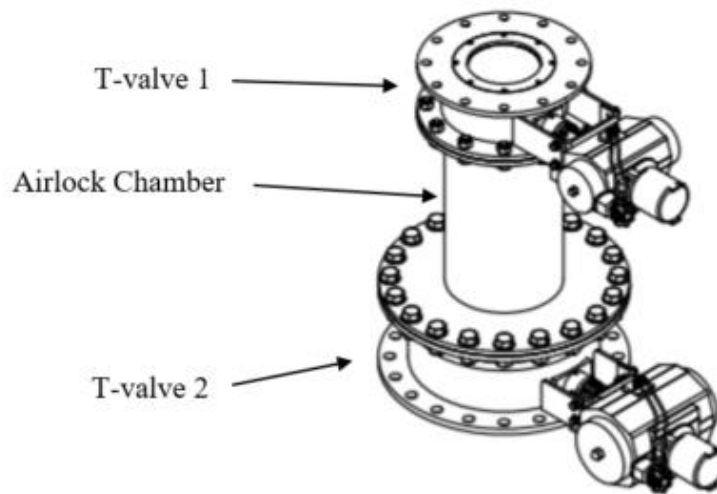


Figure 113: Schematic of the airlock chamber for the dual T-valve airlock system [60].

The mass flow rate for the flow was required to be 0.1 kg/s and the diameter of the valve was required to be 2 in. Thus, Figure 114 shows the height of the airlock chamber needed to satisfy the number of cycles per minute it would require maintaining the 0.1 kg/s mass flow rate. The EES file in the appendix further explains the calculations done for the sizing and cycling.

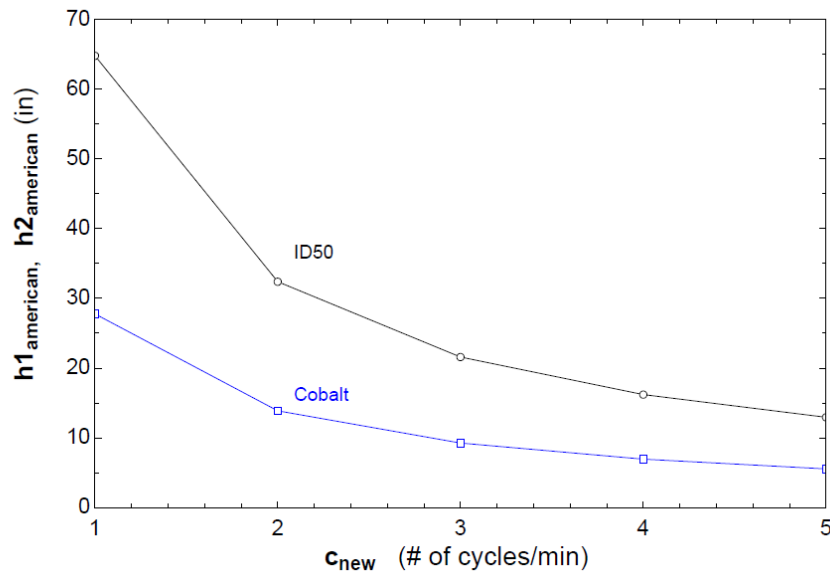


Figure 114: Graph showing the height of airlock chamber for both Accucast ID50 and Cobalt for the various number of cycles per minute.

8.6 Conclusion

In conclusion, it is recommended that the T-valve system to be used for the inlet and outlet of the heat exchanger. It is also recommended that at the inlet there would be a T-valve airlock system to minimize any air leakage and ensure that the valve's self-cleaning mechanism works. Furthermore, at the outlet of the heat exchanger, it is also recommended that there would be another T-valve airlock system to maintain the pressure in the heat exchanger. The design of the T-valve helped keep the valve clean and reduced any particles being trapped. The other advantage of the T-vale is that it can be modified to operate at higher temperature. Finally, the new valve designs proposed in this chapter should be further investigated as they might be good candidates for high temperature and pressure applications.

CHAPTER 9. CONCLUSION

9.1 Conclusions

A thorough literature review was done on the application and the types of direct contact heat exchangers that can be used in a solar tower. It has also been evident that particle technology is becoming increasingly popular in research for concentrated solar power applications. Furthermore, moving bed heat exchanger have shown to be a good candidate in lab scaled models but still further research needs to be done on larger models and applications.

First, the inlet flows were investigated and studied especially for fluidization. After conducting the experiment, it was found that the existing literature applies to our case and that the pressure drop calculations were accurate across each bed height. This is especially important for a simple open stand-pipe inlet. A stand pipe that is terminated by a perforated plate or a mesh is a feasible inlet, as can be seen in chapter 4.

Second, various internal configurations were studied for a direct contact solid to fluid heat exchanger. Several feasible designs were identified in the literature and were studied in detail. Four designs were selected based on simplicity and feasibility of the design. These designs were studied experimentally, in chapter 5, to confirm their flow characteristics.

Third, the particle inlet flows were investigated in chapter 6. Using the perforated plate with a gate valve has shown to be a very feasible design. This design, enabled a modular system, in which the internal parts of the heat exchanger can be exchanged easily. This design also allowed for ease of refilling the particulate column and allowed for change

in the perforated plate. The particle mass flow was investigated for various perforated plate type and sizes. It was concluded that the flow was steady and uniform through the inlet and that there was no gas bypass throughout these experiments. Fluidization and bridging was observed in the particulate column. This inlet design lead to another new and useful design that should be pursued in later work.

Fourth, the particle flow was studied in detail and observations were made in chapter 7. Particle fluidization was investigated, and the heights were identified for fluidization for various perforated plates. Furthermore, entrainment was calculated theoretically and measured experimentally. The entrainment calculations helped in controlling the flow and minimizing any particle carry over. The entrainment that occurred experimentally was found to be due to fluidization or bridging. Consequently, entrainment can be controlled if air velocity and particle bridging is controlled. Also, the air velocities were compared to the fraction of mass entrained. We concluded that as the air velocity increases the percentage of mass entrained increases. Moreover, the particle sizes were measured using a microscope and a microscopic slide ruler. This experiment was conducted to verify the theoretical calculations that were done earlier. Thus, the simple theoretical model proved to be effective in predicting particle entrainment in this case. Further, as the air velocity increases, the particle size entrained increases and the number of particles entrained increases. Then, the particle flow was simulated using Blender for the four designs identified in chapter 5. Then a flow visualization was conducted experimentally and confirmed that the flow is consistent, steady, and uniform throughout the particle fluid heat exchanger.

Finally, a literature survey was conducted on the current particle control technologies. Recommendations were given for specific valves that are currently available in industry. Also, new designs were constructed to meet the valve requirements for the solar tower application. These new concepts should be pursued for further research and testing. Sizing calculations were also done for an airlock system that can be placed in the solar tower application.

9.2 10 MW Solar Tower Plant

The system that will be studied for the scale up is located in Riyadh in Saudi Arabia. The project is part of the solar thermal research done in Kind Saud University and the main focus of this research is to study new advancements in solar towers. Currently as seen in Figure 115, the heliostats are installed and have been integrated to effectively concentrate the light on the central receiver in the tower. The central receiver referred to as the Particle Heating Receiver (PHR), can be seen in the figure, as the bright light on the tower. There are a lot of research and development being done on this system to decrease radiation and overall heat losses. The tower also contains the heat exchanger as well as the turbine. In Figure 116, there are pipes coming in and out of the tower, these are the pipes connecting the heat exchanger to the turbine. The turbine is located on the platform seen in the figure. Figure 115, does not show the platform since at the time of the photo the platform was not built. Moreover, there are still constant research and development being conducted on all subsystems of this solar tower. In the appendix, further details are given regarding the heat exchanger as well as the turbine used in the system.



Figure 115: Solar tower system in Saudi Arabia.

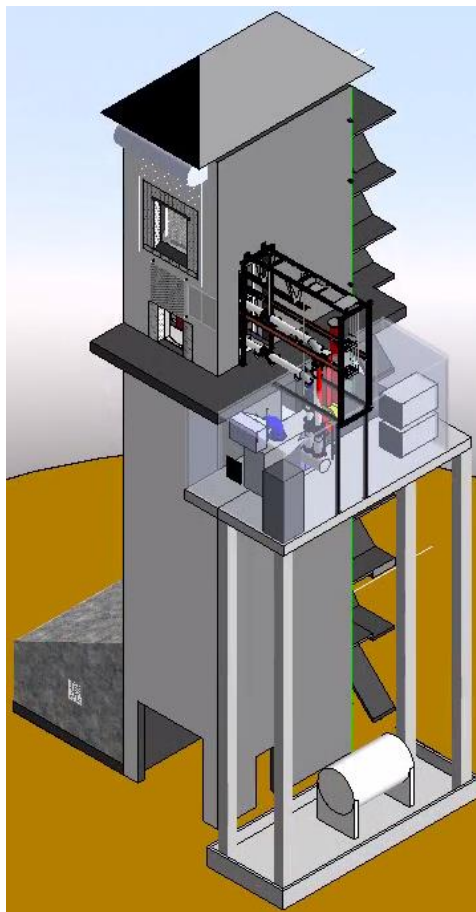


Figure 116: Schematic of the solar tower system that is currently installed.

The current heat exchanger in the system is an indirect contact heat exchanger between sand and air. However, this research can serve as first step to study a direct contact heat exchanger that will enable higher heat exchanger effectiveness and thus result in higher overall efficiency for the plant. Furthermore, this type of heat exchanger will reduce the cost of the scaled-up system, as there are no expensive metals used in the internal design of the heat exchanger which is the case in indirect contact heat exchangers. Furthermore, further research in this area may result in successfully scaling up the direct contact heat exchanger and testing it on a 100 KW Solar Tower system.

The direct contact moving bed heat exchanger is a much more cost-effective solution when compared with an indirect contact heat exchanger. This is due to the removal of the material between the solid and the fluid (air), typically made of expensive alloy metals. Furthermore, the size of the heat exchanger can be greatly reduced as there is direct interaction between the solids and the fluid. Thus, decreasing the size of the heat exchanger in volume and height and further reducing the price as well. Moreover, by pressurizing the heat exchanger, the heat is effectively extracted from the particles solids to the air flowing through the heat exchanger. Furthermore, Prosin has made a through cost analysis on sizing up solar tower power plants with various systems [61]. One type of size up and cost analysis that was conducted was on a direct contact heat exchanger that will be placed in a 10 MW solar tower power plant. The paper researched the manufactures of moving bed heat exchangers and found that Grenzebach had a lot of experience and expertise in this field [61]. Thus, the paper cited sources for the cost of this direct contact heat exchanger system, these ranged from \$143/kWth to \$215/kWth. His research also assumed worst case scenario and went with the most expensive option of \$215/kWth and that the target cost is

to reduce this cost to about \$54/kWth [61]. As part of further work a proposed design will be developed.

9.3 Summary

This thesis has studied and analyzed the particle entrainment, which plays an important role in solar thermal power plants. In a solar tower power plant that used particulates as the media, there is a possibility for particles to be entrained from the heat exchanger to the turbine. This is true if the solar tower system is using a direct contact heat exchanger. In the direct contact heat exchanger that transfers heat from the hot particulates to the gas, the gas needs to be mixed thoroughly throughout the heat exchanger to increase the heat exchanger effectiveness. However, since the heat exchanger is pressurized a set of valves need to be in place between the upper and lower bins connected to the heat exchanger. Thus, entrainment could occur if the velocity of the air inside the heat exchanger increases to a point where it can carry the particulate in the air, this is sometimes also referred to as particle carry over. Consequently, when analyzing this behavior, I have set limits for air velocities at various pressures to ensure that entrainment does not occur. We have done the calculation on various particle sizes to show the trend and for future research to predict whether entrainment would occur. Furthermore, I have found that during our experimental runs that the number of particles entrained overall was minimal at various pressures and did not exceed 9% of the total mass that went through the heat exchanger. We have observed that entrainment also occurs when the particulate column is blocked, meaning that bridging occurs. This sometimes occurs just before fluidization or due to some clogging in the flow. Fluidization in the particulate column also disrupts the flow and can cause entrainment. These were the main causes of entrainment that were observed

during the experiments runs. Moreover, another experiment was conducted by capping the particulate column to minimize air leakage and observing if entrainment occurs. The result was that minimal entrainment occurred when there was no bridging or fluidization in the particulate column.

We have also conducted a lot of research and tests in particle entry or inlet. This includes various designs for entry valves as well as researching various valves that can be utilized in particulate flow and are sustainable. The challenge with valves in the market is that solid particulates get stuck in valve system and thus affect the valve performance and life expectancy. Consequently, self-cleaning mechanisms were explored to check for solutions to these challenges. Three new valve ideas were proposed, these include a rotating pocket valve, a rotated diaphragm valve, and the use of variable perforated plates as well as birding to control the flow. Moreover, since these valves need also to hold pressure, an air lock system had to be calculated and designed to match the mass flow rate that is needed. For these calculations, I assumed that the self-cleaning T-valve mechanism will be used in an airlock system. Calculations were done to size the airlock system with two T-valves that can control particulate flow as well as maintain the pressure in the heat exchanger.

In this thesis, various direct contact heat exchanger designs were proposed. The design objective was to slow down the air velocity to minimize particle entrainment and increase the time it takes the particles to exchange heat with the air. Therefore, many designs were proposed and three were manufactured and assembled to be tested. The designs were evaluated based on the uniformity of distributing particulates throughout the heat exchanger. Other aspects of the interval design included a particle entry distributor. Since the particulate column is 2 in. (50.8 mm) in diameter and the heat exchanger diameter

is 6 in. (152.4 mm) the purpose of the distributor is to ensure that particles enter the heat exchanger in uniformity. Further, a perforated plate was also introduced at the inlet of the heat exchanger to reduce the falling speed of the particulates and control the mass flow. These two elements in the entry of the heat exchanger remained consistent throughout all the proposed and tested designs. Some designs were also chosen to be animated in Blender, to give a visualization of the flow and initial guess of how the particulates will flow through the heat exchanger.

Another important aspect that was researched in this thesis is the limitation of particle size for particulates flowing into a gas turbine. Since the direct contact heat exchanger is directly connected to the gas turbine, we need to minimize particle entry to the turbine. However, in between the connection for the heat exchanger, there are several methods to drain these particles from the air. First, we initially design the heat exchanger to limit entrainment to particle sizes of less than 100 microns. This would allow us to remove other smaller particles using pipe designs as well as strainers or witch hats. These pipe designs include widening the pipe area, to lower air velocities or increasing the vertical height so that gravity pulls down the particles back to the heat exchanger. This would enable us to catch almost all the particulates before the air enters the gas turbine. Finally, particle bridging was initially observed in the first setup of the experiment. Bridging can be studied much further and might be used to control particulate flow. This can be further studied, to get the relationship between the perforated rate opening area and size and the pressure. Bridging might also be affected by the temperature of media, so this is also another area that might need to be further investigated. This is not only useful for using bridging to control particulate flow but also to avoid it when not needed.

9.4 Future Work

This research builds a foundation for future studies in direct contact heat exchangers in solar tower plants. However, there are still a lot of research and experimentation that needs to be done to be able to produce a cost-effective and efficient system. For instance, particle control valves and techniques can still be researched in depth in finding better more cost effective and low maintenance valves. These valves would also need the requirement to have a self-cleaning mechanism as well as adaptable to automated control. Furthermore, particle visualization methods are still in progress, using a high-speed camera to get more accurate results on the speed of particulates flowing in various designs of the heat exchanger would greatly improve the design. Moreover, laser curtains can be used to measure the particle count as well as velocity for entrained particles. Laser curtains were used to measure bullet speeds in some aerospace research. This can also be done using Particle Image Velocimetry (PIV) analysis.

Other experimental work should include the manufacturing and assembly of the modified ball valve system and testing if the mechanism does clean itself as it was designed to. This can be an economic solution for particle control especially in smaller applications. Particle bridging has been observed and needs to be further studied, this includes changing perforated plate open area as well as alternating the diameters. Moreover, there is a possibility changing the medium material being used from Accucast ID50 to maybe sand. This would allow us to formulate a constant that can describe the bridging effect that occurs. Unfortunately, due to time constraints this has not been established here but should be further researched and studied. Also, PIV analysis should be conducted on more direct contact heat exchangers designs to give more details on the particle flow to enable better

heat transfer calculations. Finally, I have built my experiment in a modular design so that future research can be conducted on it as well as designing a structure around the experiment to attach an air conveyor to the side. This would allow future experiments to run for longer hours and will provide a continuous particulate flow in the heat exchanger.

References

- [1] IEA, "Energy Access Outlook," in "World Energy Outlook Special Report," 2017, Available:
https://www.iea.org/publications/freepublications/publication/WEO2017SpecialReport_EnergyAccessOutlook.pdf.
- [2] V. Sivaram, *Taming the Sun*.
- [3] (2016). *Solar Resource Maps and GIS Data for 200+ Countries*. Available:
solargis.com/products/maps-and-gis-data/free/download/world
- [4] J. Khan and M. H. Arsalan, "Solar power technologies for sustainable electricity generation - A review," (in English), *Renewable & Sustainable Energy Reviews*, vol. 55, pp. 414-425, Mar 2016.
- [5] M. Simpson, "Overview of State-of-the-Art Emerging Technologies for Solar Photovoltaics and Concentrating Solar Power (CSP)," ed: SlidePlayer, 2016.
- [6] "CSP Technologies ", ed: Udcink.org, 2015.
- [7] (2014). *Solar Tower*. Available: www.youtube.com/watch?v=W1U3rrMIIdmE
- [8] B. Frank. (2012) Suncatchers: A Solar Tech Rundown. Available:
www.kcet.org/shows/socal-connected/suncatchers-a-solar-tech-rundown
- [9] B. Langdon (2011) Solar Parabolic Dish CSP. Available:
mcensustainableenergy.pbworks.com/w/page/32178486/Solar%20Parabolic%20Dish%20CSP
- [10] S. Warerkar, S. Schmitz, J. Goettsche, B. Hoffschmidt, M. Reissel, and R. Tamme, "Air-Sand Heat Exchanger for High-Temperature Storage," (in English), *Journal of Solar Energy Engineering-Transactions of the Asme*, vol. 133, no. 2, May 2011.
- [11] H. L. Zhang *et al.*, "Particle circulation loops in solar energy capture and storage: Gas-solid flow and heat transfer considerations," (in English), *Applied Energy*, vol. 161, pp. 206-224, Jan 1 2016.
- [12] B. T. Gorman, N. G. Johnson, J. E. Miller, and E. B. Stechel, "Thermodynamic Investigation of Concentrating Solar Power with Thermochemical Storage," (in English), *Proceedings of the Asme 9th International Conference on Energy Sustainability, 2015, Vol 1*, 2016.

- [13] R. K. Shah and D. a. P. Sekulić, *Fundamentals of heat exchanger design*. Hoboken, NJ: John Wiley & Sons, 2003, pp. xxxii, 941 p.
- [14] C. G. Hill and T. W. Root, *Introduction to chemical engineering kinetics and reactor design*, Second edition. ed. Hoboken, New Jersey: Wiley, 2014, pp. xiii, 557 pages.
- [15] M. Lichtarowicz. (2013). *Chemical Reactors*. Available: <http://www.essentialchemicalindustry.org/processes/chemical-reactors.html>
- [16] A. Rahimi and A. Niksiar, "A general model for moving-bed reactors with multiple chemical reactions part I: Model formulation," (in English), *International Journal of Mineral Processing*, vol. 124, pp. 58-66, Nov 14 2013.
- [17] S. IlPark, "Performance analysis of a moving-bed heat exchanger in vertical pipes," (in English), *Energy*, vol. 21, no. 10, pp. 911-918, Oct 1996.
- [18] "DIRECT VERSUS INDIRECT HEATING TECHNOLOGY," S. T. SCIENCE, Ed., ed.
- [19] A. O. O. Denloye and J. S. M. Botterill, "Bed to surface heat transfer in a fluidized bed of large particles," *Powder Technology*, vol. 19, no. 2, pp. 197-203, 1978/03/01/ 1978.
- [20] R. Henda and D. J. Falcioni, "Modeling of heat transfer in a moving packed bed: Case of the preheater in nickel carbonyl process," (in English), *Journal of Applied Mechanics-Transactions of the Asme*, vol. 73, no. 1, pp. 47-53, Jan 2006.
- [21] K. J. Albrecht and C. K. Ho, "Heat Transfer Models of Moving Packed-Bed Particle-to-Sco2 Heat Exchangers," (in English), *Proceedings of the Asme 11th International Conference on Energy Sustainability*, 2017, 2017.
- [22] (2017). *Project Capability*. Available: <http://geaind.com/drying.php>
- [23] A. Soria-Verdugo, J. A. Almendros-Ibanez, U. Ruiz-Rivas, and D. Santana, "Exergy Optimization in a Steady Moving Bed Heat Exchanger," (in English), *Interdisciplinary Transport Phenomena: Fluid, Thermal, Biological, Materials, and Space Sciences*, vol. 1161, pp. 584-600, 2009.
- [24] "Moving Bed Catalytic Reactors," J. Johanson, Ed., ed, 2016.
- [25] H. J. Green, C. M. Leboeuf, and M. Bohn, "TECHNICAL AND ECONOMIC EVALUATION OF A SOLID-PARTICLE/AIR DIRECT-CONTACT HEAT EXCHANGER," Solar Energy Research Institute (SERI), U.S. Department of Energy 1986.
- [26] (2014). *Baffles*. Available: [3d-labs.com/HEAT%20EXCHANGER%20E-BOOK\(3D-](http://3d-labs.com/HEAT%20EXCHANGER%20E-BOOK(3D-)

LABS)/THERMAL%20DESIGN/Heat%20Exchanger%20Thermal%20Design%20E-Book-Baffle.html

- [27] M. Ohadi. (2017). *High Efficiency High Temperature Modular Power*. Available: arpa-e.energy.gov/sites/default/files/1b%20-%20Ohadi%20%28final%29.pdf
- [28] C. Savasadiya. (2015). *Heat Exchangers*. Available: www.slideshare.net/savasadiya55/heat-exchangers-52902228
- [29] M. J. Rhodes, *Introduction to particle technology*, 2nd ed. Chichester, England ; Hoboken, NJ: Wiley, 2008, pp. xxii, 450 p.
- [30] E. Michaelides, *Heat and mass transfer in particulate suspensions*. New York: Springer, 2012.
- [31] G. Rovero, M. Curti, and G. Cavaglià, "Optimization of Spouted Bed Scale-Up by Square-Based Multiple Unit Design," *Politecnico Di Torino*, 2012. K&E Srl
- [32] C. K. Ho *et al.*, "Characterization of Particle Flow in a Free-Falling Solar Particle Receiver," (in English), *Journal of Solar Energy Engineering-Transactions of the Asme*, vol. 139, no. 2, Apr 2017.
- [33] Noshok, "Dial Indicating Gauge Accuracy/Standard Dial Configuration," ed.
- [34] M. F. Gaureaux, "DIRECT CONTACT HEAT TRANSFER IN A BAFFLE-PLATE TOWER," Doctor of Philosophy, Chemical Engineering, Louisiana State University, Agricultural and Mechanical College, 1958.
- [35] W. Widmer, W. Zhou, and K. Grohmann, "Converting Citrus Waste to Ethanol and Other Co-Products," no. 99960, pp. 18-25, 2009.
- [36] R. R. Boericke, "Assessment of Gas Turbine Erosion by PFB Combustion Products," *U.S. Department of Energy*, 1980.
- [37] I. N. Christoph Ender, "A 100 year Search for the "ideal" Mass transfer DEvice," KOCH2013, Available: <http://www.koch-glitsch.com/Document%20Library/100-year-search-ideal-mass-transfer-device.pdf>.
- [38] J. M. Hruby, "A technical Feasibility Study of a Solid Particle Solar Central Receiver for High Temperature Applications," in "Solar Central Receiver Components Division," Sandia National Laboratories 1986.
- [39] C. K. Ho, "SunShot Concentrating Solar Power Research and Development: Project Narrative," Sandia National Labs 2015.
- [40] (2007). *Heat Exchanger Static Mixers*. Available: www.stamixco-usa.com/heat-exchanger

- [41] P. Rodriguez, "Selection of Materials for Heat Exchangers," *Indira Gandhi Center for Atomic Research*, 1997.
- [42] E. I. Nedderman. (2011). *GRANULAR MATERIALS, DISCHARGE THROUGH ORIFICES*. Available: www.thermopedia.com/content/821/
- [43] "Installation and Operation Manual," in *Brooks Sho-Rate Series*, B. Instrument, Ed., ed, 2016.
- [44] TSI, "VELOCICALC® MULTI-FUNCTION Ventilation Meter," ed, 2015.
- [45] D. Instruments. *Air Velocity Measurement*. Available: <http://www.dwyer-inst.com/Products/AirVelocityIntroduction.cfm>
- [46] OHAUS, "Ohaus GT 210 Manual," ed, 1987.
- [47] M. Mengutürk, D. Gunes, H. K. Mimaroglu, and E. F. Sverdrup, "Blade Boundary Layer Effect on Turbine Erosion and Deposition," *Journal of Fluids Engineering*, vol. 105, no. 3, pp. 270-276, 1983.
- [48] M. Mengütürk, D. Güneş, M. Erten, and E. F. Sverdrup, "Multistage Turbine Erosion," no. 79283, p. V001T01A104, 1986.
- [49] *Self-Cleaning Rotary Valve*. Available: <http://www.powderbulksolids.com/article/self-cleaning-rotary-valve>
- [50] "Rotary Valve for Metering, Feeding and Airlock Applications," A. Valves, Ed., ed, 2017.
- [51] (2015). *SERIES 120 BUTTERFLY VALVES*. Available: <http://www.townley.net/valves/series-120-butterfly-valve/>
- [52] S. Peters, "GATE VALVES AND KNIFE GATE VALVES: ISN'T ONE JUST SHARPER?," Available: <https://blog.craneengineering.net/gate-valves-and-knife-gate-valves-isnt-one-just-sharper>
- [53] (2016). *Quantum HDPV2 GATE*. Available: <http://www.vortexglobal.com/hdpv2/#tab-id-5>
- [54] (2017). *T Heavy Duty Valve*. Available: <https://gemcovalve.com/products/t-heavy-duty-valve/>
- [55] (2015). *PINCH VALVES*. Available: <http://www.townley.net/valves/pinch-valve-tubes/>
- [56] (2016). *Pinch Valve*. Available: <http://jindexvalves.com.au/wp-content/uploads/2016/10/WhyUsePinchValve.jpg>

- [57] (2014). *How to Select the Right Valve?* Available: <http://blog.indelac.com/bid/333897/How-to-Select-the-Right-Valve-with-Pros-Cons>
- [58] (2017). *Lined GEMÜ diaphragm valves.* Available: https://www.gemu-group.com/en_US/kundenloesungen/ausgekleidete-membranventile/
- [59] "National Conveyors," 2015.
- [60] "8" 'T' Airlock," ed: GEMCO VALVE, 2014.
- [61] T. PROSIN, "DEVELOPMENT OF A CST SYSTEM BASED ON A SOLID PARTICLE RECEIVER, OPTIMISED FOR COMMERCIALISATION IN THE AUSTRALIAN MARKET," Murdoch University, 2017.
- [62] R. C. Knott, "HIGH TEMPERATURE DURABILITY OF METALS FOR USE IN A PARTICLE HEATING RECEIVER FOR CONCENTRATED SOLAR POWER," Masters of Science, Mechanical Engineering, Georgia Insistute of Technology.
- [63] *Silicon Carbide, SiC Ceramic Properties.* Available: <http://accuratus.com/silicar.html>
- [64] *Aluminum Nitride, AlN Ceramic Properties.* Available: <http://accuratus.com/alumni.html>
- [65] *Boron Nitride, BN Ceramic Properties.* Available: <http://accuratus.com/boron.html>
- [66] *Types of Rotary Valve Air Leakage* Available: <http://www.egatevalves.co.uk/uses/air-leakage-comparison/>
- [67] *T Heavy Duty Valve.* Available: <https://gemcovalve.com/products/t-heavy-duty-valve/>
- [68] "Fabricated Temporary Cone, Basket & Plate Strainers," ed: KECKLEY COMPANY.

Appendix A: Accucast ID50-K Foundry properties

Average particle size: 0.283 mm

Chemical Composition of ID50-K Particles [62]:

Compound	Weight %
Al ₂ O ₃	75
SiO ₂	11
Fe ₂ O ₃	9
TiO ₂	3

Mineralogy of ID50-K Particles [62]:

Mullite	52%
Corundum	48%
Beta Cristobalite	0%
Amorphous	0%
Quartz Silica	0%

Thermo-physical Properties [62]:

Apparent Specific Gravity (ASG)	3.23
Grain Fineness Number (GFN)	40
Loose Bed Density (lbs/ft ³)	113
Packed Bed Density (lbs/ft ³)	125
Thermal Expansion (%LC)	0.708
Coefficient of Expansion (1e ⁻⁶ in/in-°C)	6.62
Thermal Conductivity (W/m-°C)	0.70
Heat Capacity (Cal/g-°C)	0.291
Thermal Diffusivity (cm ² /s)	0.0029
Heat Diffusivity 10 ⁶ (W ² s)/(m ⁴ -°C ²)	1.708

Appendix B: Particle Materials

Silicon Carbide

Silicon Carbide has a lot of good mechanical properties and it is used in high performance applications such as ceramics, refractories, and abrasives. It is also the only chemical compound that is made out of silicon and carbon [63].

Table B1: Silicon Carbide material properties [63].

Mechanical	SI/Metric (Imperial)	SI/Metric	(Imperial)
Density	gm/cc (lb/ft ³)	3.1	(193.5)
Porosity	% (%)	0	(0)
Color	—	black	—
Flexural Strength	MPa (lb/in ² x10 ³)	550	(80)
Elastic Modulus	GPa (lb/in ² x10 ⁶)	410	(59.5)
Shear Modulus	GPa (lb/in ² x10 ⁶)	—	—
Bulk Modulus	GPa (lb/in ² x10 ⁶)	—	—
Poisson's Ratio	—	0.14	(0.14)
Compressive Strength	MPa (lb/in ² x10 ³)	3900	(566)
Hardness	Kg/mm ²	2800	—
Fracture Toughness K _{IC}	MPa•m ^{1/2}	4.6	—
Maximum Use Temperature (no load)	°C (°F)	1650	(3000)
Thermal			
Thermal Conductivity	W/m•°K (BTU•in/ft ² •hr•°F)	120	(830)
Coefficient of Thermal Expansion	10 ⁻⁶ /°C (10 ⁻⁶ /°F)	4.0	(2.2)
Specific Heat	J/Kg•°K (Btu/lb•°F)	750	(0.18)
Electrical			
Dielectric Strength	ac-kv/mm (volts/mil)	—	semiconductor
Dielectric Constant	—	—	—
Dissipation Factor	—	—	—
Loss Tangent	—	—	—
Volume Resistivity	ohm•cm	10 ² –10 ⁹	dopant dependent

Aluminum Nitride

Aluminum Nitride is a relatively new material in ceramics. It has a high thermal conductivity and low coefficient of thermal expansion. It is also non-reactive and has good dielectric properties [64].

Table B2: Aluminum Nitride material properties [64].

Mechanical	Units of Measure	SI/Metric	(Imperial)
Density	gm/cc (lb/ft ³)	3.26	(203.5)
Porosity	% (%)	0	(0)
Color	—	gray	—
Flexural Strength	MPa (lb/in ² ×10 ³)	320	(46.4)
Elastic Modulus	GPa (lb/in ² ×10 ⁶)	330	(47.8)
Shear Modulus	GPa (lb/in ² ×10 ⁶)	—	—
Bulk Modulus	GPa (lb/in ² ×10 ⁶)	—	—
Poisson's Ratio	—	0.24	(0.24)
Compressive Strength	MPa (lb/in ² ×10 ³)	2100	(304.5)
Hardness	Kg/mm ²	1100	—
Fracture Toughness K _{IC}	MPa•m ^{1/2}	2.6	—
Maximum Use Temperature (no load)	°C (°F)	—	—
Thermal			
Thermal Conductivity	W/m•°K (BTU•in/ft ² •hr•°F)	140–180	(970–1250)
Coefficient of Thermal Expansion	10 ⁻⁶ /°C (10 ⁻⁶ /°F)	4.5	(2.5)
Specific Heat	J/Kg•°K (Btu/lb•°F)	740	(0.18)
Electrical			
Dielectric Strength	ac-kv/mm (volts/mil)	17	(425)
Dielectric Constant	@ 1 MHz	9	(9)
Dissipation Factor	@ 1 MHz	0.0003	(0.0003)
Loss Tangent	@ 1 MHz	—	—
Volume Resistivity	ohm•cm	>10 ¹⁴	—

Boron Nitride

Boron Nitride has good mechanical and electrical properties. It also has a high thermal conductivity and a low coefficient of thermal expansion. It is also able to withstand thermal shock and is a non-toxic material. Finally, it is nonabrasive and can be easily machined [65].

Table B3: Boron Nitride material properties [65].

	Units of Measure	Orientation to Pressing Direction			
Mechanical	SI/Metric (Imperial)	Parallel		Perpendicular	
Density	gm/cc (lb/ft ³)	1.9	(120)	1.9	(120)
Porosity	% (%)	2.8	2.8	2.8	2.8
Color	—	white	white	white	white
Flexural Strength	MPa (lb/in ² x10 ³)	75.8	(11.0)	113	(16.4)
Elastic Modulus	GPa (lb/in ² x10 ⁶)	46.9	(6.8)	73.8	(10.7)
Shear Modulus	GPa (lb/in ² x10 ⁶)	—	—	—	—
Bulk Modulus	GPa (lb/in ² x10 ⁶)	—	—	—	—
Poisson's Ratio	—	—	—	—	—
Compressive Strength	MPa (lb/in ² x10 ³)	143	(20.8)	186	(27.0)
Hardness	Kg/mm ²	15-24	—	15-24	—
Fracture Toughness K _{IC}	MPa•m ^{3/2}	—	—	—	—
Maximum Use Temperature (inert atm)	°C (°F)	1800	(3250)	—	—
Thermal					
Thermal Conductivity	W/m•°K (BTU•in/ft ² •hr•°F)	30	(205)	33	(225)
Coefficient of Thermal Expansion	10 ⁻⁶ /°C (10 ⁻⁶ /°F)	11.9	(6.6)	3.1	(1.7)
Specific Heat	J/Kg•°K (Btu/lb•°F)	1610	(.38)	—	—
Electrical					
Dielectric Strength	ac-kv/mm (volts/mil)	95	(2400)	79	(2000)
Dielectric Constant	@ 8.8 GHz	4.6	—	4.2	—
Dissipation Factor	@ 8.8 GHz	0.0017	—	0.0005	—
Loss Tangent	—	—	—	—	—
Volume Resistivity	ohm•cm	>10 ¹⁴	—	>10 ¹⁵	—

Appendix C: Types of Rotary Valve Air Leakage

There are two main types of leakage in rotary valves carry-over leakage and clearance leakage. The carry-over leakage is when the compressed air goes into an empty pocket in as its making its way up in the valve. The clearance leakage is when air leaks between the housing and the moving rotor.

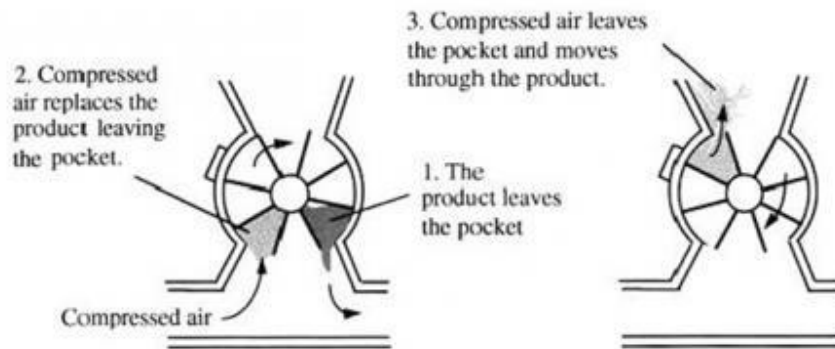


Figure C1: Rotary valve carry-over leakage [66].

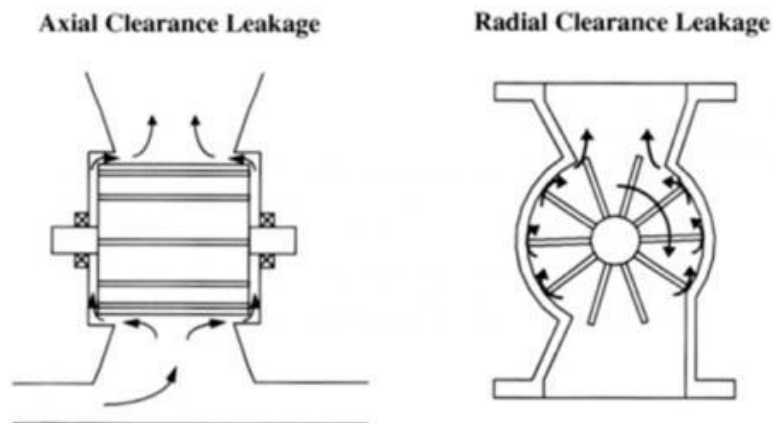


Figure C2: Rotary valve clearance leakage [66].

[66]

Appendix D: T-Valve

The Type T-valve is designed for heavy-duty service. It is typically used for slurries, abrasives, and heavy density materials. The T-valve is available in cast stainless steel, cast iron as standard and can be fabricated from any alloy that can be welded, with the full range of sanitary finishes. Options include high temperature or pressure (3 bar) designs, clean in place spray balls or nozzles and custom adapters or mountings.

Drawings:

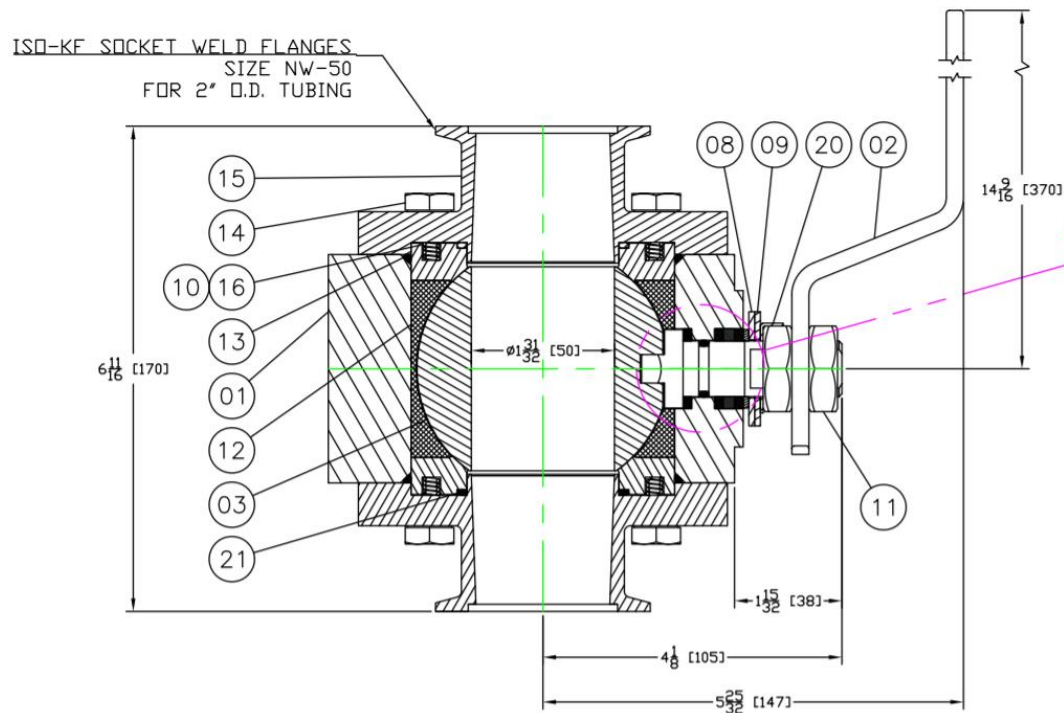


Figure D1: Side section view of T-valve [67].

Details:

- Valve body in 316L Stainless Steel.
- Connections Tri Clamp standard or ANSI flanges.
- Seat ring and ball segment are 316L hard coated to RC60.
- High temperature Graphite packing.
- Operated by a manual lever.

Appendix E: T-Valve Airlock System

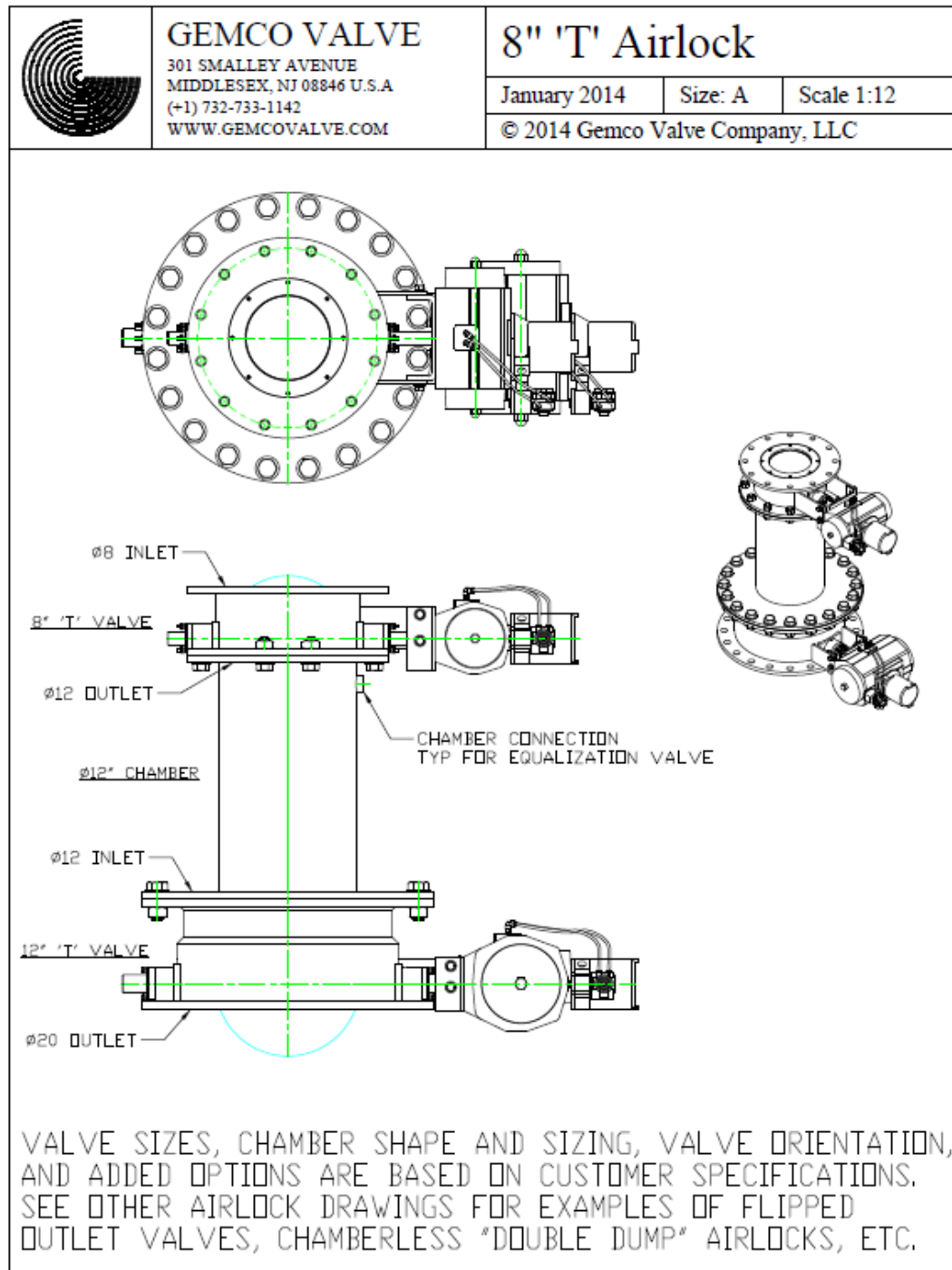


Figure E1: Gemco T-valve airlock system [67].

Appendix F: Airlock Cycling EES Calculations

This EES file is a calculation of the size of the airlock system needed for various cycle loads. The airlock can vary in height depending on how many cycles that the system will run. For this application, the number of cycles was minimized, as the mass flow required is low.

```
m_dot1=0.1 [kg/s]
v_dot1=m_dot1/den1
den1=1800 [kg/m^3]
r1=0.0254 [m]

h1=v_dot1/(3.14*(r1^2)*c)

c_new=c*60

m_dot2=0.1 [kg/s]
v_dot2=m_dot2/den2
den2=4200 [kg/m^3]
r2=0.0254 [m]

h2=v_dot2/(3.14*(r2^2)*c)

h1_american=h1*39.37 [in]
h2_american=h2*39.37 [in]
```

$$\dot{m}_{\text{dot1}} = 0.1 \text{ [kg/s]}$$

$$\dot{V}_{\text{dot1}} = \frac{\dot{m}_{\text{dot1}}}{\text{den1}}$$

$$\text{den1} = 1800 \text{ [kg/m}^3\text{]}$$

$$r1 = 0.0254 \text{ [m]}$$

$$h1 = \frac{\dot{V}_{\text{dot1}}}{3.14 \cdot r1^2 \cdot c}$$

$$c_{\text{new}} = c \cdot 60$$

$$\dot{m}_{\text{dot2}} = 0.1 \text{ [kg/s]}$$

$$\dot{V}_{\text{dot2}} = \frac{\dot{m}_{\text{dot2}}}{\text{den2}}$$

$$\text{den2} = 4200 \text{ [kg/m}^3\text{]}$$

$$r2 = 0.0254 \text{ [m]}$$

$$h2 = \frac{\dot{V}_{\text{dot2}}}{3.14 \cdot r2^2 \cdot c}$$

$$h1_{\text{american}} = h1 \cdot 39.37 \text{ [in]}$$

$$h2_{\text{american}} = h2 \cdot 39.37 \text{ [in]}$$

Solution:

$c = 0.08333$
 $\text{den1} = 1800 \text{ [kg/m}^3\text{]}$
 $h1 = 0.3291$
 $h2 = 0.141$
 $\dot{m}_{\text{dot1}} = 0.1 \text{ [kg/s]}$
 $r1 = 0.0254 \text{ [m]}$
 $\dot{v}_{\text{dot1}} = 0.00005556$

$c_{\text{new}} = 5$
 $\text{den2} = 4200 \text{ [kg/m}^3\text{]}$
 $h1_{\text{american}} = 12.96$
 $h2_{\text{american}} = 5.553$
 $\dot{m}_{\text{dot2}} = 0.1 \text{ [kg/s]}$
 $r2 = 0.0254 \text{ [m]}$
 $\dot{v}_{\text{dot2}} = 0.00002381$

No unit problems were detected.

Parametric Table: Table 1

	c	c_{new}	h1_{american}	h2_{american}
Run 1	0.01667	1	64.78	27.76
Run 2	0.03333	2	32.39	13.88
Run 3	0.05	3	21.59	9.254
Run 4	0.06667	4	16.2	6.941
Run 5	0.08333	5	12.96	5.553

Appendix G: Strainer

The strainer will help capture any particles entrained from the direct contact heat exchanger. This will be placed upstream the heat exchanger to capture any particles that were entrained before the air goes to the turbine. Furthermore, the strainer will be accessible so that the particles captured in it can be removed, to maintain minimal pressure drops.



Figure G1: Cone shaped strainer [68].

Table G1: Strainer size specifications [68].

Size		A				B		C	
		150 – 300 lb. (std)		600 lb.		All Flange Ratings		All Flange Ratings	
in	mm	in	mm	in	mm	in	mm	in	mm
1-1/2	40	3-1/4	83	3-5/8	92	1-1/4	32	3/4	19
2	50	4	102	4-1/4	108	1-3/4	44	1	25
2-1/2	65	4-3/4	121	5	127	2-1/4	57	1-1/4	32
3	80	5-1/4	133	5-3/4	146	2-3/4	70	1-1/2	38
4	100	6-3/4	171	7-1/2	191	3-3/4	95	2	51
6	150	8-5/8	219	10-3/8	264	5-3/8	137	3	76
8	200	10-7/8	276	12-1/2	318	7-3/8	187	4	102
10	250	13-1/4	337	15-5/8	397	9-3/8	238	5	127
12	300	16	406	17-7/8	454	11	279	6	152
14	350	17-3/8	441	19	483	12-1/4	311	7	178
16	400	20-1/8	511	21-7/8	556	14	356	8	203
18	450	21-1/4	540	23-3/4	603	15-3/4	400	9	229
20	500	23-1/2	597	26-5/8	676	17-1/2	445	10	254
24	600	27-7/8	708	30-7/8	784	21-1/4	540	12	305

Size		L 1/4" PERFORATED 3/16" CENTERS % OPEN AREA COMPARED TO CROSS SECTION SCHEDULE 40 PIPE											
		Cones						Baskets					
		100%		150% (std)		200%		100%		150% (std)		200%	
in	mm	in	mm	in	mm	in	mm	in	mm	in	mm	in	mm
1-1/2	40	3-3/16	81	4	102	5	127	2-3/4	70	2-7/8	73	3	76
2	50	3-1/2	89	6	152	8	203	3	76	3-1/2	89	4	102
2-1/2	65	4-1/16	103	6-1/4	159	8	203	3-3/16	81	3-7/8	98	4-1/2	114
3	80	4-1/4	108	6-3/4	171	9	229	3-1/2	89	3-7/8	98	5-1/2	140
4	100	5	127	10	254	12	305	4	102	5	127	7	178
6	150	7	178	13	330	18	457	6	152	7-3/4	197	11	279
8	200	8-3/16	208	17	432	23	584	6-1/8	156	9-3/4	248	14	356
10	250	12	305	22	559	28	711	7-1/2	191	12-3/8	314	18	457
12	300	13	330	26	660	34	864	9	229	14-3/4	375	20	508
14	350	15	381	27	686	36	914	10	254	15-7/8	403	21	533
16	400	17	432	30	762	40	1016	10	254	18-3/8	467	23	584
18	450	19	483	35	889	46	1168	12	305	20-7/8	530	27	686
20	500	21	533	39	991	51	1295	14	356	23-1/2	597	31	787
24	600	25	635	45	1143	61	1549	16	406	28-3/8	721	37	940

Appendix H: RTV Solar Tower System Components



Figure H1: RTV site in Riyadh, Saudi Arabia.

100 kW turbine with diesel combustion cycle and an air compression ratio of 1:4.5. It is capable of operating in hybrid and full diesel states.



Figure H2: 100kW turbine that used in the RTV site.

Indirect contact heat exchanger has internal cross tubes modules, air enters from the bottom and exits from the top, particles fall top to bottom. It also has a small hot bin on the top and a slide gate valve on the bottom. It is constructed out of 309 stainless steel.

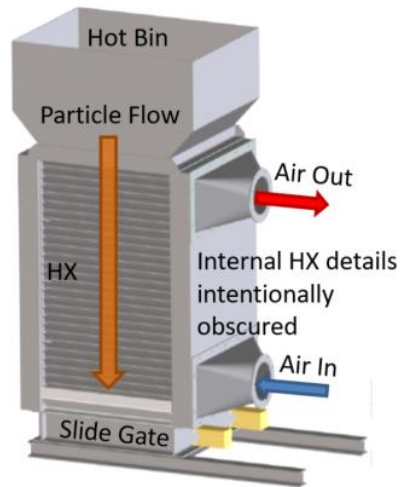


Figure H3: Schematic of the indirect heat exchanger at the RTV site.

Appendix I: Entrainment Calculations in EES

```

nu_air=kinematicviscosity(Air,T=T_out,P=P_hx)
mu_air=nu_air*rho_air
rho_air=density(Air,T=T_out,P=P_hx)
rho_p= 3300 [kg/m^3]
g = 9.81 [m/s^2]

```

$$X=(4/3)*((d_p^3)*rho_air*(rho_p-rho_air)*g)/(mu_air^2)$$

$$X=Cd*(Re^2)$$

$$Cd=0.5$$

$$Re=rho_air*d_p*(-U_T)/mu_air$$

$$U_air=0.00001 \text{ [m/s]}$$

$$U_rel=U_air+U_T$$

$$\nu_{air} = \text{KinematicViscosity} (\text{Air} , T = T_{out} , P = P_{hx})$$

$$\mu_{air} = \nu_{air} \cdot \rho_{air}$$

$$\rho_{air} = \rho (\text{Air} , T = T_{out} , P = P_{hx})$$

$$\rho_p = 3300 \text{ [kg/m}^3\text{]}$$

$$g = 9.81 \text{ [m/s}^2\text{]}$$

$$X = 4 / 3 \cdot \frac{d_p^3 \cdot \rho_{air} \cdot (\rho_p - \rho_{air}) \cdot g}{\mu_{air}^2}$$

$$X = Cd \cdot Re^2$$

$$Cd = 0.5$$

$$Re = \rho_{air} \cdot d_p \cdot \frac{-U_T}{\mu_{air}}$$

$$U_{air} = 0.00001 \text{ [m/s]}$$

$$U_{rel} = U_{air} + U_T$$

Parametric Table: Table 5

	P_{hx} [kPa]	d_p [m]	T_{out} [C]	U_{rel} [m/s]
Run 1	101.6	0.0001	25	-2.696
Run 2	101.6	0.0001	400	-4.052
Run 3	101.6	0.0001	800	-5.116
Run 4	101.6	0.0001	1200	-5.994
Run 5	200	0.0003	25	-3.328
Run 6	200	0.0003	400	-5.001
Run 7	200	0.0003	800	-6.315
Run 8	200	0.0003	1200	-7.399
Run 9	300	0.0005	25	-3.507
Run 10	300	0.0005	400	-5.271
Run 11	300	0.0005	800	-6.656
Run 12	300	0.0005	1200	-7.799
Run 13	400	0.001	25	-4.295
Run 14	400	0.001	400	-6.456
Run 15	400	0.001	800	-8.152
Run 16	400	0.001	1200	-9.552

Appendix J: Uncertainty Analysis

Opening Area 40%, Large Diameter, and Pressure 0 bars:

N: number of data points; DF: number degrees; SSD: Sum of Squared Differences; kc: Coverage Factor

Excel Calculation for U_A and U_C:

pressure	Time (s)	Vol flow (cm ³ /s)	Mass Flow (kg/s)	Squared Difference
	0 bar		N	9
			DF	8
	2.03	99.84	0.33	7.3E-04
	2.15	94.27	0.31	7.3E-05
	2.28	88.89	0.29	8.4E-05
	2.18	92.97	0.31	1.8E-05
	2.18	92.97	0.31	1.8E-05
	2.3	88.12	0.29	1.4E-04
	2.19	92.55	0.31	8.2E-06
	2.3	88.12	0.29	1.4E-04
	2.32	87.36	0.29	2.0E-04
	Avg. Vol. flow	91.68		
Avg. time	2.21	Average Mass Flow	0.30	
	Avg. Vel. (m/s)	0.05		
			SSD^2	1.76E-04
			kc	2.31
			U_A	1.02E-02
			U_B EES	1.36E-03
			U_C	1.03E-02

EES Calculation for U_B:

Unit Settings: SI K kPa kJ mass deg

Variable±Uncertainty	Partial derivative	% of uncertainty
M = 0.302±0.001364 [kg/s]		
T = 2.214±0.01 [s]	$\partial M / \partial T = -0.1364$	100.00 %
Vol = 0.0002027±1.000E-09 [m ³]	$\partial M / \partial Vol = 1490$	0.00 %

No unit problems were detected.

Opening Area 40%, Large Diameter, and Pressure 0.5 bars:

N: number of data points; DF: number degrees; SSD: Sum of Squared Differences; kc: Coverage Factor

Excel Calculation for U_A and U_C:

	Time (s)	Vol flow (cm ³ /s)	Mass Flow (kg/s)		
pressure	0.5 bar			N	5
				DF	4
	4.26	47.58	0.16		4.3E-05
	5.06	40.06	0.13		3.3E-04
	4.41	45.96	0.15		1.4E-06
	4.22	48.03	0.16		6.4E-05
	4.37	46.38	0.15		6.6E-06
Fluidization**	No Data Points				
	No Data Points				
	No Data Points				
	No Data Points				
	Avg. Vol. flow	45.60			
Avg. time	4.46				
		Average Mass Flow	0.15		
	Avg. Vel. (m/s)	0.02		SSD^2	1.12E-04
				kc	2.78
				U_A	1.32E-02
				U_B EES	3.36E-04
				U_C	1.32E-02

EES Calculation for U_B:

Unit Settings: SI K kPa kJ mass deg

Variable±Uncertainty	Partial derivative	% of uncertainty
M = 0.1498±0.0003356 [kg/s]		
T = 4.464±0.01 [s]	$\partial M / \partial T = -0.03356$	100.00 %
Vol = 0.0002027±1.000E-09 [m ³]	$\partial M / \partial Vol = 739.2$	0.00 %

No unit problems were detected.

**Please note that no data points were taken when fluidization occurred.

Opening Area 40%, Large Diameter, and Pressure 1 bars:

N: number of data points; DF: number degrees; SSD: Sum of Squared Differences; kc: Coverage Factor

Excel Calculation for U_A and U_C:

	Time (s)	Vol flow (cm ³ /s)	Mass Flow (kg/s)		
pressure	1 bar			N	5
				DF	4
	5.03	40.29	0.13		2.1E-04
	5.78	35.07	0.12		7.2E-06
	5.77	35.13	0.12		6.1E-06
	5.8	34.94	0.12		9.4E-06
	5.97	33.95	0.11		4.0E-05
Fluidization**	No Data Points				
	No Data Points				
	No Data Points				
	No Data Points				
	No Data Points				
	Avg. Vol. flow	35.88			
Avg. time	5.67				
		Average Mass Flow	0.12		
	Avg. Vel. (m/s)	0.02		SSD^2	6.89E-05
				kc	2.78
				U_A	1.03E-02
				U_B EES	2.08E-04
				U_C	1.03E-02

EES Calculation for U_B:

Unit Settings: SI K kPa kJ mass deg

Variable±Uncertainty	Partial derivative	% of uncertainty
<u>M = 0.1498±0.0003356 [kg/s]</u>		
T = 4.464±0.01 [s]	$\partial M / \partial T = -0.03356$	100.00 %
Vol = 0.0002027±1.000E-09 [m ³]	$\partial M / \partial Vol = 739.2$	0.00 %

No unit problems were detected.

**Please note that no data points were taken when fluidization occurred.

Opening Area 40%, Large Diameter, and Pressure 1.5 bars:

N: number of data points; DF: number degrees; SSD: Sum of Squared Differences; kc: Coverage Factor

Excel Calculation for U_A and U_C:

	Time (s)	Vol flow (cm ³ /s)	Mass Flow (kg/s)		
pressure	1.5 bar			N	3
				DF	2
	6.21	32.64	0.11		3.0E-06
	6.66	30.43	0.10		3.1E-05
	6.09	33.28	0.11		1.5E-05
Fluidization**	No Data Points				
	No Data Points				
	No Data Points				
	No Data Points				
	No Data Points				
	No Data Points				
	No Data Points				
	No Data Points				
	No Data Points				
	No Data Points				
	Avg. Vol. flow	32.12			
Avg. time	6.32	Average Mass Flow	0.11	SSD^2	2.43E-05
	Avg. Vel. (m/s)	0.02		kc	4.30
				U_A	1.22E-02
				U_B EES	1.68E-04
				U_C	1.22E-02

EES Calculation for U_B:

Unit Settings: SI K kPa kJ mass deg

Variable±Uncertainty	Partial derivative	% of uncertainty
<u>M = 0.1058±0.0001675 [kg/s]</u>		
T = 6.32±0.01 [s]	$\partial M / \partial T = -0.01675$	100.00 %
Vol = 0.0002027±1.000E-09 [m ³]	$\partial M / \partial Vol = 522.2$	0.00 %

No unit problems were detected.

**Please note that no data points were taken when fluidization occurred.

Opening Area 40%, Large Diameter, and Pressure 2 bars:

N: number of data points; DF: number degrees; SSD: Sum of Squared Differences; kc: Coverage Factor

Excel Calculation for U_A and U_C:

	Time (s)	Vol flow (cm ³ /s)	Mass Flow (kg/s)		
pressure	2 bars			N	2
				DF	1
	8.46	23.96	0.08		5.1E-06
	8.97	22.60	0.07		5.1E-06
Fluidization**		No Data Points			
		No Data Points			
		No Data Points			
		No Data Points			
		No Data Points			
		No Data Points			
		No Data Points			
		No Data Points			
		No Data Points			
	Avg. Vol. flow	23.28			
Avg. time	8.72	Average Mass Flow	0.08		
	Avg. Vel. (m/s)	0.01			
				SSD^2	1.01E-05
				kc	12.71
				U_A	2.86E-02
				U_B EES	8.81E-05
				U_C	2.86E-02

EES Calculation for U_B:

Unit Settings: SI K kPa kJ mass deg

Variable±Uncertainty	Partial derivative	% of uncertainty
M = 0.07675±0.00008806 [kg/s]		
T = 8.715±0.01 [s]	$\partial M / \partial T = -0.008806$	100.00 %
Vol = 0.0002027±1.000E-09 [m ³]	$\partial M / \partial Vol = 378.7$	0.00 %

No unit problems were detected.

**Please note that no data points were taken when fluidization occurred.

Opening Area 40%, Small Diameter, and Pressure 0 bars:

N: number of data points; DF: number degrees; SSD: Sum of Squared Differences; kc: Coverage Factor

Excel Calculation for U_A and U_C:

Pressure	Time (s)	Vol flow (cm ³ /s)	Mass Flow (kg/s)		
0 bar				N	10
				DF	9
	3.64	55.68	0.18		2.8E-04
	3.96	51.18	0.17		3.3E-06
	3.69	54.93	0.18		2.0E-04
	3.99	50.80	0.17		2.9E-07
	3.85	52.64	0.17		4.4E-05
	4.08	49.68	0.16		1.0E-05
	4.15	48.84	0.16		3.5E-05
	4.23	47.91	0.16		8.0E-05
	4.17	48.60	0.16		4.5E-05
	4.4	46.06	0.15		2.3E-04
	Avg. Vol. flow	50.63			
Avg. time	4.02	Average Mass Flow	0.17		
	Avg. Vel. (m/s)	0.02		SSD^2	1.03E-04
				kc	2.26
				U_A	7.25E-03
				U_B EES	4.15E-04
				U_C	7.26E-03

EES Calculation for U_B:

Unit Settings: SI K kPa kJ mass deg

Variable±Uncertainty	Partial derivative	% of uncertainty
<u>M = 0.1665±0.0004147 [kg/s]</u>		
T = 4.016±0.01 [s]	$\partial M / \partial T = -0.04147$	100.00 %
Vol = 0.0002027±1.000E-09 [m ³]	$\partial M / \partial Vol = 821.7$	0.00 %

No unit problems were detected.

Opening Area 40%, Small Diameter, and Pressure 0.5 bars:

N: number of data points; DF: number degrees; SSD: Sum of Squared Differences; kc: Coverage Factor

Excel Calculation for U_A and U_C:

Pressure	Time (s)	Vol flow (cm ³ /s)	Mass Flow (kg/s)	
	0.5 bar			N 8
				DF 7
	3.98	50.92	0.17	2.1E-03
	4.98	40.70	0.13	1.4E-04
	5.16	39.28	0.13	5.0E-05
	5.93	34.18	0.11	9.5E-05
	5.48	36.99	0.12	2.3E-07
	5.85	34.65	0.11	6.7E-05
	6.61	30.66	0.10	4.6E-04
	6.83	29.67	0.10	6.1E-04
Fluidization**	No Data Points			
	No Data Points			
	Avg. Vol. flow	37.13		
Avg. time	5.60	Average Mass Flow	0.12	
	Avg. Vel. (m/s)	0.02		
				SSD^2 4.98E-04
				kc 2.36
				U_A 1.87E-02
				U_B EES 2.13E-04
				U_C 1.87E-02

EES Calculation for U_B:

Unit Settings: SI K kPa kJ mass deg

Variable±Uncertainty	Partial derivative	% of uncertainty
M = 0.1194±0.0002131 [kg/s]		
T = 5.603±0.01 [s]	$\partial M / \partial T = -0.02131$	100.00 %
Vol = 0.0002027±1.000E-09 [m ³]	$\partial M / \partial Vol = 589$	0.00 %

No unit problems were detected.

**Please note that no data points were taken when fluidization occurred.

Opening Area 40%, Small Diameter, and Pressure 1 bars:

N: number of data points; DF: number degrees; SSD: Sum of Squared Differences; kc: Coverage Factor

Excel Calculation for U_A and U_C:

Pressure	Time (s)	Vol flow (cm ³ /s)	Mass Flow (kg/s)	
	1 bar			N 7
				DF 6
	12.62	16.06	0.05	1.2E-05
	12.37	16.38	0.05	2.0E-05
	12.35	16.41	0.05	2.1E-05
	12.4	16.35	0.05	1.9E-05
	14.42	14.06	0.05	1.0E-05
	15.33	13.22	0.04	3.6E-05
	15.94	12.72	0.04	5.8E-05
Fluidization**	No Data Points			
	No Data Points			
	Avg. Vol. flow	15.03		
Avg. time	13.63	Average Mass Flow	0.05	
	Avg. Vel. (m/s)	0.01		
				SSD^2 2.92E-05
				kc 2.45
				U _A 5.00E-03
				U _B EES 3.60E-05
				U _C 5.00E-03

EES Calculation for U_B:

Unit Settings: SI K kPa kJ mass deg

Variable±Uncertainty	Partial derivative	% of uncertainty
M = 0.04906±0.00003599 [kg/s]		
T = 13.63±0.01 [s]	$\partial M / \partial T = -0.003599$	100.00 %
Vol = 0.0002027±1.000E-09 [m ³]	$\partial M / \partial Vol = 242.1$	0.00 %

No unit problems were detected.

**Please note that no data points were taken when fluidization occurred.

Opening Area 40%, Small Diameter, and Pressure 1.5 bars:

N: number of data points; DF: number degrees; SSD: Sum of Squared Differences; kc: Coverage Factor

Excel Calculation for U_A and U_C:

Pressure	Time (s)	Vol flow (cm ³ /s)	Mass Flow (kg/s)
	1.5 bar		N 6
			DF 5
	18.41	11.01	0.04 4.8E-07
	18.6	10.90	0.04 1.1E-07
	19.13	10.59	0.03 4.5E-07
	18.74	10.82	0.04 3.2E-09
	18.4	11.02	0.04 5.1E-07
	19.38	10.46	0.03 1.3E-06
Fluidization**	No Data Points		
	No Data Points		
	Avg. Vol. flow	10.80	
Avg. time	18.78	Average Mass Flow	0.04
	Avg. Vel. (m/s)	0.01	
			SSD^2 5.63E-07
			kc 2.57
			U_A 7.88E-04
			U_B EES 1.90E-05
			U_C 7.88E-04

EES Calculation for U_B:

Unit Settings: SI K kPa kJ mass deg

Variable±Uncertainty	Partial derivative	% of uncertainty
M = 0.03562±0.00001897 [kg/s]		
T = 18.78±0.01 [s]	$\partial M / \partial T = -0.001897$	99.99 %
Vol = 0.0002027±1.000E-09 [m ³]	$\partial M / \partial Vol = 175.7$	0.01 %

No unit problems were detected.

**Please note that no data points were taken when fluidization occurred.

Opening Area 40%, Small Diameter, and Pressure 2 bars:

N: number of data points; DF: number degrees; SSD: Sum of Squared Differences; kc: Coverage Factor

Excel Calculation for U_A and U_C:

	Time (s)	Vol flow (cm ³ /s)	Mass Flow (kg/s)
Pressure	2 bars		
			N 3
			DF 2
	20.16	10.05	0.03 1.3E-07
	20.03	10.12	0.03 3.3E-07
	20.98	9.66	0.03 8.8E-07
Fluidization**	No Data Points		
	No Data Points		
	No Data Points		
	No Data Points		
	Avg. Vol. flow	9.94	
Avg. time	20.39	Average Mass Flow	0.03
	Avg. Vel. (m/s)	0.00	

SSD^2	6.69E-07
kc	4.30
U_A	2.03E-03
U_B EES	1.61E-05
U_C	2.03E-03

EES Calculation for U_B:

Unit Settings: SI K kPa kJ mass deg

Variable±Uncertainty	Partial derivative	% of uncertainty
M = 0.0328±0.00001609 [kg/s]		
T = 20.39±0.01 [s]	$\partial M / \partial T = -0.001609$	99.99 %
Vol = 0.0002027±1.000E-09 [m ³]	$\partial M / \partial Vol = 161.8$	0.01 %

No unit problems were detected.

**Please note that no data points were taken when fluidization occurred.

Opening Area 51%, Large Diameter, and Pressure 0 bars:

N: number of data points; DF: number degrees; SSD: Sum of Squared Differences; kc: Coverage Factor

Excel Calculation for U_A and U_C:

pressure	Time (s)	Vol flow (cm ³ /s)	Mass Flow (kg/s)	N	10
	0 bar			DF	9
	2.48	81.73	0.27		1.6E-04
	2.34	86.62	0.29		8.3E-04
	2.75	73.70	0.24		1.9E-04
	2.4	84.45	0.28		4.7E-04
	2.81	72.13	0.24		3.6E-04
	2.56	79.17	0.26		1.7E-05
	3.02	67.11	0.22		1.3E-03
	2.87	70.62	0.23		5.8E-04
	2.73	74.24	0.24		1.5E-04
	2.27	89.29	0.29		1.4E-03
	Avg. Vol. flow	77.91			6.6E-02
Avg. Time	2.62	Average Mass Flow	0.26		
	Avg. Vel. (m/s)	0.04			
				SSD^2	7.95E-03
				kc	2.26
				U_A	6.38E-02
				U_B EES	9.72E-04
				U_C	6.38E-02

EES Calculation for U_B:

Unit Settings: SI K kPa kJ mass deg

Variable±Uncertainty	Partial derivative	% of uncertainty
M = 0.255±0.0009721 [kg/s]		
T = 2.623±0.01 [s]	$\partial M / \partial T = -0.09721$	100.00 %
Vol = 0.0002027±1.000E-09 [m ³]	$\partial M / \partial Vol = 1258$	0.00 %

No unit problems were detected.

Opening Area 51%, Large Diameter, and Pressure 0.5 bars:

N: number of data points; DF: number degrees; SSD: Sum of Squared Differences; kc: Coverage Factor

Excel Calculation for U_A and U_C:

	Time (s)	Vol flow (cm ³ /s)	Mass Flow (kg/s)		
pressure	0.5 bar			N	5
				DF	4
	3.8	53.34	0.18		2.5E-03
	4.84	41.88	0.14		1.5E-04
	6.95	29.16	0.10		8.9E-04
	6.28	32.27	0.11		3.9E-04
	5.88	34.47	0.11		1.5E-04
Fluidization*	No Data Points				
*					
	Avg. Vol. flow	38.22			
Avg. Time	5.55				
		Average Mass Flow	0.13		
	Avg. Vel. (m/s)	0.02			
				SSD^2	1.02E-03
				kc	2.78
					3.96E-02
				U_A	02
				U_B	2.17E-04
				EES	04
					3.96E-02
				U_C	02

EES Calculation for U_B:

Unit Settings: SI K kPa kJ mass deg

Variable±Uncertainty	Partial derivative	% of uncertainty
<u>M = 0.1205±0.0002171 [kg/s]</u>		
T = 5.55±0.01 [s]	$\partial M/\partial T = -0.02171$	100.00 %
Vol = 0.0002027±1.000E-09 [m ³]	$\partial M/\partial \text{Vol} = 594.6$	0.00 %

No unit problems were detected.

**Please note that no data points were taken when fluidization occurred.

Opening Area 51%, Large Diameter, and Pressure 1 bars:

N: number of data points; DF: number degrees; SSD: Sum of Squared Differences; kc: Coverage Factor

Excel Calculation for U_A and U_C:

	Time (s)	Vol flow (cm ³ /s)	Mass Flow (kg/s)		
pressure	1 bar			N	6
				DF	5
	5.15	39.36	0.13		1.7E-03
	6.09	33.28	0.11		4.3E-04
	6.96	29.12	0.10		4.9E-05
	8.67	23.38	0.08		1.4E-04
	10.43	19.43	0.06		6.2E-04
	11.61	17.46	0.06		9.9E-04
Fluidization*	No Data Points				
*	No Data Points				
	No Data Points				
	No Data Points				
	Avg. Vol. flow	27.00			
		Average Mass Flow	0.09		
Avg. Time	8.15				
	Avg. Vel. (m/s)	0.01		SSD^2	7.80E-04
				kc	2.57
				U_A	2.93E-02

U_B	1.01E-
EES	04
	2.93E-
U_C	02

EES Calculation for U_B:

Unit Settings: SI K kPa kJ mass deg

Variable±Uncertainty	Partial derivative	% of uncertainty
M = 0.08205±0.0001007 [kg/s]		
T = 8.152±0.01 [s]	$\partial M / \partial T = -0.01007$	100.00 %
Vol = 0.0002027±1.000E-09 [m ³]	$\partial M / \partial Vol = 404.8$	0.00 %

No unit problems were detected.

**Please note that no data points were taken when fluidization occurred.

Opening Area 51%, Large Diameter, and Pressure 1.5 bars:

N: number of data points; DF: number degrees; SSD: Sum of Squared Differences; kc: Coverage Factor

Excel Calculation for U_A and U_C:

	Time (s)	Vol flow (cm ³ /s)	Mass Flow (kg/s)		
pressure	1.5 bar			N	6
				DF	5
	8.92	22.72	0.07		2.2E-04
	10.43	19.43	0.06		1.6E-05
	11.06	18.33	0.06		1.1E-07
	12.17	16.65	0.05		2.7E-05
	12.51	16.20	0.05		4.5E-05
	12.65	16.02	0.05		5.3E-05
Fluidization*	No Data Points				
*					
	Avg. Vol. flow	18.23			
Avg. Time	11.29				
		Average Mass Flow	0.06	SSD^2	7.21E-05
	Avg. Vel. (m/s)	0.01		kc	2.57
					8.91E-03
				U_A	03
				U_B	5.25E-05
				EES	05
					8.91E-03
				U_C	03

EES Calculation for U_B:

Unit Settings: SI K kPa kJ mass deg

Variable±Uncertainty	Partial derivative	% of uncertainty
<u>M = 0.05924±0.00005247 [kg/s]</u>		
T = 11.29±0.01 [s]	$\partial M/\partial T = -0.005247$	100.00 %
Vol = 0.0002027±1.000E-09 [m ³]	$\partial M/\partial Vol = 292.3$	0.00 %

No unit problems were detected.

**Please note that no data points were taken when fluidization occurred.

Opening Area 51%, Large Diameter, and Pressure 2 bars:

N: number of data points; DF: number degrees; SSD: Sum of Squared Differences; kc: Coverage Factor

Excel Calculation for U_A and U_C:

	Time (s)	Vol flow (cm ³ /s)	Mass Flow (kg/s)		
pressure	2 bars			N	5
				DF	4
	10.16	19.95	0.07		7.6E-05
	10.85	18.68	0.06		2.0E-05
	11.61	17.46	0.06		2.2E-07
	12.98	15.61	0.05		3.1E-05
	13.63	14.87	0.05		6.5E-05
Fluidization*	No Data Points				
*	No Data Points				
	No Data Points				
	No Data Points				
	No Data Points				
	Avg. Vol. flow	17.31			
		Average Mass			
Avg. Time	11.85	Flow	0.06		
	Avg. Vel. (m/s)	0.01			
				SSD^2	4.82E-05
				kc	2.78
				U_A	8.62E-03

U_B	4.77E-
EES	05
	8.62E-
U_C	03

EES Calculation for U_B:

Unit Settings: SI K kPa kJ mass deg

Variable±Uncertainty	Partial derivative	% of uncertainty
<u>M = 0.05646±0.00004766 [kg/s]</u>		
T = 11.85±0.01 [s]	$\partial M / \partial T = -0.004766$	100.00 %
Vol = 0.0002027±1.000E-09 [m ³]	$\partial M / \partial Vol = 278.6$	0.00 %

No unit problems were detected.

**Please note that no data points were taken when fluidization occurred.

Opening Area 51%, Small Diameter, and Pressure 0 bars:

N: number of data points; DF: number degrees; SSD: Sum of Squared Differences; kc: Coverage Factor

Excel Calculation for U_A and U_C:

Pressure	Time (s)	Vol flow (cm ³ /s)	Mass Flow (kg/s)		
0 bar				N	11
				DF	10
	4.59	44.16	0.15		4.6E-04
	5.11	39.66	0.13		4.4E-05
	5.29	38.31	0.13		4.6E-06
	5.4	37.53	0.12		1.8E-07
	5.51	36.78	0.12		8.4E-06
	5.1	39.74	0.13		4.7E-05
	5.43	37.33	0.12		1.2E-06
	5.63	36.00	0.12		3.0E-05
	5.9	34.35	0.11		1.2E-04
	5.86	34.59	0.11		1.0E-04
	5.66	35.81	0.12		3.7E-05
	Avg. Vol. flow	37.66			
Avg. Time	5.41	Average Mass Flow	0.12		
	Avg. Vel. (m/s)	0.02		SSD^2	8.54E-05
				kc	2.23
				U_A	6.21E-03
				U_B EES	2.29E-04
				U_C	6.21E-03

EES Calculation for U_B:

Unit Settings: SI K kPa kJ mass deg

Variable±Uncertainty	Partial derivative	% of uncertainty
M = 0.1237±0.0002288 [kg/s]		
T = 5.407±0.01 [s]	$\partial M / \partial T = -0.02288$	100.00 %
Vol = 0.0002027±1.000E-09 [m ³]	$\partial M / \partial Vol = 610.3$	0.00 %

No unit problems were detected.

Opening Area 51%, Small Diameter, and Pressure 0.5 bars:

N: number of data points; DF: number degrees; SSD: Sum of Squared Differences; kc: Coverage Factor

Excel Calculation for U_A and U_C:

	Time (s)	Vol flow (cm ³ /s)	Mass Flow (kg/s)		
Pressure	0.5 bar			N	7
				DF	6
	7.13	28.43	0.09		3.1E-06
	7.09	28.59	0.09		5.3E-06
	7.03	28.83	0.10		9.6E-06
	6.59	30.76	0.10		8.9E-05
	7.28	27.84	0.09		2.9E-08
	7.39	27.43	0.09		2.4E-06
	8.67	23.38	0.08		2.2E-04
Fluidization*	No Data Points				
*	No Data Points				
	No Data Points				
	Avg. Vol. flow	27.89		SSD^2	5.53E-05
Avg. Time	7.31	Average Mass Flow	0.09	kc	2.45
	Avg. Vel. (m/s)	0.01		U_A	6.88E-03
				U_B	1.25E-04
				EES	6.88E-04
				U_C	6.88E-03

EES Calculation for U_B:

Unit Settings: SI K kPa kJ mass deg

Variable±Uncertainty	Partial derivative	% of uncertainty
M = 0.09148±0.0001251 [kg/s]		
T = 7.311±0.01 [s]	$\partial M / \partial T = -0.01251$	100.00 %
Vol = 0.0002027±1.000E-09 [m ³]	$\partial M / \partial Vol = 451.3$	0.00 %

No unit problems were detected.

****Please note that no data points were taken when fluidization occurred.**

Opening Area 51%, Small Diameter, and Pressure 1 bars:

N: number of data points; DF: number degrees; SSD: Sum of Squared Differences; kc: Coverage Factor

Excel Calculation for U_A and U_C:

Pressure	Time (s)	Vol flow (cm ³ /s)	Mass Flow (kg/s)		
	1 bar			N	5
				DF	4
	8.23	24.63	0.08		4.8E-05
	8.11	24.99	0.08		6.6E-05
	9.08	22.32	0.07		4.5E-07
	10.3	19.68	0.06		8.8E-05
	9.65	21.00	0.07		2.5E-05
Fluidization*	No Data Points				
*	No Data Points				
	No Data Points				
	No Data Points				
	Avg. Vol. flow	22.52			
		Average Mass Flow			
Avg. Time	9.07		0.07	SSD^2	5.71E-05
	Avg. Vel. (m/s)	0.01		kc	2.78
				U_A	9.38E-03
				U_B	8.12E-05
				EES	9.38E-03
				U_C	9.38E-03

EES Calculation for U_B:

Unit Settings: SI K kPa kJ mass deg

Variable±Uncertainty

M = 0.07371±0.00008123 [kg/s]

T = 9.074±0.01 [s]

Vol = 0.0002027±1.000E-09 [m³]

Partial derivative

$\partial M / \partial T = -0.008123$

$\partial M / \partial Vol = 363.7$

% of uncertainty

100.00 %

0.00 %

No unit problems were detected.

****Please note that no data points were taken when fluidization occurred.**

Opening Area 51%, Small Diameter, and Pressure 1.5 bars:

N: number of data points; DF: number degrees; SSD: Sum of Squared Differences; kc: Coverage Factor

Excel Calculation for U_A and U_C:

	Time (s)	Vol flow (cm ³ /s)	Mass Flow (kg/s)		
Pressure	1.5 bar			N	3
				DF	2
	15.83	12.80	0.04		9.4E-09
	15.81	12.82	0.04		2.3E-08
	15.96	12.70	0.04		6.1E-08
Fluidization*	No Data Points				
*	No Data Points				
	No Data Points				
	No Data Points				
	No Data Points				
	Avg. Vol. flow	12.77			
	Avg. Time	15.87	Average Mass Flow	0.04	
	Avg. Vel. (m/s)	0.01			
				SSD^2	4.66E-08
				kc	4.30
				U_A	5.36E-04
				U_B	2.66E-05
				EES	5.37E-05
				U_C	5.37E-04

EES Calculation for U_B:

Unit Settings: SI K kPa kJ mass deg

Variable±Uncertainty	Partial derivative	% of uncertainty
$M = 0.04215 \pm 0.00002657$ [kg/s]		
$T = 15.87 \pm 0.01$ [s]	$\partial M / \partial T = -0.002657$	99.99 %
$Vol = 0.0002027 \pm 1.000E-09$ [m ³]	$\partial M / \partial Vol = 208$	0.01 %

No unit problems were detected.

****Please note that no data points were taken when fluidization occurred.**

Opening Area 51%, Small Diameter, and Pressure 2 bars:

N: number of data points; DF: number degrees; SSD: Sum of Squared Differences; kc: Coverage Factor

Excel Calculation for U_A and U_C:

	Time (s)	Vol flow (cm ³ /s)	Mass Flow (kg/s)		
Pressure	2 bars			N	3
				DF	2
	16.27	12.46	0.04		9.2E-07
	16.78	12.08	0.04		8.5E-08
	16.94	11.96	0.04		4.5E-07
Fluidization*	No Data Points				
*	No Data Points				
	No Data Points				
	No Data Points				
	Avg. Vol. flow	12.17			
Avg. Time	16.66	Average Mass Flow	0.04		
	Avg. Vel. (m/s)	0.01			
				SSD^2	7.24E-07
				kc	4.30
				U_A	2.11E-03
				U_B	2.41E-05
				EES	2.11E-03
				U_C	03

EES Calculation for U_B:

Unit Settings: SI K kPa kJ mass deg

Variable±Uncertainty	Partial derivative	% of uncertainty
<u>M = 0.04014±0.00002409 [kg/s]</u>		
T = 16.66±0.01 [s]	$\partial M / \partial T = -0.002409$	99.99 %
Vol = 0.0002027±1.000E-09 [m ³]	$\partial M / \partial Vol = 198$	0.01 %

No unit problems were detected.

**Please note that no data points were taken when fluidization occurred.

Appendix K: Air Leakage Measurement

This measurement was done using a rotor meter and pressure gauge placed at the inlet of the air flow. Also, all other outlets were sealed except for the particle column, which is where the air will leak through.

$$\dot{m}_{corr} = \dot{m}_{read} \sqrt{\frac{P_{read}}{P_{abs}} \cdot \frac{T_{abs}}{T_{read}}}$$

Table K1: Measured mass flow converted to corrected mass flow.

Pressure (bar) ± 0.05	Measured Mass Flow Rate (slpm) ± 5%	Corrected Mass Flow Rate (slpm) ± 5%
0	0	0
0.5	5.2	3.7
1	6.9	6.9
1.5	9.3	11.4
2	10.7	15.1

Knowing this information, we can calculate the air velocity after it leaves the particulate column since the area of the particulate column is known. This can also help estimate the air velocity near the top of the column, which would help us control the particle carry over in the particle column.

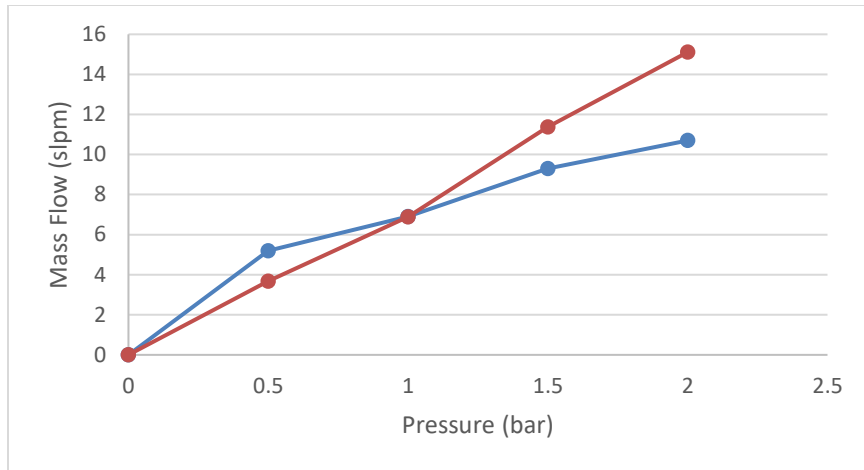


Figure K1: Mass flow compared to pressure. Comparing measured (blue) vs corrected (red) readings.

Appendix L: Entrainment Uncertainty Calculations

Pressure Inlet (PSI)	2		
	Wall	Center	Average SSD
	330	341	335.5 0.0225
	334	342	338 5.5225
	328	344	336 0.1225
	332	341	336.5 0.7225
	334	342	338 5.5225
	329	339	334 2.7225
	325	340	332.5 9.9225
	328	340	334 2.7225
	331	341	336 0.1225
	332	340	336 0.1225
Average Velocity (FPM)	330.3	341	335.65
Average Velocity (m/s)	1.68	1.73	1.71
Mass Entrained (g)			0.00
Time (s)			25.8
Mass Total			4864.4
Mass Flow (kg/s)			0.19
Mass Ratio			0.00%
N	10		
DF	9		
SSD^2			3.05
KC			2.26
U_A (FPM)			1.25
U_A (m/s)			0.006
U_B (FPM) - EES			3
U_B (m/s)			0.015
U_C (m/s)			0.016

Pressure Inlet (PSI)	5			
	Wall	Center	Average	SSD
	440	461	450.5	0.3025
	436	463	449.5	0.2025
	431	458	444.5	29.7025
	433	460	446.5	11.9025
	441	457	449	0.9025
	442	460	451	1.1025
	446	463	454.5	20.7025
	445	462	453.5	12.6025
	436	465	450.5	0.3025
	443	457	450	0.0025
Average Velocity (FPM)	439.3	460.6	449.95	
Average Velocity (m/s)	2.23	2.34	2.29	
Mass Entrained (g)			0.00	
Time (s)			25.0	
Mass Total			4864.4	
Mass Flow (kg/s)			0.19	
Mass Ratio			0.00%	
N	10			
DF	9			
SSD^2				8.63
KC				2.26
U_A (FPM)				2.10
U_A (m/s)				0.012
U_B (FPM) - EES				3
U_B (m/s)				0.015
U_C (m/s)				0.018

Pressure Inlet (PSI)	10		
	Wall	Center	Average SSD
	540	553	546.5 0.36
	539	552	545.5 0.16
	534	555	544.5 1.96
	534	556	545 0.81
	540	555	547.5 2.56
	537	557	547 1.21
	539	555	547 1.21
	536	556	546 0.01
	533	553	543 8.41
	537	557	547 1.21
Average Velocity (FPM)	536.9	554.9	545.9
Average Velocity (m/s)	2.73	2.82	2.77
Mass Entrained (g)			1.38
Time (s)			26.7
Mass Total			4864.4
Mass Flow (kg/s)			0.18
Mass Ratio			0.03%
N	10		
DF	9		
SSD^2			1.98
KC			2.26
U_A (FPM)			1.01
U_A (m/s)			0.005
U_B (FPM) - EES			3
U_B (m/s)			0.015
U_C (m/s)			0.016

Pressure Inlet (PSI)	20			
	Wall	Center	Average	SSD
	869	902	885.5	3.8025
	864	900	882	2.4025
	869	897	883	0.3025
	873	903	888	19.8025
	866	901	883.5	0.0025
	869	898	883.5	0.0025
	873	897	885	2.1025
	870	895	882.5	1.1025
	866	897	881.5	4.2025
	864	898	881	6.5025
Average Velocity (FPM)	868.3	898.8	883.55	
Average Velocity (m/s)	4.41	4.57	4.49	
Mass Entrained (g)			9.76	
Time (s)			24.8	
Mass Total			4864.4	
Mass Flow (kg/s)			0.20	
Mass Ratio			0.20%	
N	10			
DF	9			
SSD^2				4.47
KC				2.26
U_A (FPM)				1.51
U_A (m/s)				0.007
U_B (FPM) - EES				3
U_B (m/s)				0.015
U_C (m/s)				0.017

Pressure Inlet (PSI)	30		
	Wall	Center	Average SSD
	1145	1192	1168.5 1.96
	1150	1190	1170 0.01
	1153	1195	1174 16.81
	1147	1187	1167 8.41
	1153	1188	1170.5 0.36
	1147	1190	1168.5 1.96
	1155	1192	1173.5 12.96
	1147	1190	1168.5 1.96
	1150	1187	1168.5 1.96
	1153	1187	1170 0.01
Average Velocity (FPM)	1150	1189.8	1169.9
Average Velocity (m/s)	5.84	6.04	5.94
Mass Entrained (g)			50.06
Time (s)			25.6
Mass Total			4864.4
Mass Flow (kg/s)			0.19
Mass Ratio			1.03%
N	10		
DF	9		
SSD^2			5.15
KC			2.26
U_A (FPM)			1.62
U_A (m/s)			0.008
U_B (FPM) - EES			3
U_B (m/s)			0.015
U_C (m/s)			0.017

Pressure Inlet (PSI)	40			
	Wall	Center	Average	SSD
	1425	1508	1466.5	4.6225
	1422	1504	1463	1.8225
	1419	1508	1463.5	0.7225
	1425	1504	1464.5	0.0225
	1422	1508	1465	0.4225
	1428	1501	1464.5	0.0225
	1425	1497	1461	11.2225
	1424	1504	1464	0.1225
	1425	1508	1466.5	4.6225
	1426	1504	1465	0.4225
Average Velocity (FPM)	1424.1	1504.6	1464.35	
Average Velocity (m/s)	7.23	7.64	7.44	
Mass Entrained (g)			75.21	
Time (s)			23.4	
Mass Total			4864.4	
Mass Flow (kg/s)			0.21	
Mass Ratio			1.55%	
N	10			
DF	9			
SSD^2				2.67
KC				2.26
U_A (FPM)				1.17
U_A (m/s)				0.006
U_B (FPM) - EES				3
U_B (m/s)				0.015
U_C (m/s)				0.016

Pressure Inlet (PSI)	50			
	Wall	Center	Average	SSD
	1568	1765	1666.5	5.5225
	1565	1761	1663	34.2225
	1572	1769	1670.5	2.7225
	1578	1773	1675.5	44.2225
	1565	1769	1667	3.4225
	1567	1773	1670	1.3225
	1573	1761	1667	3.4225
	1572	1765	1668.5	0.1225
	1578	1769	1673.5	21.6225
	1569	1765	1667	3.4225
Average Velocity (FPM)	1570.7	1767	1668.85	
Average Velocity (m/s)	7.98	8.98	8.48	
Mass Entrained (g)			105.16	
Time (s)			25.4	
Mass Total			4864.4	
Mass Flow (kg/s)			0.19	
Mass Ratio			2.16%	
N	10			
DF	9			
SSD^2				13.33
KC				2.26
U_A (FPM)				2.61
U_A (m/s)				0.013
U_B (FPM) - EES				3
U_B (m/s)				0.015
U_C (m/s)				0.020

Appendix M: Uncertainty Analysis for Particle Size Measurements

Below are the data table for the particle size measurements measured in mm on the microscopic ruler. This was done on 30 particles in the sample and then divided into 100 micrometer segments. Furthermore, the figures below show pictures of the sample under the microscope for each run.

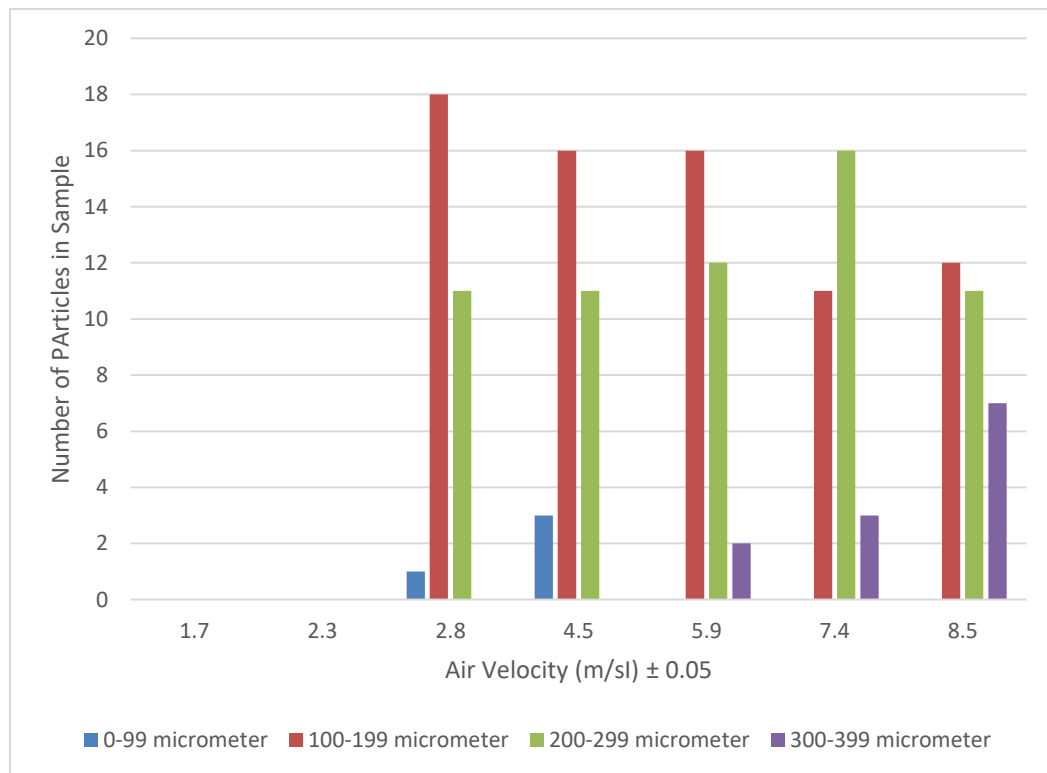


Figure M1: Summary of results for the sizes of the particle entrained.

Table M1: Uncertainty analysis for particle size measurements at an air velocity of 2.8 m/s.

Particle	2.8 m/s	SSD^2
1	0.22	2.18E-03
2	0.23	3.21E-03
3	0.18	4.44E-05
4	0.08	8.71E-03
5	0.11	4.01E-03
6	0.15	5.44E-04
7	0.17	1.11E-05
8	0.16	1.78E-04
9	0.12	2.84E-03
10	0.2	7.11E-04
11	0.19	2.78E-04
12	0.21	1.34E-03
13	0.2	7.11E-04
14	0.16	1.78E-04
15	0.23	3.21E-03
16	0.19	2.78E-04
17	0.22	2.18E-03
18	0.12	2.84E-03
19	0.21	1.34E-03
20	0.22	2.18E-03
21	0.2	7.11E-04
22	0.19	2.78E-04
23	0.21	1.34E-03
24	0.14	1.11E-03
25	0.12	2.84E-03
26	0.17	1.11E-05
27	0.16	1.78E-04
28	0.15	5.44E-04
29	0.13	1.88E-03
30	0.16	1.78E-04
Average size (mm)	0.17	
	SSD^2	4.61E-02
	N	30
	DF	29
	Kc	2.05
	U_A	0.08
	U_B	0.05
	U_C	0.09

Table M2: Uncertainty analysis for particle size measurements at an air velocity of 4.5 m/s.

Particle	4.5 m/s	SSD^2
1	0.19	1.60E-04
2	0.12	3.29E-03
3	0.15	7.47E-04
4	0.14	1.39E-03
5	0.23	2.77E-03
6	0.21	1.07E-03
7	0.22	1.82E-03
8	0.17	5.38E-05
9	0.11	4.53E-03
10	0.13	2.24E-03
11	0.2	5.14E-04
12	0.08	9.47E-03
13	0.09	7.63E-03
14	0.18	7.11E-06
15	0.26	6.83E-03
16	0.26	6.83E-03
17	0.25	5.28E-03
18	0.23	2.77E-03
19	0.21	1.07E-03
20	0.17	5.38E-05
21	0.22	1.82E-03
22	0.2	5.14E-04
23	0.18	7.11E-06
24	0.07	1.15E-02
25	0.2	5.14E-04
26	0.22	1.82E-03
27	0.16	3.00E-04
28	0.15	7.47E-04
29	0.19	1.60E-04
30	0.13	2.24E-03
Average size (mm)	0.18	
	SSD^2	7.82E-02
	N	30
	DF	29
	Kc	2.05
	U_A	0.10
	U_B	0.05
	U_C	0.12

Table M3: Uncertainty analysis for particle size measurements at an air velocity of 5.9 m/s.

Particle	5.9 m/s	SSD^2
1	0.32	1.61E-02
2	0.15	1.85E-03
3	0.16	1.09E-03
4	0.14	2.81E-03
5	0.19	9.00E-06
6	0.3	1.14E-02
7	0.21	2.89E-04
8	0.17	5.29E-04
9	0.18	1.69E-04
10	0.12	5.33E-03
11	0.22	7.29E-04
12	0.19	9.00E-06
13	0.26	4.49E-03
14	0.24	2.21E-03
15	0.13	3.97E-03
16	0.19	9.00E-06
17	0.22	7.29E-04
18	0.12	5.33E-03
19	0.21	2.89E-04
20	0.22	7.29E-04
21	0.2	4.90E-05
22	0.21	2.89E-04
23	0.19	9.00E-06
24	0.23	1.37E-03
25	0.16	1.09E-03
26	0.21	2.89E-04
27	0.22	7.29E-04
28	0.17	5.29E-04
29	0.11	5.33E-03
30	0.14	2.81E-03
Average size (mm)	0.19	
	SSD^2	7.06E-02
	N	30
	DF	29
	Kc	2.05
	U_A	0.10
	U_B	0.05
	U_C	0.11

Table M4: Uncertainty analysis for particle size measurements at an air velocity of 7.4 m/s.

Particle	7.4 m/s	SSD^2
1	0.12	8.16E-03
2	0.17	1.63E-03
3	0.27	3.56E-03
4	0.23	3.87E-04
5	0.29	6.35E-03
6	0.18	9.20E-04
7	0.3	8.04E-03
8	0.26	2.47E-03
9	0.16	2.53E-03
10	0.21	1.11E-07
11	0.14	4.95E-03
12	0.2	1.07E-04
13	0.21	1.11E-07
14	0.28	4.85E-03
15	0.32	1.20E-02
16	0.23	3.87E-04
17	0.18	9.20E-04
18	0.25	1.57E-03
19	0.26	2.47E-03
20	0.22	9.34E-05
21	0.21	1.11E-07
22	0.2	1.07E-04
23	0.22	9.34E-05
24	0.31	9.93E-03
25	0.13	6.45E-03
26	0.15	3.64E-03
27	0.16	2.53E-03
28	0.14	4.95E-03
29	0.12	1.01E-02
30	0.2	1.07E-04
Average size (mm)	0.21	
	SSD^2	9.93E-02
	N	30
	DF	29
	Kc	2.05
	U_A	0.12
	U_B	0.05
	U_C	0.13

Table M5: Uncertainty analysis for particle size measurements at an air velocity of 8.5 m/s.

Particle	8.5 m/s	SSD^2
1	0.14	7.11E-03
2	0.15	5.53E-03
3	0.17	2.95E-03
4	0.16	4.14E-03
5	0.13	8.90E-03
6	0.27	2.09E-03
7	0.33	1.12E-02
8	0.31	7.34E-03
9	0.22	1.88E-05
10	0.32	9.15E-03
11	0.25	6.59E-04
12	0.23	3.21E-05
13	0.2	5.92E-04
14	0.19	1.18E-03
15	0.28	3.10E-03
16	0.24	2.45E-04
17	0.14	7.11E-03
18	0.18	1.97E-03
19	0.15	5.53E-03
20	0.34	1.34E-02
21	0.25	6.59E-04
22	0.14	7.11E-03
23	0.3	5.73E-03
24	0.32	9.15E-03
25	0.2	5.92E-04
26	0.25	6.59E-04
27	0.31	7.34E-03
28	0.17	2.95E-03
29	0.2	5.92E-04
30	0.19	1.18E-03
Average size (mm)	0.22	
	SSD^2	1.28E-01
	N	30
	DF	29
	Kc	2.05
	U_A	0.13
	U_B	0.05
	U_C	0.14

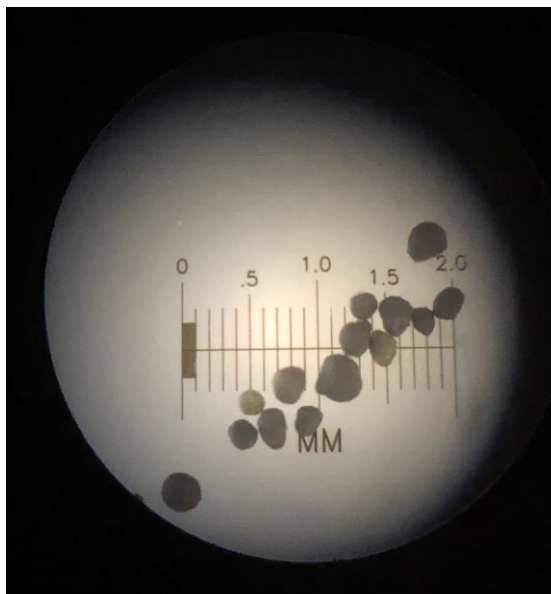


Figure M2: 10 PSI microscopic image of the particles.

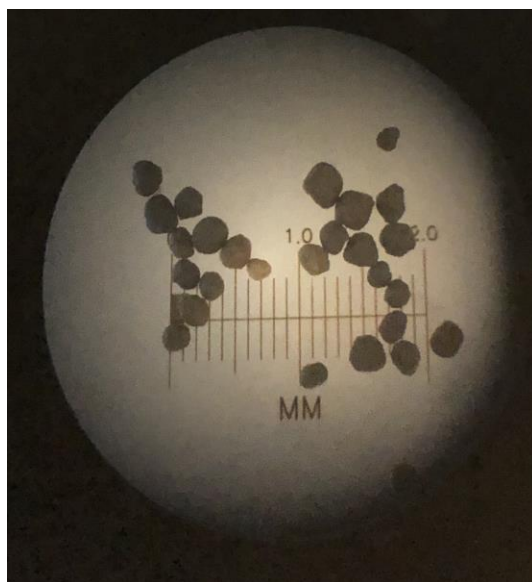


Figure M3: 20 PSI microscopic image of the particles.

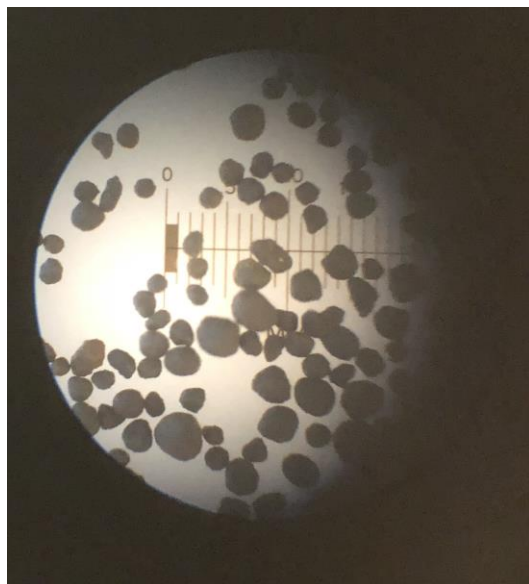


Figure M4: 30 PSI microscopic image of the particles.

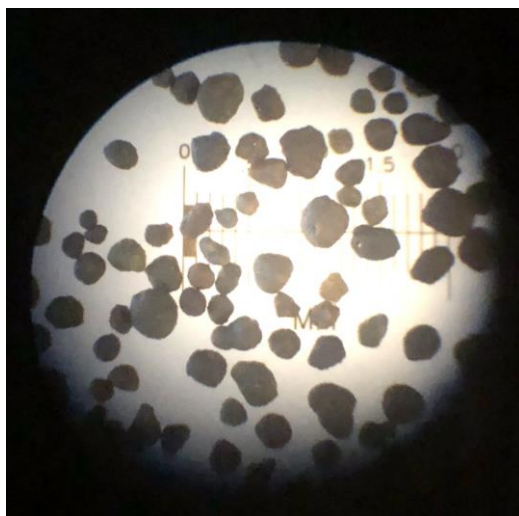


Figure M5: 40 PSI microscopic image of the particles.

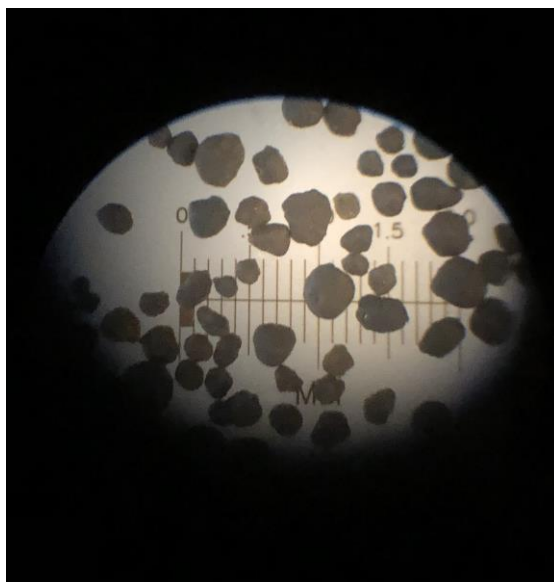


Figure M6: 50 PSI microscopic image of the particles.